UNIVERSITY OF CALIFORNIA, SAN DIEGO

On Anomalous Plasma Transport in The Edge of Magnetic Confinement Devices

A dissertation submitted in partial satisfaction of the

requirements for the degree

Doctor of Philosophy

in

Engineering Sciences (Engineering Physics)

by

Justin Ray Angus

Committee in charge:

Professor Sergei I. Krasheninnikov, Chair
Professor Gaurav Arya
Professor Farhat Beg
Professor Asoka Mendis
Professor Daniel Tartakovsky

2012

The dissertation of Justin Ray Angus is approved, and it is acceptable in quality and form for publication on microfilm and electronically:

_____

_____

_____

_____

_____

Chair

University of California, San Diego

2012

DEDICATION

To the polar bears.

EPIGRAPH

"... The function of man is to live, not to exist.
I shall not waste my days trying to prolong them.
I shall use my time."
—Jack London

TABLE OF CONTENTS

LIST OF FIGURES

ACKNOWLEDGEMENTS

I would like to thank Sergei Krasheninnikov, Maxim Umansky, Tom Rognlien, Ron Cohen, Mikhail Dorf, and Milo Dorr for their collaborations and academic guidance. I would also like to extend my special thanks to Olivia Bui for her endless effort to support me during my graduate studies.

Chapter 2, in full, is a reprint of the material as it appears in *Effects of parallel electron dynamics on plasma blob transport* in Physics of Plasmas 19, 082312 by J. Angus, M. Umansky, and S. Krasheninnikov, 2012. The dissertation author was the primary investigator and author of this paper.

Chapter 3, in full, is a reprint of the material as it appears in *Drift wave dispersion relation for arbitrarily collisional plasmas* in Physics of Plasmas 19, 052504 by J. Angus and S. Krasheninnikov, 2012. The dissertation author was the primary investigator and author of this paper.

VITA

2007	B.S. in Mathematics Marshall University, Huntington, WV
2007	B.S. in Physics Marshall University, Huntington, WV
2007-2010	Powell Fellow University of California, San Diego, La Jolla, CA
2008	Summer Internship Far-Tech, San Diego, CA
2008	Teaching Assistant CENG101A: Introductory Fluid Mechanics Department of Mechanical and Aerospace Engineering University of California, San Diego, La Jolla, CA
2009-2012	Graduate Research Assistant Sergei Krasheninnikov's group Department of Mechanical and Aerospace Engineering University of California, San Diego, La Jolla, CA
2009	M.S. in Engineering Physics University of California, San Diego, La Jolla, CA
2009	Teaching Assistant MAE118a: Engineering and The Environment Department of Mechanical and Aerospace Engineering University of California, San Diego, La Jolla, CA
2010	Teaching Assistant MAE118c: Nuclear Engineering Department of Mechanical and Aerospace Engineering University of California, San Diego, La Jolla, CA
2012	Ph.D. in Engineering Physics University of California, San Diego, La Jolla, CA

PUBLICATIONS

Energy gain of free electron in pulsed electromagnetic plane wave with constant external magnetic fields, J. Angus and S. Krasheninnikov, Phys. of Plasmas 16, 113103 (2009).
http://dx.doi.org/10.1063/1.3259968

Kinetic theory of electromagnetic plane wave obliquely incident on bounded plasma slab, J. Angus, S. Krasheninnikov, and A. Smolyakov, Phys. of Plasmas 17, 102115 (2010).
http://dx.doi.org/10.1063/1.3499664

Drift wave dispersion relation for arbitrarily collisional plasmas, J. Angus, S. Krasheninnikov, Phys. of Plasmas 19, 052504 (2012).
http://dx.doi.org/10.1063/1.4714614

Effect of Drift Waves on Blob Dynamics, J. Angus M. Umansky, and S. Krasheninnikov, Physical Review Letters 108, 215002 (2012).
http://link.aps.org/doi/10.1103/PhysRevLett.108.215002

3D Blob Modelling with BOUT++, J. Angus, M. Umansky, and S. Krasheninnikov, Contrib. Plasma Phys., 52: 348-352. (2012).
doi: 10.1002/ctpp.201210015

Progress with the cogent edge kinetic code: Collision operator options, M. Dorf, R. Cohen, J. Compton, M. Door, T. Rognlien, J. Angus, S. Krasheninnikov, P. Colella, D. Martin, P. McCorquodale, Contrib. Plasma Phys., 52: 518-522. (2012).
doi: 10.1002/ctpp.201210042

Effects of parallel electron dynamics on plasma blob transport, J. Angus, M. Umansky, S. Krasheninnikov, Phys. of Plasmas 19, 082312 (2012).
http://dx.doi.org/10.1063/1.4747619

Review and limitations of 3D plasma blob modeling with reduced collisional fluid equations, J. Angus, M. Umansky, S. Krasheninnikov, Submitted to Journal of Nuclear Materials, May 2012.

ABSTRACT OF THE DISSERTATION

On Anomalous Plasma Transport in The Edge of Magnetic Confinement Devices

by

Justin Ray Angus

Doctor of Philosophy in Engineering Sciences (Engineering Physics)

University of California, San Diego, 2012

Professor Sergei I. Krasheninnikov, Chair

Magnetic confinement devices use strong magnetic fields to confine fusion grade plasmas for the purpose of producing fusion energy. Fully understanding plasma transport in these devices is crucial for the realization of a fusion reactor. The plasma transport is governed mostly by anomalous (turbulent) processes. Furthermore, the edge region is characterized by strong gradients in plasma profiles leading to coherent convecting structures known as plasma blobs that can dominant the far edge transport. This Thesis work is concerned with a characterization of plasma blob dynamics through a combination of theoretical investigations and 3D simulations of the collisional Braginskii equations using the code BOUT++. Another topic of this Thesis is the modeling of mean profile evolution due to fluctuating anomalous transport. The model is a formulated as a kinetic extension of fluid models and is implemented into the 2D2V gyrokinetic code COGENT.

Chapter 1

Introduction

The central focus of this Thesis concerns plasma transport in the edge region of magnetic confinement devices. Magnetic confinement devices are designed to study confinement of fusion grade plasmas using strong magnetic fields. Before discussing the specific topics of this Thesis, it is worth while to first answer some basic questions such as, what is fusion energy, how do magnetic confinement devices work, and why is plasma transport in the edge region of these devices important to study?

1.1 Background

The hydrogen isotopes deuterium (H^2) and tritium (H^3) will fuse together to form an alpha particle (He^4) with 3.5MeV of kinetic energy and a neutron with 14.1MeV of kinetic energy when they are brought close enough together that the attractive strong nuclear force overcomes the repulsive electrostatic force. Obtaining energy from fusion is an attractive alternative to current forms of energy production for electrical power plants such as nuclear fission and the burning of carbon based fossil fuels like gas and coal. Fossil fuels have relatively low energy densities ($25-50$MJ/kg) and emit harmful amounts of bi-products into the atmosphere. Nuclear fission has an extremely high energy density ($\sim 8.0\times 10^7$MJ/kg)

and produces no air pollutants, but can be dangerously unstable, since fission is a chain reaction, and produces radioactive waste with half-lifes on the order of thousands of years [1]. Fusion energy, on the other hand, has a higher energy density than both carbon and fission ($\sim 3.3 \times 10^8$MJ/kg), poses no risk of unstable meltdown, and produces no carbon emissions. Nuclear waste created by the high energy neutrons may still be an issue, but it is believed that this can be minimized by controlling what materials are exposed to the high energy neutron flux.

There are two basic requirements that need to be satisfied in order for fusion energy to be a viable energy source. First, the DT fuel needs to be heated to temperatures on the order of 10keV for enough fusion reactions to take place. This is equivalent to about 100 million degrees Celsius and any substance at this temperature will inevitably be in a plasma state. A plasma is an ionized state of a gas that occurs when the thermal energy is large enough to prevent the negatively charged electrons from recombining with the positively charged ions. The second requirement is that ignition of fuel takes place, which means that the plasma energy is confined long enough that the fusion power produced is sufficient to maintain the fuel at fusion conditions with minimal or no external heating sources.

The energy confinement requirement needed to reach ignition precludes confinement with material vessels alone since any contact with material surfaces would quickly cool off the very thin plasma. One approach to confine fusion grade plasmas is to leverage the fact that a plasma consist of independently charged particles, which have a difficult time crossing magnetic fields, and confine the plasma using strong magnetic fields. This is known as magnetic confinement. One of the most promising magnetic confinement devices for a fusion reactor are toroidally shaped devices known as tokamaks [2]. The toroidal shape is used to obtain full 3D confinement since charged particles are free to move along magnetic field lines. A basic example of a tokamak is shown in Fig. 1.1. The toroidal magnetic fields are produced by currents flowing through coils wrapped poloidally around the exterior of the device. A smaller poloidal field that leads to a helical shape of the magnetic field lines, which is mostly induced by the plasma current flowing in the toroidal

direction, is also required for equilibrium where the magnetic pressure balances the thermal pressure of the plasma.

The interior of magnetic confinement devices can be separated into two main regions - the core, which is characterized by closed magnetic field lines, and the edge, also known as the scrape-off layer (SOL), where the field lines end on material surfaces. The edge region forms the boundary between the hot core and the material surfaces of the device. The core plasma performance is limited by cross field plasma transport from the core to the edge that is limited by how well the edge plasma transport can be controlled and the tolerable concentrations of particle and heat fluxes on the material surfaces. The particle and heat fluxes on material surfaces must be held to a tolerable limit not only to limit unwanted wall materials entering the core of the plasma (pollution) and radiating away the energy, but also to maintain the integrity of the device and to limit retention of radioactive hydrogen isotopes in the wall of the vessel [3].

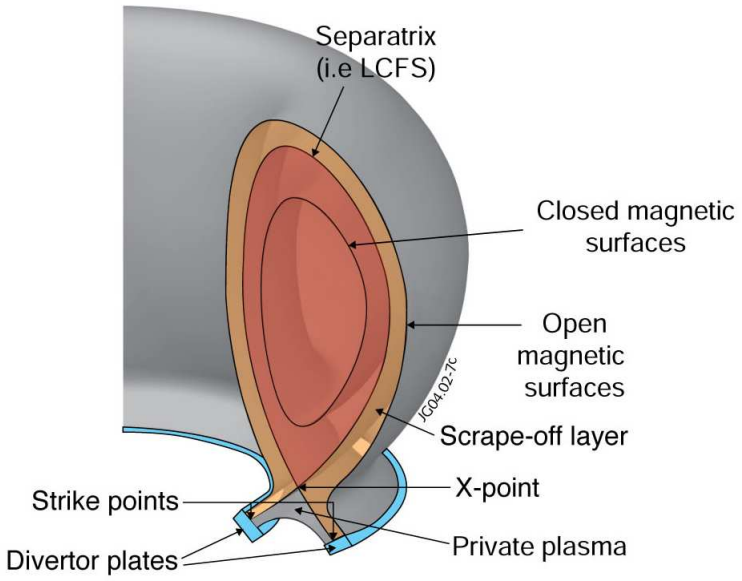

Figure 1.1: Example diagram of tokamak.

The ideal cross field plasma transport mechanisms in a tokamak is collisional diffusion. Collisional transport in a torus is known as neoclassical transport and is an extension of collisional transport in a magnetized cylinder that accounts for

the toroidal geometry effects on the particle orbits [4]. The tokamak edge region is designed so that plasma entering the edge region from the core will flow along the field lines to divertor or limiter regions where the plasma can be recycled and the particle and heat loads can be tolerated. However, cross field plasma transport is found to be dominated by turbulent (anomalous) processes and the radial fluxes are much larger than that predicted by neoclassical theories [5]. Furthermore, since the core-edge boundary is the transition region between the hot core and the cooler SOL, the transport in this region is further complicated due to strong gradients in plasma profiles that lead to strong bursty-like convective transport. This latter process leads to concentrated plasma fluxes reaching the tokamak walls on time scales short compared to that for the plasma to flow to the divertor regions. A lack of predictive capabilities for the edge plasma transport that stems from a lack of understanding is one of the main limiting factors in achieving thermonuclear fusion in magnetic confinement devices.

1.2 Dissertation Outline

A detailed description of anomalous cross-field transport in the edge of magnetic confinement devices is one of the most challenging issues in magnetic confinement physics [5–10]. In general, the turbulent fluctuations are electromagnetic in nature, but, at least in low $\beta \equiv 8\pi nT/B^2$ systems, the turbulence is largely electrostatic [2,6,11]. The enhanced cross field plasma flux is a result of the $\mathrm{E} \times \mathrm{B}$ drift associated with the electrostatic fluctuations. The main goal of tokamak transport studies is to understand the physics of the transport well enough that the radial particle and heat fluxes can be determined. However, due to the complex nature of anomalous edge transport, this is not so easily accomplished. One of the complicating features of edge turbulence is the broad range of observed density fluctuations ranging from $\sim 5\%$ of the background density near the last closed flux surface to $\gtrsim 100\%$ in the far SOL [10].

The relatively large amplitude density perturbations in the edge region are

associated with coherent field-aligned structures known as plasma blobs. These blobs are strongly convective and contribute about 50% of the total cross field plasma transport near the last closed flux surface [12]. Furthermore, at least in low-confinement discharged (L-mode), these blobs are consider to dominate the transport in the far SOL [13]. Plasma blobs are formed as a result of turbulent processes in the core-edge boundary and bring dense clumps of plasma across the SOL to the material walls on time scales short compared to the parallel loss time. The creation and propagation of a blob in the SOL during an experiment on the NSTX tokamak is shown in Fig. 1.2 [14]. Although plasma blobs are formed as a result of the plasma turbulence in the core-edge boundary, the evolution of plasma blobs propagating through the less dense far SOL can be treated as individual entities and studied separately from the fine scale plasma turbulence.

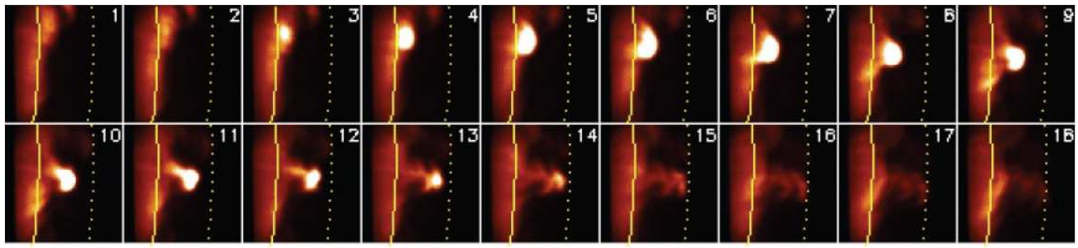

Figure 1.2: Creation and propagation of plasma blob in SOL of NSTX tokmamak [14]. Images are produced using GPI diagnostics. The toroidal direction is into the page, the solid line represents the last closed flux surface, and the dashed line represents the limiter shadow region. This blob has an approximate radius of $\sim$ 2cm and avection velocity of $\sim$ 1km/s.

In situations where the amplitude of the turbulent fluctuations are small compared to the background parameters, the mean profiles drive the turbulent fluctuations, which in turn alter the mean profiles and self-consistent modeling is of course required for precise transport studies [15, 16]. However, since the time and spatial scales of the turbulent fluctuations are much smaller than the mean parameter transport scales, the mean profile evolution due to anomalous processes are typically studied separately from the generation and details of plasma turbulence. This is done by using models to represent the effects of turbulent transport on the mean profiles.

The work presented in this Thesis focuses on a characterization of the evolution of plasma blobs and the modeling of mean profile evolution due to anomalous transport. It should be mentioned that, although the discussion above was mainly tokamak oriented, plasma turbulence in toroidal devices shares many similarities with turbulence in linear and helical devices. Thus, the results of this Thesis work are not limited to tokamaks alone, but can be applicable to magnetic confinement devices in general. An overview of each chapter in this Thesis is outlined below. A lot of the work presented in this Thesis is related to the flute mode instability and or drift waves. Both of these modes are common linear modes in magnetized plasmas. A brief review of the basic physics of both is given in Appendix A.

1.2.1 Ch. 2: Effects of Parallel Electron Dynamics on Plasma Blobs

Almost all work to date on plasma blobs have ignored effects of the parallel variation of parameters along the field line on the 2D cross field dynamics by invoking different closure schemes to represent the parallel physics. However, it has recently been suggested that 3D dynamics may indeed be important to better understand what is seen in experiments [17]. The 3D effects on sheath connected plasma blobs that result from parallel electron dynamics are examined in this Chapter by allowing for the variation of blob density and potential along the magnetic field line and using collisional Ohm's law to model the parallel current density. The parallel current density from linear sheath theory, typically used in the 2D model, is implemented as parallel boundary conditions. This model includes electrostatic 3D effects, such as resistive drift waves and blob spinning, while retaining all of the fundamental 2D physics of sheath connected plasma blobs.

1.2.2 Ch. 3: Drift Wave Dispersion Relation for Arbitrarily Collisional Plasma

One of the main results of Ch. 2 is that the collisionally resistive drift wave instability can dissipate plasma blobs. However, the dominant unstable modes that affect plasma blobs are found to exist in parameter regimes that only marginally satisfy several of the assumptions considered for the validity of the reduced collisional fluid equations used in the study. Namely, the neglect of parallel electron heat flow and finite electron mean free path. How the mode structure and growth rate of the drift wave instability would be altered due to these effects is addressed in this Chapter by generalizing the standard local linear analysis of drift waves in a plasma slab to be valid for arbitrarily collisional electrons. The role of finite ion temperature on the dominant unstable modes is also addressed.

1.2.3 Ch. 4: Model Drag-Diffusion Collision Operator for Kinetic Codes

Numerical simulation of velocity space collisions in a plasma poses many challenging tasks. In some situations, the detailed relaxation of a species to thermodynamic equilibrium is not important and more computationally efficient "model" operator can be used in kinetic codes. These "model" operators may not be obtainable from any limiting situation of the full nonlinear Fokker-Planck collision operator in a plasma, but still relax the distribution function to thermodynamic equilibrium while satisfying the appropriate conservation properties. One such model is the Fokker-Planck collision operator for Brownian motion. It is demonstrated in this Chapter how this operator can be used as a model for like-like particle collisions in a plasma. The structure of this operator is particularly appealing for kinetic codes because the conservation of density, momentum, and energy can be obtained exactly numerically with little computational effort.

1.2.4 Ch. 5: Anomalous Transport Model for Kinetic Simulations

The time scale of turbulent fluctuations is much smaller than that of the mean profile evolution and transport in the edge of magnetic confinement devices. It is therefore much more numerically efficient for transport studies to introduce models that represent the effects of turbulent fluctuations on the mean profiles rather than fully resolving the turbulent time scale. Such models are frequently used in fluid transport codes, but increasing need for a kinetic description of the edge region requires a kinetic extension of these fluid models to kinetic codes. One such model for gyrokinetic studies is proposed in this Chapter. The model has been implemented into the gyrokinetic code COGENT and several verification tests are performed.

Chapter 2

Effects of Parallel Electron Dynamics on Plasma Blobs

Plasma blobs are regularly seen in the edge region of magnetic confinement devices and are typically characterized as filamentary like structures along the magnetic field line with an isolated density bump in the drift plane. They are strongly convective structures that form as a result of turbulent processes and can often dominate the transport in the far scrape-off layer of magnetic confinement devices. Plasma blobs are of large interest to the plasma physics community because of their role in edge transport, plasma exhaust, and plasma-wall interactions for magnetically confined fusion devices known as tokamaks. There have been numerous studies done on plasma blobs in recent years [12, 13, 17–29]. A thorough review of the current theoretical and experimental understanding of plasma blobs can be found in the recent review paper by D'Ippolito *et al.* [17].

The basic physics of blobs, shown in Fig. 2.1, is that charge polarizing forces combined with a vertical density gradient gives rise to an electric field that produces an E×B drift and drives the blob radially outward. The dynamics of the blob evolution is then determined by the dominant form of charge mitigation, which can be through either perpendicular or parallel dynamics. Almost all work to date has only considered the 2D dynamics of blobs by invoking different closure

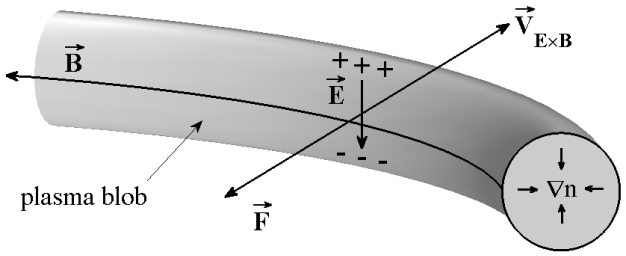

Figure 2.1: Basic physics of plasma blobs driven by charge polarizing forces. Reprinted with permission from J. Angus, M. Umansky, and S. Krasheninnikov, Phys. Rev. Lett. 108, 215002 (2012). Copyright 2012, American Physical Society.

schemes to model the parallel dynamics. The most basic model for the parallel dynamics is to assume that the blob is connected to material surfaces at each end of the magnetic flux tubes so that the potential is limited by the current flowing into the sheaths at the parallel boundaries (see Fig. 2.2). Examples of other closure schemes sometimes considered are the enhanced cross-field polarization current that takes place near magnetic X-points in diverted tokamaks and the outgoing propagation of Alfven waves in finite beta plasma where magnetic field line bending can be important. A detailed discussion of all the different 2D closure schemes that have been considered for the parallel dynamics can be found in [25].

The various closure schemes discussed above for the parallel dynamics has proven useful for basic analytical estimates of blob properties to be compared with experimental results. However, there is still quite a bit of discrepancy and "scatter" found when comparing experimental results with 2D models [17]. It is plausible that one of the culprits for the disparity between experiment and theory could be 3D effects that result from the variation of parameters along the magnetic field line. In this Chapter, the 3D effects on blob dynamics due to parallel electron dynamics are examined in the electrostatic limit by allowing for the variation of potential and density along the field line and using collisional Ohm's law to model the parallel current density. The conventional closure scheme for the parallel dynamics in the 2D sheath connected model is implemented through the parallel boundary conditions in the 3D model.

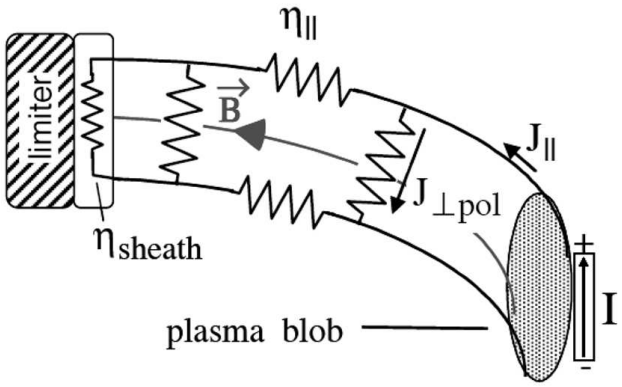

Figure 2.2: Circuit diagram of current path in basic sheath connected plasma blobs. Reprinted with permission from S. I. Krasheninnikov, D. A. D'Ippolito, and J. R. Myra, J. Plasma Phys. 74. 679 (2008). Copyright 2008, Cambridge University Press.

The most fundamental new physical phenomenon that enters into the standard blob model as a result of the parallel electron dynamics is the linear resistive drift wave instability. The effects of resistive drift waves on blob dynamics has recently been discussed by the authors in [30]. It is demonstrated in [30] that the blob's density gradient is depleted during the nonlinear stage of this instability resulting in a much more diffuse blob. Since the blob's density gradient is responsible for the charge polarization that drives the blob radially outward, the diffuse blob has little (if any) radial motion. The relative importance of drift waves on blob dynamics is estimated in [30] by comparing the maximum growth rate from a local linear analysis of the governing equations with the radial convection rate from 2D theory. This expression (Eq. 6 in [30]) suggests that smaller blobs and blobs in systems with a smaller effective gravity force will be more susceptible to the drift wave instability. These results are supported [30] by a direct comparison of 2D and 3D seeded blob simulations.

Another consequence of the parallel electron dynamics is the mitigation of polarized charge via blob spinning that results from a Boltzmann-like potential that arises when a blob has some varying profile along the magnetic field line. The spinning results from the poloidal E×B drift resulting from the dependence of the Boltzmann potential on the radially varying blob density profile in the drift

plane. (here, "poloidal" and "radial" are considered to be with respect to polar coordinates centered on the blob with axial direction along B.) This situation is similar to the blob spinning that results from a sheath connected blob with some radially varying temperature profile [21]. It was demonstrated in [21] how spinning can increase the blob's coherency, reduce the radial cross field convection, induce a poloidal component of convection, and stabilize the flute mode instability. (here, "poloidal and "radial" refer to the effective poloidal and radial coordinates in the edge region of the magnetic confinement device.)

The variation of plasma density along the magnetic field line also leads to parallel ion dynamics in the form of sound waves and density transport along the field line. However, the parallel density profiles analyzed in this paper are considered to be modest enough that the resulting parallel ion dynamics occurs on time scales long compared to the 2D and parallel electron dynamics. For these reasons, the parallel ion dynamics are ignored in this work and only parallel electron dynamics are considered in detail.

The remainder of this paper is outlined as follows: The 3D governing equations are presented in the next section of this paper and it is demonstrated how the 3D model reduces to the 2D model in the appropriate limits. The discussion of the governing equations is followed by a review of the basic 2D sheath limited blob model with which I wish to compare the results from the 3D model with. The examination of 3D effects begins by reviewing the work on the effect of drift waves on blob dynamics given in [30] with a more detailed comparison of the modes seen in the simulations with those predicted by the simplified local linear analysis. The 3D analysis is concluded by demonstrating how blob spinning that results from a parallel density profile can affect the blob evolution. The deviation of blob dynamics from 2D theory due to drift waves and Boltzmann spinning is demonstrated by a direct comparison of 2D and 3D seeded blob simulations of the governing equations using the code BOUT++ [31]. A summary of the results along with a discussion of the limitations of the model and an outlook towards future studies is given in the conclusion of this chapter.

2.1 Governing Equations

The basic equations governing the dynamics of plasma blobs are obtained from the conservation of charge and density in a quasi-neutral plasma.

$$\nabla \cdot \left(J_{\parallel} \hat{\mathbf{b}} + \mathbf{J}_{\perp} \right) = 0, \tag{2.1}$$

$$\frac{\partial n}{\partial t} + \nabla \cdot (n \mathbf{V}) = 0, \tag{2.2}$$

where $J_{\parallel}$ and $\mathbf{J}_{\perp}$ are respectively the current density along and transverse to the magnetic field $\mathbf{B} = B\hat{\mathbf{b}}$, n is the plasma density, and $\mathbf{V} = \mathbf{V}_{\perp} + V_{\parallel}\hat{\mathbf{b}}$ can be either the electron or the ion mean velocity since quasi-neutrality is assumed. The plasma is assumed to be highly magnetized such that the plasma $\beta = 8\pi nT/B^2$ is low and the electrostatic drift ordering is appropriate for the transverse velocities. The parallel dynamics are governed by the electron and ion equations of motion for a collisional plasma. Plasma blobs that can be described using a magnetic slab geometry where x is the effective radial coordinate, y is the effective poloidal coordinate, and z follows the magnetic field line are considered. In toroidal devices, this represents blobs located in the outer midplane away from magnetic X-points where the toroidal magnetic field is typically much larger than the poloidal field. Additional assumptions made are that the ions are singly charged ($Z = 1$) and cold ($T_i << T_e$), the electrons are isothermal, the polarizing forces can be represented as effective gravity forces, and the Boussinesque approximation can be used. This yields the following set of governing equations:

$$n \frac{e^2 \rho_s^2}{T_e} \frac{d}{dt} \varpi = \nabla_{\parallel} J_{\parallel} - \frac{eg}{\Omega_i} \frac{\partial n}{\partial y}, \tag{2.3}$$

$$\frac{d}{dt} n = \frac{\nabla_{\parallel} J_{\parallel}}{e} - \frac{g}{\Omega_i} \frac{\partial n}{\partial y} - n \nabla_{\parallel} V_{\parallel i}, \tag{2.4}$$

$$J_{\parallel} = \sigma_{\parallel} \left(\frac{T_e}{en} \nabla_{\parallel} n - \nabla_{\parallel} \phi \right), \tag{2.5}$$

$$\frac{d}{dt} V_{\parallel i} = -\frac{c_s^2}{n} \nabla_{\parallel} n, \tag{2.6}$$

where $\rho_s = c_s/\Omega_i$, $c_s = \sqrt{T_e/M_i}$, $d/dt = \partial/\partial t + \mathbf{V}\cdot\nabla$, $\mathbf{V} = \mathbf{V}_\mathrm{E} + V_{\|i}\hat{\mathbf{b}}$, $\mathbf{V}_\mathrm{E} = c\hat{\mathbf{b}}\times\nabla\phi/B$, $\varpi = \nabla_\perp^2\phi$ is the vorticity, $\sigma_\| = ne^2\tau_{ei}/(0.51m_e)$ is the plasma conductivity, $\tau_{ei} = 3m_e^2v_e^{3/2}/(4\sqrt{2\pi}ne^4\ln\Lambda)$ is the electron-ion collision time with $\ln\Lambda \approx 10$ and $v_e = \sqrt{T_e/m_e}$, and g is the effective single particle gravitational acceleration. All other parameters are defined conventionally with respect to cgs units. Some common examples of g are: magnetic field curvature and gradient forces $g_\kappa = 2c_s^2/R_c$ in the outer midplane of tokamaks with radius of curvature R_c, the effective centrifugal force $g_{cent} = V_\theta^2/a$ in linear plasma devices of radius a rotating with velocity V_θ [32], and the neutral wind force $g_{nw} = v_n\nu_{in}$ where v_n is the effective neutral velocity and ν_{in} is the ion-neutral collision frequency [33]. In terms of ion dynamics, the first two terms on the RHS (right hand side) of Eq. 2.4 represents the contribution of the ion polarization drift to the density evolution, which is typically neglected in 2D theory since it is lower order than the E×B advection. However, the ion polarization drift has the important effect of making the drift wave instability well behaved in k-space and must therefore be retained for 3D simulations [30].

The parallel ion velocity and electron current density for sheath connected blobs are matched with that from linear sheath theory at the parallel boundaries $z = \pm L/2$: $V_{\|i,\pm} = \pm c_s$ and $J_\pm = \pm\sigma_\pm\phi_\pm/(L/2)$, where $\sigma_\pm = c_s n_\pm e^2 L/(2T_e)$ is the effective sheath conductivity and $n_\pm$ ($\phi_\pm$) is the density (potential) at the upper(+) and lower(-) sheaths. $\phi_\pm$ is taken with respect to the floating potential $\phi_f \approx 3T_e/e$, which is just a constant reference potential when T_e is constant. To complete the boundary conditions needed to solve Eq.'s (2.3)-(2.6), the standard set of boundary conditions valid for the plasma side of sheaths are employed and the parallel gradient of n, ϖ, and $V_{\|i}$ are all taken as zero at the parallel boundaries [34]. Plasma blobs are considered to be isolated in the drift plane and so, as long as the simulation domain is large enough that the blob remains away from the transverse boundaries, the transverse boundary conditions are insignificant.

The parallel ion equation of motion is presented in the governing equations for consistency with the sheath boundary conditions and to demonstrate exactly how

the parallel ion dynamics enters into both the 2D and 3D models. As mentioned in the Introduction, parallel ion dynamics are ignored in this work and justifications for this will be given throughout the paper.

The 2D sheath limited model is found by assuming that the parallel gradients of density and potential are modest enough that parallel dynamics can be ignored and integrating Eqs (2.3)-(2.4) along the field line using the sheath boundary conditions [18]. In terms of the given parameters, this reduction to 2D can be shown to be valid when the resistance to the charge flow due to the sheath potential is much larger than the collisional resistance in the bulk of the plasma ($\sigma_{\parallel} >> \sigma_{\pm}$) and when the Boltzmann potential that arises due to a varying density profile is negligible with respect to the sheath potential ($\ln(n(z)/n_{\pm}) << e\phi_{\pm}/T_e$). When these conditions are satisifed, the following 2D equations can be obtained:

$$n\frac{e^2\rho_s^2}{T_e}\left(\frac{\partial}{\partial t}+\mathbf{V}_{\mathrm{E}}\cdot\nabla\right)\varpi = \frac{2enc_s}{L}\frac{e\phi}{T_e}-\frac{eg}{\Omega_i}\frac{\partial n}{\partial y}, \tag{2.7}$$

$$\left(\frac{\partial}{\partial t}+\mathbf{V}_{\mathrm{E}}\cdot\nabla\right)n = \frac{2nc_s}{L}\frac{e\phi}{T_e}-\frac{g}{\Omega_i}\frac{\partial n}{\partial y}-\frac{2nc_s}{L}. \tag{2.8}$$

As mentioned previously, the first two terms on the right hand side of Eq. (2.8) represent the contribution of the ion polarization drift to the density evolution and is typically ignored in 2D theory since it is lower order than the E×B drift. The last term in Eq. (2.8) represents the sink of plasma density that results from plasma flowing into the sheaths. This term is also often neglected in 2D theory since the rate of plasma loss to the sheaths is typically much smaller than the rate of radial advection ($2c_s/L << V_{\mathrm{E}}/\delta$). Moreover, if the parallel loss time is smaller than or comparable to the blob advection time, then the blob would not exist anyway. Thus the density evolution equation valid for a 2D analysis is

$$\left(\frac{\partial}{\partial t}+\mathbf{V}_{\mathrm{E}}\cdot\nabla\right)n=0. \tag{2.9}$$

Eq. (2.7) and Eq. (2.9) are the governing equations used in the basic 2D sheath limited blob model where the density is advected with E×B velocity and the potential driven by the effective gravity forces is limited by the ion inertia and the flow of charge into the sheaths at the parallel boundaries [18].

2.2 2D Sheath Limited Theory

I wish to compare the dynamics of plasma blobs from 3D theory and simulations with that from 2D theory and simulations. It is therefore useful to first review the 2D theory of sheath limited plasma blobs. Plasma blobs are typically represented analytically with a Gaussian profile in the plane normal to the magnetic field with an amplitude on the order of or larger than that of the background plasma density, which is usually taken to be homogeneous. The radius of the blob, denoted by δ, is considered to be where the Gaussian profile falls to $1/e$ of its maximum value and is taken to be the characteristic perpendicular gradient scale length.

The characteristic E×B advection rate $\tilde{\omega}_{\mathrm{E}} = \tilde{V}_{\mathrm{E}}/\delta$ depends on the characteristic velocity $\tilde{V}_{\mathrm{E}} = c_s\rho_s(e\tilde{\phi}/T_e)/\delta$, which in turn depends on the characteristic potential $\tilde{\phi}$. The characteristic potential scale $\tilde{\phi}$ is determined from the vorticity equation by balancing the potential source with the potential sinks:

$$\frac{g}{\Omega_i\delta} \sim \frac{2c_s}{L}\frac{e\tilde{\phi}}{T_e} + \frac{\rho_s^3 c_s}{\delta^4}\left(\frac{e\tilde{\phi}}{T_e}\right)^2. \tag{2.10}$$

The LHS of Eq. (2.10) is the potential source due to the effective gravity forces and the terms on the RHS respectively represent the sink of potential through sheath dissipation and inertial dissipation. The physics of the limiting situations when one of the sinks dominates the other will be discussed shortly, but it can be shown that both of the sinks and the source are all on the same order when $\delta = \delta_* \equiv \rho_s\left(gL^2/(4c_s^2\rho_s)\right)^{1/5}$ [25]. The corresponding potential is $e\phi_*/T_e = \sqrt{g}\delta_*^{3/2}/(c_s\rho_s)$. With respect to ϕ_*, the variation of $\tilde{\phi}$ depends only on the dimensionless parameter $\Delta \equiv \delta/\delta_*$. The potential decays with $1/\Delta$ as Δ increases beyond unity and the corresponding advection velocity decreases with $1/\Delta^2$. In the other limit, as Δ decreases from unity, the potential and velocity decrease respectively with $\Delta^{3/2}$ and $\sqrt{\Delta}$.

Eq. (2.10) is only order of magnitude accurate and is merely to demonstrate how the potential and velocity approximately transition from their different scal-

ings in the different limits of Δ. Based on the E×B advection, there seems to be two different sets of fundamental parameters, depending on the size of the blob with respect to the fundamental size δ_*, that are relevant for the normalization of the 2D blob equations. For reasons that will become clear shortly, the characteristic parameters for small blobs ($\Delta < 1$) are the appropriate choice. The potential is order unity for small blobs when normalized by $\omega_g \delta^2/(\rho_s c_s)$, which yields an advection rate of order unity when normalized by the flute mode growth rate $\omega_g = \sqrt{g/\delta}$. In this normalization, the order of magnitude estimates for the potential, velocity, and advection rate are all order unity for $\Delta < 1$ and decay with $1/\Delta^{5/2}$ at large Δ. This is demonstrated in Fig. 3a.

The parameter scalings in Fig. 3a are found by assuming a stable propagating blob. A linear analysis of the governing equations should be addressed to understand the limitations of the scalings given in Fig. 3a. An exact linear analysis of the governing equations with the blob density profile described above representing the background is difficult since this background does not represent a steady state solution of the governing equations due to the effective gravity force combined with the poloidal density gradient. However, the linear modes of importance are flute modes, which can be understood from the standard local linear analysis of the governing equations by considering a background density that is uniform in the poloidal dimension and exponentially decaying in the x-direction $\partial \ln n/\partial x = -1/\delta$. Here, δ is meant to represent the characteristic radius of the blob. The density and potential perturbations are assumed to be of the form $\exp\left[-i\omega t + ik_\perp y\right]$ and the dispersion relation found from Eqs (2.7) and (2.9) is

$$\omega^2 + \omega_g^2 = -i\frac{\Delta^{5/2}}{k_\perp^2 \delta^2}\omega\omega_g. \tag{2.11}$$

Eq. (2.11) is the standard flute mode dispersion relation with the addition of the sink term on the RHS that physically represents the dissipation of potential due to charge flowing through the sheaths. Eq. (2.11) demonstrates how the linear flute modes for varying blob sizes δ are modified by the sheath dissipation. The sheath dissipation is negligible when $\Delta^{5/2}/(k_\perp \delta)^2 << 1$ and the solution of Eq. (2.11) reduces to the conventional wavelength independent flute mode dispersion

relation $\omega = i\omega_g$. The contribution from the vorticity (ω^2) can be neglected when $\Delta^{5/2}/(k_\perp\delta)^2 >> 1$ and the solution is $\omega = i\omega_g k_\perp^2\delta^2/\Delta^{5/2}$. The growth rate as a function of $1/(k_\perp\delta)$ for varying values of Δ is shown in Fig. 3b to demonstrate how the flute mode growth rate for varying values of Δ is modified by the sheath dissipation and how these rates compare to the E×B advection rate shown in Fig. 3a. The growth rates for $\Delta \lesssim 1$ are relatively unaffected by the sheath boundary condition and are more or less independent of the wavelength. So small blobs with $\Delta \lesssim 1$ can be expected to initially propagate radially outward and to be unaffected by flute modes in the early stages of its motion. The situation is opposite for large blobs since, for $\Delta > 1$, the growth rate of all wavelengths smaller than the blob size occur on shorter time scales then the advection time scale.

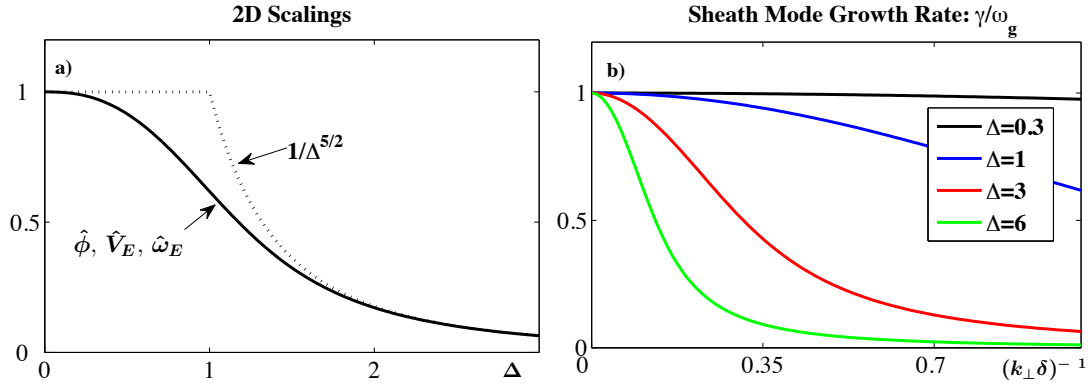

Figure 2.3: a) Order of magnitude scaling of potential, velocity, and advection rate all normalized appropriately for small blobs. b) Sheath mode growth rate γ normalized by ω_g vs perturbation wavelength for varying values of Δ.

The normalization of the 2D blob equations based on the parameters relevant for the advection of small blobs is now seen to be the appropriate normalization for all blob sizes. Although the E×B advection sets the dynamical time scale for small blobs, whereas the small wavelength flute mode instability sets the dynamical time scale for large blobs, both of these phenomena occur on the same relative time scale ω_g^{-1}. The normalized equations are found by normalizing the potential as $e\phi/T_e = \hat{\phi}\omega_g\delta^2/(\rho_s c_s)$, the perpendicular spatial scales as $(x, y) = (\hat{x}, \hat{y})\delta$, and the

time as $t = \hat{t}\omega_g^{-1}$. This yields the following normalized 2D blob equations:

$$\left(\frac{\partial}{\partial \hat{t}} + \hat{\mathbf{V}}_{\mathrm{E}} \cdot \hat{\nabla}\right) \hat{\varpi} = \Delta^{5/2}\hat{\phi} - \frac{1}{\hat{n}}\frac{\partial \hat{n}}{\partial \hat{y}}, \tag{2.12}$$

$$\left(\frac{\partial}{\partial \hat{t}} + \hat{\mathbf{V}}_{\mathrm{E}} \cdot \hat{\nabla}\right) \hat{n} = 0. \tag{2.13}$$

The fact that the dynamics of 2D sheath connected plasma blobs are mainly governed by the single dimensionless parameter Δ is evident when the governing equations are cast into their nondimensional form. The inertial dissipation of charge dominates the sheath dissipation when $\Delta < 1$ and the blob develops a mushroom front as it initially convects radially outward at the flute mode rate ω_g, but quickly becomes unstable to KH (Kelvin-Helmoltz). Physically, this is a result of the strong rotation at the poles as the plasma tries to cancel the charge created from the polarizing forces. On the other hand, the inertial dissipation is negligible when $\Delta > 1$ and the potential is set by the balance of the sheath dissipation with the gravitational forces. The normalized convective rate is longer than the small wavelength flute mode instability by a factor of $\Delta^{5/2}$ and the blob breaks apart into fingers. The most interesting case is when Δ is order unity. In this situation, the KH modes at the poles are balanced by the radial E×B advection and the blob can propagate relatively large distances as a coherent structure.

The physics described above is demonstrated with 2D seeded blob simulations of Eq's (2.12)-(2.13) using the code BOUT++ in Fig. 2.4. The background density n_0 in the simulations is taken to be homogeneous and the blob density n_B is seeded on top of this background with twice the amplitude of the background and a Gaussian profile in the drift plane with Gaussian width δ and Gaussian center x=0, y=0. The initial profile of the total density in nondimensional form is $\hat{n} = 1 + 2\exp\left[-\hat{x}^2 - \hat{y}^2\right]$. It should be mentioned that, even though the hats have been left off of the quantities in Fig. 2.4, the quantities in Fig. 2.4 are normalized as discussed in the text.

It is worth mentioning here that the dynamics of blobs predicted by Eqs (2.12)-(2.13) is also dependent on the ratio of the background density to the blob

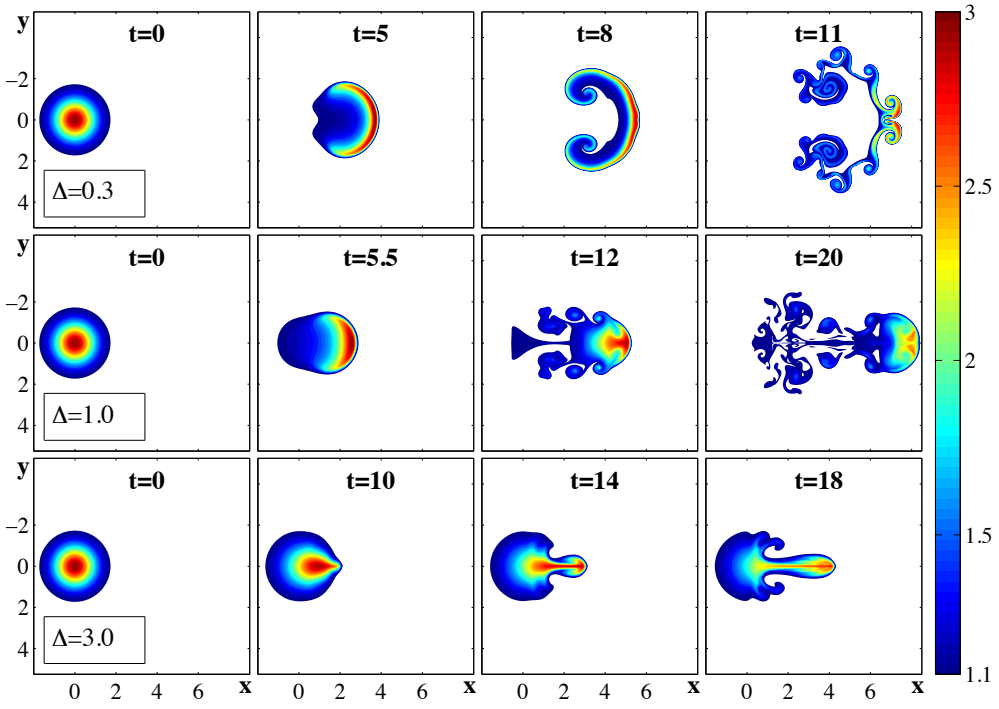

Figure 2.4: Time slices of density contours from 2D Simulations for a small blob with $\Delta = 0.3$ (top), medium blob with $\Delta = 1.0$ (middle), and large blob with $\Delta = 3.0$ (bottom).

density n_B/n_0. This is because the background density n_0 only enters in the denominator of $n^{-1}\partial n/\partial y \sim n_B/(n_0 + n_B)$. An exact solution of Eqs (2.12)-(2.13) can be found in the limit where $n_B >> n_0$ and the poloidal profile of n_B is Gaussian. This limit corresponds to a blob in a vacuum and the solution, first demonstrated in [18], shows that the blob will retain its original form in the frame moving with a constant E×B velocity and is independent of the profile of the blob in the x direction. A blob in a vacuum is not a realistic situation, but this solution provides an upper bound for the advection rate of sheath limited plasma blobs. However, this solution does not really apply to large blobs ($\Delta > 1$) since it relies on the overall stability of the blob on time scales short compared to the E×B advection time.

With respect to the simulation of large blobs ($\Delta > 1$), it should be mentioned that the onset of the flute mode instability is delayed due to the symmetry

of the initial density profiles. The perturbations are not seeded, but instead are allowed to develop naturally during the simulation and most likely arise due to numerical error. This means that different numerical schemes could produce different perturbations and therefore different simulation results. Furthermore, since smaller wavelengths have larger growth rates, the coarseness of the grid can also influence the modes seen in the simulation. Different grid refinements and numerical schemes were performed and the details of the simulation for large blobs were indeed different. However, the observation that the blob breaks apart via small wavelength interchange modes on a time scale short compared to the advection time scale remains the same.

2.3 Effects of Parallel Electron Dynamics

To build upon the 2D model and extend it to 3D, only physical processes that can have time scales comparable to or less than the fundamental 2D time scale ω_g^{-1} are considered. It was argued in the previous section that the E×B advection must occur at much faster rate than the parallel loss rate in order for the blob to exist and propagate ($2c_s/L << \omega_g$). Furthermore, ion sound waves typically occur on time scales much longer than flute modes ($c_s k_\parallel << \omega_g$) and only modestly varying parallel profiles such that the parallel advection is also negligible ($c_s|\nabla_\parallel \ln(n)| << \omega_g$) are considered. For these reasons, parallel ion dynamics are ignored in the 3D analysis and the focus is only on how parallel electron dynamics alter blob dynamics from that predicted by 2D theory.

The vorticity and density equations used in the 3D analysis given here are obtained from Eqs (2.3)-(2.4) by neglecting the parallel ion dynamics [30]:

$$n\frac{e^2\rho_s^2}{T_e}\left(\frac{\partial}{\partial t}+\mathbf{V}_\mathrm{E}\cdot\nabla\right)\varpi = \nabla_\parallel J_\parallel - \frac{eg}{\Omega_i}\frac{\partial n}{\partial y}, \tag{2.14}$$

$$\left(\frac{\partial}{\partial t}+\mathbf{V}_\mathrm{E}\cdot\nabla\right)n = \frac{\nabla_\parallel J_\parallel}{e} - \frac{g}{\Omega_i}\frac{\partial n}{\partial y}. \tag{2.15}$$

2.3.1 Drift Waves

A 3D analysis of plasma blobs is began by considering initial density profiles that are homogeneous along the magnetic field line. The new linear 3D physics that enters are resistive drift waves. It was shown in the analysis of the 2D equations that the dominant linear flute modes occur at wavelengths smaller than the blob size and on time scales short compared to the blob advection rate. This separation in scales is justification for the applicability of the results from a standard local linear analysis of an exponentially decaying slab density to the linear modes present on large blobs. Similar arguments are applicable for the linear analysis of drift waves in the 3D equations. Linear resistive drift waves are known to oscillate at a rate on the order of the drift frequency $\omega_* = c_s k_\perp \rho_s/\delta$ and to have maximum growth rates when $k_\perp \rho_s \approx 1$ [35]. On the other hand, the fundamental blob size δ_* is typically an order of magnitude larger than ρ_s and the blob advection rate is on the order of the flute mode growth rate $\omega_g = \sqrt{g/\delta}$, which, for most relevant values of g, is less than ω_*. For example, the drift wave frequency is larger than the advection rate by a factor of $\sqrt{R_c/(2\delta)} \sim 10$ for blobs in the outer midplane of toroidal devices ($g = 2c_s^2/R_c$) with typical blob diameters 2δ on the cm scale and machines with radius of curvature R_c on the meter scale.

Consider the same exponentially varying density slab and linear modes as was assumed in the previous section for the 2D linear analysis with the additional assumption that the perturbations also have some arbitrary parallel profiles that satisfy the sheath boundary conditions. With some algebraic manipulations, the 1D equation governing the parallel profiles from Eqs (2.14), (2.15), and (2.5) along with the sheath boundary conditions are

$$\nabla_\parallel^2 \hat{\phi}(z) = k_\parallel^2 \hat{\phi}(z), \tag{2.16}$$

$$-\nabla_\parallel \hat{\phi}(z) \mid_{z=\pm L/2} = \pm \frac{2}{\sigma L} \hat{\phi}(z) \mid_{z=\pm L/2}, \tag{2.17}$$

where $\sigma = \sigma_\parallel/\sigma_{sh} = 2v_e\lambda_e/(c_s L)$ is the ratio of the parallel conductivity to the sheath conductivity with $\lambda_e = v_e\tau_{ei}/0.51$ the electron mean free path, and the

constant $k_\parallel$ is defined as

$$k_\parallel = \sqrt{\frac{\chi^2\left[\omega^2+\omega_g^2\left(1-\frac{\omega}{\omega_*}\chi^2\right)\right]}{i\lambda_e v_e\left[\omega\left(1+\chi^2\right)-\omega_*\right]}}, \tag{2.18}$$

where $\chi = \rho_s k_\perp$.

The function for the eigenmodes supported in this system is found from the general solution of Eq. (2.16) with the sheath boundary condition (Eq. (2.17)). The general solutions of Eq. 2.16 are in the form of hyperbolic sines and cosines. After implementing the boundary conditions given in Eq. 2.17, the following dispersion relations are obtained:

$$ik_\parallel \tan\left[ik_\parallel L/2\right] = \frac{2}{\sigma L}, \tag{2.19}$$

$$ik_\parallel \cot\left[ik_\parallel L/2\right] = \frac{-2}{\sigma L}. \tag{2.20}$$

Eq. (2.19) corresponds to even eigenmodes and Eq. (2.20) corresponds to odd eigenmodes. If it is assumed that $\sigma k_\parallel L/2 >> 1$, then one can use the Taylor expansions $\arctan[x] \approx m\pi + x$ and $\operatorname{arccot}[x] \approx (m+1/2)\pi - x$ to simplify the dispersion relation to

$$\omega^2 + \omega_g^2 - \omega\frac{g\chi}{c_s} = -i\omega_{sh}\omega, \qquad \text{for } m = 0 \tag{2.21}$$

$$\omega^2 + \omega_g^2 - \omega\frac{g\chi}{c_s} = -i\omega_\parallel\left[\omega - \frac{\omega_*}{1+\chi^2}\right], \text{ for } m \in Z^+ \tag{2.22}$$

where $\omega_{sh} = \nu_{sh}/\chi^2$ with $\nu_{sh} = 2c_s/L$ the sheath loss rate, $\omega_\parallel = \nu_\parallel(1+\chi^2)/\chi^2$ with $\nu_\parallel = v_e\lambda_e k_\parallel^2$ the characteristic rate for electrons to diffuse a distance on the order of a parallel wavelength, and $k_\parallel = \pi \mathrm{m}/L$. Here, m refers to the number of half wavelengths and even (odd) values of m correspond to even (odd) modes.

The last term on the LHS of both Eq. (2.21) and Eq. (2.22) is the contribution of the ion polarization drift in the density evolution to the standard flute mode dispersion relation. With the exception of this term, which was neglected in the 2D analysis, the m=0 mode is exactly the 2D sheath limited mode given in Eq. (2.11). Notice that the m=0 mode is the only mode where the sheath boundary

conditions play a role in the limit where $|\sigma k_\| L/2| >> 1$. The other modes are the same as finite local modes with zero gradient boundary condition. A physical interpretation of this limit is merely an extension of the condition considered to ignore the parallel gradients that arise due to a finite parallel resistivity in the reduction to 2D theory. Here, the 2D limit allows us to ignore the coupling of the sheath boundary condition with the parallel modes as long as the parallel wavelength of the modes are smaller than the characteristic gradient scale of the background that arise due to the finite plasma resistivity. Since $k_\| = 0$ for m=0, one would expect the boundary conditions to enter into the m=0 dispersion relation.

In addition to the assumption that $\sigma > 1$, it is also implicitly assumed for the validity of 2D theory that the rate of 3D instabilities are small compared to the 2D convection rate ω_g. The growth rate from Eq. 2.21 is never larger than ω_g since Eq. 2.21 is the 2D sheath limited dispersion relation. Eq. 2.22 is a combination of both drift and flute modes, but the drift wave contribution to the growth rate can be shown to dominate the flute modes as long as $\omega_*/(1+\chi^2) > \omega_g$. In this limit, the maximum growth rate as a function of $k_\|$ and the equation for the corresponding parallel wavenumber where the maximum growth occurs are found to be

$$\gamma_{max} \approx \frac{0.3\omega_*}{1+\chi^2} = \frac{0.3c_s}{\sqrt{g\delta}}\frac{\chi}{1+\chi^2}\omega_g. \tag{2.23}$$

$$\omega_{\|,max} \approx \frac{\omega_*}{1+\chi^2}. \tag{2.24}$$

Eq. 2.23 has an absolute maximum in k space when $\chi = 1$ and suggests that blob transport may deviate from 2D theory due to drift waves when $0.15c_s/\sqrt{g\delta} \gtrsim 1$.

The χ^2 terms in the factors of $1+\chi^2$ in Eqs (2.23)-(2.24) physically come from the contribution of the ion polarization drift to the density evolution [35]. Without this term, the maximum growth rate and corresponding parallel wavenumber would scale with χ respectively as $\gamma_{max} \propto \chi$ and $k_{\|,max} \propto \chi^{3/2}$. Thus, the perpendicular wavelength and parallel mode number corresponding to the maximum growth rate would both increase as the grid is refined. This is not physical and so the contribution of the ion polarization drift to the density evolution, though not important for 2D studies, must be retained in a 3D analysis.

To examine Eq. (2.22) in more detail, let's reduce our attention to blobs that may be found in the outer midplane of tokamaks ($g = 2c_s^2/R_c$). This gives $\gamma_{max}/\omega_g \approx 0.3\sqrt{R_c/(2\delta)}$ and thus the maximum growth rate only depends on the ratio of the radius of curvature of the device to the transverse size of the blob. To see what the dispersion relation might look like for different size blobs and different values of R_c, consider two different sets of parameters; a set that may be typical for current tokamaks: $T_e = 20$ eV, $B = 3$ T, $n_0 = 3 \times 10^{12}$ cm^{-3}, $R_c = 150$ cm, and a set that may be typical of future tokamaks: $T_e = 50$ eV, $B = 4$ T, $n_0 = 1 \times 10^{13}$ cm^{-3}, $R_c = 800$ cm. The relation $L = 10R_c$ is also assumed since the parallel scale length in tokamaks is typically $L \approx q\pi R_c$ with safety factor $q \approx 3$. The real and imaginary solutions of Eq. (2.22) normalized by the 2D advection rate ω_g is plotted in Fig. 2.3 for a small, medium, and large blob using the parameters typical of current devices and for a medium blob using the parameters typical of future devices. Recall that ω_g is to be interpreted as the rate at which the the blob is unstable to flute modes for large blobs rather than as the advection rate.

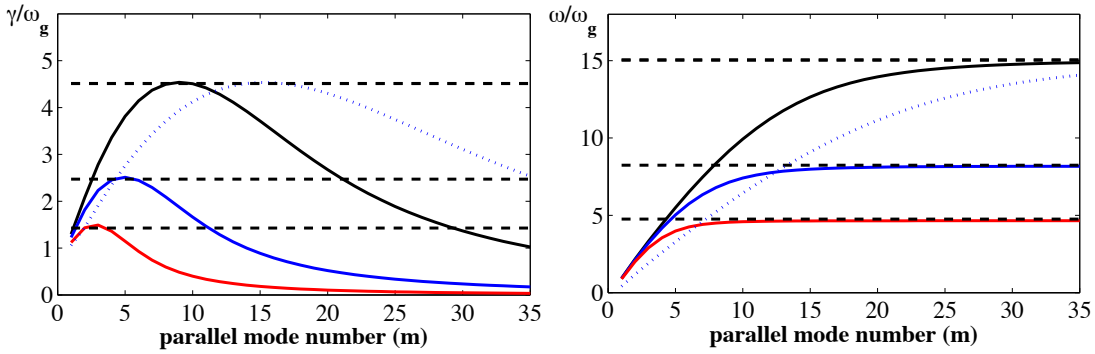

Figure 2.5: Solutions of Eq. 2.22. The growth rate (top) and real frequency (bottom) normalized by the 2D convective rate are plotted versus the parallel mode number m. The solid black curve, solid blue curve, and solid red curve are respectively for $\Delta = 0.3$, $\Delta = 1.0$, and $\Delta = 3.0$ at $\rho_s k_\perp = 1$ using the parameter set typical of current tokamaks. The .. blue curve was calculated for a $\Delta = 1$ blob using parameters typical for future tokamaks. The corresponding maximum growth rate given by Eq. (2.23) is shown by the corresponding - - lines of the same color. The corresponding maximum real frequency that the curves saturate to at large parallel mode number correspond to $\omega = \omega_*/\left(1+\chi^2\right)$ [36].

Unlike the standard flute modes, which have a purely imaginary solution and are thus purely growing modes, drift waves have both a real and imaginary part to the solution of the dispersion relation and therefore travel as they grow. Drift waves propagate in the electron diamagnetic direction with a frequency on the order of the drift frequency ω_*. As seen in Fig. 2.5b, the rate of propagation of these waves can be up to an order of magnitude larger than the blob advection rate. In order to accurately capture the effect of drift waves on plasma blobs as they propagate using a 3D numerical algorithm, one must resolve the time scale of the propagation of these waves. This can significantly increase the time required to perform a 3D numerical simulation with respect to 2D simulations due to the large disparity in these time scales. The rate of these waves is relatively larger than the advection rate for smaller blobs since $\omega_* \sim 1/\delta$ whereas $\omega_g \sim 1/\sqrt{\delta}$. Moreover, more grid points along the field line are required for smaller blobs since the parallel mode number corresponding to the maximum growth rate scales with $1/\sqrt{\delta}$.

For the purpose of comparing 2D and 3D seeded blob simulation results and the development of linear resistive drift waves on plasma blobs with that predicted by the simplified linear analysis, first consider the following non-dimensional transformation: $(x, y) = \delta(\hat{x}, \hat{y})$, $z = (L/2)\hat{z}$, $t = \omega_g^{-1}\hat{t}$, $\phi = \sqrt{g\delta^3/(c_s\rho_s)^2}T_e\hat{\phi}/e = \tilde{\phi}\hat{\phi}$, $n = \tilde{n}\hat{n}$, and $J_\parallel = e^2 c_s \tilde{n}\tilde{\phi}/T_e\hat{J}_\parallel$. The dimensionless form of Eq. 2.3 and Eq. 2.4 along with parallel Ohm's law are

$$\hat{n}\frac{d}{d\hat{t}}\hat{\nabla}_\perp^2\hat{\phi} = \Delta^{\frac{5}{2}}\hat{\nabla}_\parallel\hat{J}_\parallel - \frac{\partial\hat{n}}{\partial\hat{y}}, \tag{2.25}$$

$$\frac{d}{d\hat{t}}\hat{n} = \frac{\rho}{\sqrt{\alpha\Delta}}\left(\Delta^{\frac{5}{2}}\hat{\nabla}_\parallel\hat{J}_\parallel - \frac{\partial\hat{n}}{\partial\hat{y}}\right), \tag{2.26}$$

$$\hat{J}_\parallel = \sigma\hat{\nabla}_\parallel\left(\frac{\rho}{\sqrt{\alpha^3\Delta^3}}\ln(\hat{n}) - \hat{\phi}\right), \tag{2.27}$$

where $d/d\hat{t} = \partial/\partial\hat{t} + \hat{z}\times\hat{\nabla}\hat{\phi}\cdot\hat{\nabla}$, $\rho \equiv g\rho_s/c_s^2$, $\sigma \equiv \hat{n}_\pm\sigma_\parallel/\sigma_\pm = \hat{n}\lambda_e\sqrt{M_i/m_e}/(L/2)$, and $\alpha \equiv g\delta_*/c_s^2$. The sheath boundary conditions in the dimensionless representation are $\hat{J}_\parallel(\hat{z} = \pm 1) = \pm\hat{n}_\pm\hat{\phi}_\pm$. The 2D operator $\hat{\nabla}_\parallel\hat{J}_\parallel = \hat{n}\hat{\phi}$ is used in Eq. 2.25-2.26 for the 2D simulations. The only difference between the 2D simulations presented here and those presented earlier in the paper is that the ion polarization drift is now retained in the density evolution (which should not affect the

2D simulations much) in order to have a one-to-one correspondence to the results from the 3D simulations. The initial density profiles for the 3D simulations are uniform along the field line with the 2D profiles the same as was used for the 2D simulations presented previously.

It should be mentioned that the hats used here to represent the dimensionless variables have been dropped from the terms in the figures for simplicity. The results from 2D and 3D seeded blob simulations for a $\Delta = 1$ blob using the parameter set given previously that may be characteristic of current tokamaks are shown in Fig. 2.6. The 2D density profiles from the 3D simulations represent the density averaged along the field line. Notice that the averaged density along the field line from the 3D simulation (bottom) matches well with the 2D simulation (top) at early stages in the 2D convection, but the onset of drift waves can be seen by looking at the individual slices along the field line shown in Fig. 2.7. At later times, the 3D simulation yields a blob that is much more diffuse with a greatly reduced radial velocity.

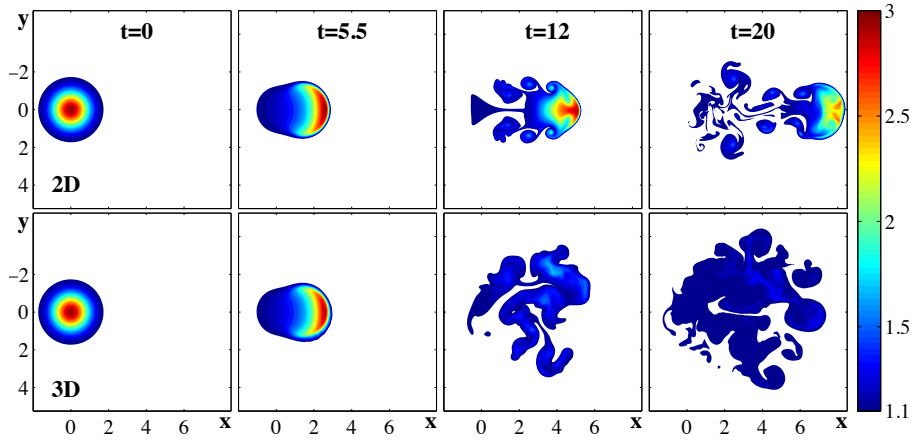

Figure 2.6: Time slices of density contours from 2D simulation (top) and 3D simulation (bottom) for $\Delta = 1.0$ blob using parameters typical of current tokamaks: $\rho = 2.87\times10^{-4}$, $\sigma = 32.3$, and $\alpha = 3.68\times10^{-3}$. The 2D contours from the 3D simulation are the averaged values along the field line (enhanced online). Reprinted with permission from J. Angus, M. Umansky, and S. Krasheninnikov, Phys. Rev. Lett. 108, 215002 (2012). Copyright 2012, American Physical Society.

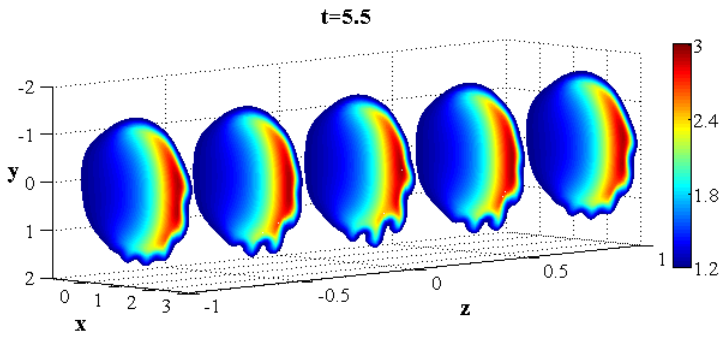

Figure 2.7: 2D density contours from 3D simulation taken at different slices along the magnetic field line corresponding to the averaged density contour shown at t=5.5 in Fig. 2.6. Reprinted with permission from J. Angus, M. Umansky, and S. Krasheninnikov, Phys. Rev. Lett. 108, 215002 (2012). Copyright 2012, American Physical Society.

The results of 2D and 3D seeded blob simulations for a $\Delta = 0.3$ blob and a $\Delta = 3.0$ blob using parameters typical of current devices are shown in Fig. 2.8 and Fig. 2.9, respectively. The $\Delta = 0.3$ blob is seen to be affected by the drift waves at a relatively earlier time than the $\Delta = 1$ blob, whereas the $\Delta = 3.0$ blob is relatively unaffected by the drift wave instability. Both of these results agree qualitatively well with the linear analysis given in Fig. 2.5.

The results from the standard local linear analysis gives a qualitatively good description of how drift waves affect plasma blobs, but to gain a better understanding of the modes that affect plasma blobs and the limitations of using the standard local linear analysis to describe these modes, it is useful to analyze the development of the drift wave modes in more detail. The mode structure of the dominant unstable drift wave mode corresponding to the 3D simulation in Fig. 2.6 is shown in Fig. 2.10 where the development of a wave with parallel mode number six and normalized perpendicular wavelength such that $\chi \approx 0.5$ is seen. Both of these values agree qualitatively well with that predicted by the local linear theory. The results of the linear analysis shown in Fig. 2.5 also suggest that the parallel mode number corresponding to the maximum growth rate for a $\Delta = 1$ blob using the parameters characteristic of future tokamaks should be about twice as large as that for parameters typical of current devices. This result is also found in the

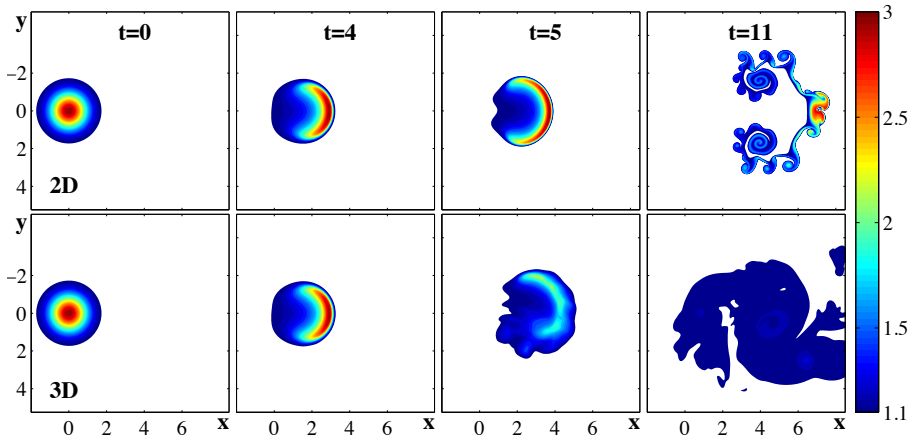

Figure 2.8: Time slices of density contours from 2D simulation (top) and 3D simulation (bottom) for $\Delta = 0.3$ blob using parameters typical of current tokamaks: $\rho = 2.87\times10^{-4}$, $\sigma = 32.3$, and $\alpha = 3.68\times10^{-3}$. The 2D contours from the 3D simulation are the averaged values along the field line (enhanced online). Reprinted with permission from J. Angus, M. Umansky, and S. Krasheninnikov, Phys. Rev. Lett. 108, 215002 (2012). Copyright 2012, American Physical Society.

seeded blob simulations of a $\Delta = 1$ blob with future-like parameters shown in Fig. 2.11 where a parallel mode number of 12 is seen. The dominant perpendicular wavelength shown in Fig. 2.11 is such that $\chi \approx 0.7$.

The linear analysis also predicts that the growth rate for a $\Delta = 1$ blob with the future-like parameters should be larger than that for a $\Delta = 1$ blob with the current-like parameters. A 3D background density is required in order to extract the growth rates from the simulations. This background is obtained by first recognizing that the drift wave instability is a consequence of the density dependence in Ohm's law and is physically a result of the phase delay between the potential and density that arises due to the finite parallel resistivity that the electrons experience while trying to set up a perfect Boltzmann relation along the field line. If the density dependence in Ohm's law is ignored, then the plasma will just develop a slight parallel density gradient as it propagates radially due to the finite resistivity, but will be stable with respect to the drift wave instability. With the exception of the drift wave density perturbations, the blob density evolution

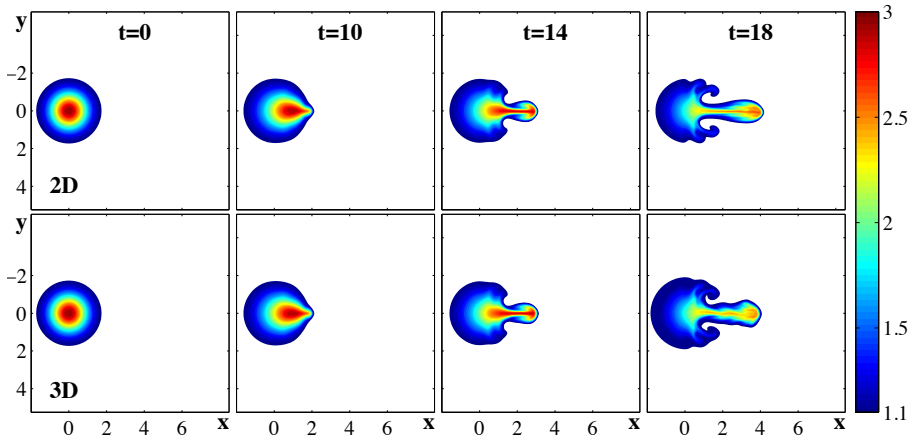

Figure 2.9: Time slices of density contours from 2D simulation (top) and 3D simulation (bottom) for $\Delta = 3.0$ blob using parameters typical of current tokamaks: $\rho = 2.87\times10^{-4}$, $\sigma = 32.3$, and $\alpha = 3.68\times10^{-3}$. The 2D contours from the 3D simulation are the averaged values along the field line (enhanced online).

during the linear stage of drift waves should develop very similar to the density profile that would be found by ignoring the pressure in Ohm's law in the limit where $\sigma > 1$. Therefore, to solo out the density perturbations from the total density profiles shown in Figs 2.10-2.11, identical simulations are performed by ignoring the pressure in Ohm's law and then subtract these density profiles from the full 3D profiles. The maximum growth rates, shown in Fig. 2.12, are then determined from the slope of the natural logarithm of the maximum density perturbations versus normalized time.

The results shown in Fig. 2.12 demonstrate linear growth corresponding to the time between the time slices shown in Fig. 2.10 for the current-like blob and in Fig. 2.11 for the future-like blob. However, even though the onset of the dominant unstable mode for the future-like blob occurs at a relatively earlier time for the current-like blob, the growth rate is actually larger for the current-like blob than for the future-like blob. This is in contrast to that predicted by the local linear analysis and is most likely due to the fact that the front of the radial density profile steepens as the blob convects radially outward [23]. Since the current-like blob propagates relatively further than the future-like blob before the instability

sets in, the actual radial density gradient of the blob when the instability develops is much larger than the initial density gradient used to calculate the maximum growth rates shown in Fig. 2.5. There does appears to be a slowly growing linear mode in the current-like blob that develops around the same normalized time as the dominant mode in the future-like blob, but this mode is not strong enough to dissipate the blob before a more dominant mode develops.

The 2D contour slices in the drift plane shown in Figs 2.7, 2.10, and 2.11 all show the drift wave perturbations on the bottom half of the radial front of the blob. The waves actually develop around the vertical center of the blob where the density gradient is sharpest, but they travel in the electron diagmagnetic direction and therefore end up on the bottom half. The waves are then stretched out there along with the 2D KH modes and lose their free energy source as they rotate to the backside of the blob where the poloidal density gradient is much weaker.

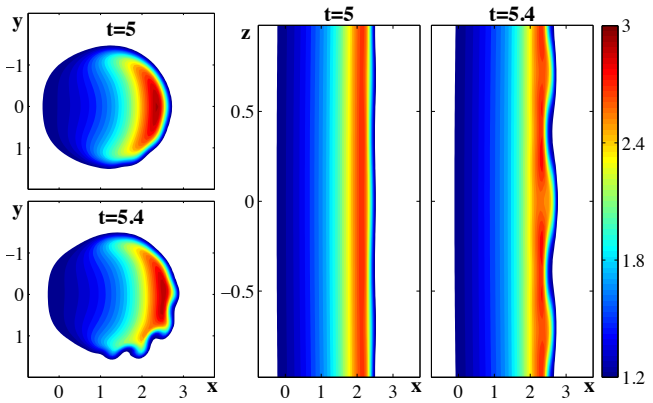

Figure 2.10: Time slices of density contours in the drift plane (left) and along B (right) for $\Delta = 1.0$ blob using parameters typical of current tokamaks: $\rho = 2.87 \times 10^{-4}$, $\sigma = 32.3$, and $\alpha = 3.68 \times 10^{-3}$. The 2D contours in the drift plane are taken at $z = 0$ and the 2D contours along B are taken at $y = -0.76$. The development of drift waves in the drift plane at $y = 0$ is demonstrated in movie format (enhanced online). The time between frames is slowed down during the development of the drift waves in the movie since they occur on a time scale much smaller than the advection time.

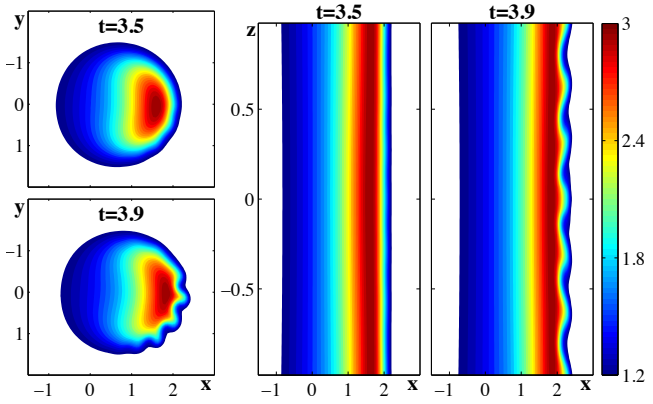

Figure 2.11: Time slices of density contours in the drift plane (left) and along B (right) for $\Delta = 1.0$ blob using parameters typical of future tokamaks: $\rho = 6.4\text{E} - 5$, $\sigma = 11.4$, and $\alpha = 1.1 \times 10^{-3}$. The 2D contours in the drift plane are taken at $z = 0$ and the 2D contours along B are taken at $y = 0$. The development of drift waves in the drift plane at $y = 0$ is demonstrated in movie format (enhanced online). The time between frames is slowed down during the development of the drift waves in the movie since they occur on a time scale much smaller than the advection time.

2.3.2 Boltzmann spinning

The effect of drift waves on plasma blobs was analysed in the previous section by assuming a density profile that was initially uniform along the field line. This is the most basic extension of the conventional 2D model to 3D, but a more physically accurate model would be one with a varying profile along the field line. The blob density could be expected to decrease from the center to the parallel boundaries owing to the loss of plasma through the sheaths. Moreover, plasma in the edge region of tokamaks is known to sometimes exhibit strong ballooning-like characteristics [24].

A parallel density gradient will set up a parallel varying Boltzmann-like potential along the field line. This Boltzmann potential will also have a radially variation through its dependence on the radially varying blob density. (The use of the term "radial" here is not to be confused with the effective radial coordinate x. Here, "radial" refers to the radial distance with respect to polar coordinates

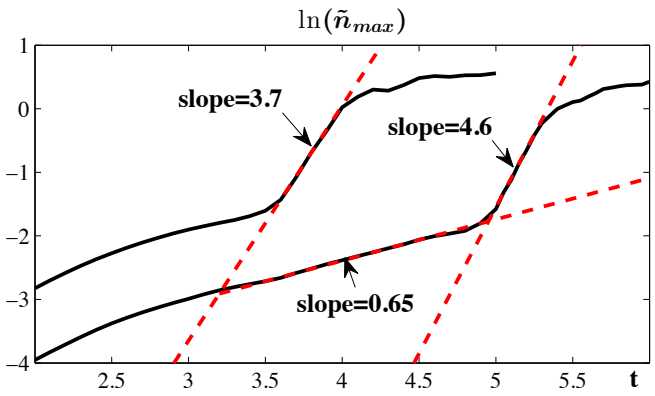

Figure 2.12: Logarithm of maximum density perturbation from simulations vs normalized time to demonstrate linear growth rate. The curve which demonstrates a normalized linear growth rate of 3.7 corresponds to the $\Delta = 1$ blob using the future-like edge parameters displayed in Fig. 2.10. The other curve correspond to the $\Delta = 1$ blob using the current-like edge shown in Fig. 2.11.

from the center of the plasma blob.) This radially varying potential will produce an E×B drift that will spin the blob about its center and thereby mix the positive and negative charge created from the effective gravity forces - thus providing an additional sink of the 2D sheath potential.

To see how the Boltzmann potential modifies the conventional sink-source relation for the 2D potential (Eq. 2.10), the parallel profiles are assumed to be modest enough that the vorticity equation can be integrated along the field line (the same way that was done to reduce the 3D equations to 2D in Section II) by estimating the potential and density integrals as $\int_z^{L/2} f(z')dz' \approx f(z)(L/2 - z)$. For simplicity, it is also assumed that everything is symmetric along the field line such that $f(z) = f(-z)$ and $f(z = L/2) = f(z = -L/2) = f_{sh}$ for some arbitrary function $f(z)$. The potential drop along the blob as a function of z with modestly varying profiles and in the limit where $\sigma_{\parallel}/\sigma_{sh} >> 1$ can be shown to be a linear combination of the sheath and Boltzmann potentials: $e\phi(z)/T_e = e\phi_{sh}/T_e + \ln(n(z)/n_{sh})$. The sink-source relation for the 2D sheath potential now

becomes

$$\frac{g}{\Omega_i \delta} \sim \frac{n_{sh}}{n(0)} \frac{2c_s}{L} \frac{e\phi_{sh}}{T_e} + \frac{\rho_s^3 c_s}{\delta^4} \left(\frac{e\phi_{sh}}{T_e} + \ln\left(\frac{n(0)}{n_{sh}}\right) \right) \frac{e\phi_{sh}}{T_e}, \tag{2.28}$$

where $n(0) = n(z = 0)$ is the maximum initial density in the center between the parallel boundaries.

Eq. (2.28) is exactly the same as Eq. (2.10) when $n(0) = n_{sh}$. When $n(0) \neq n_{sh}$, then the sheath dissipation term scales with $n_{sh}/n(0)$ and there is an additional inertial sink of the 2D potential coming from the Boltzmann potential. As discussed earlier in Section III, The inertial dissipation dominates the sheath dissipation for small blobs with $\delta < \delta_*$. Thus, the deviation of blob dynamics from that predicted by 2D theory for small blobs can be expected to occur when the Boltzmann potential becomes comparable to the conventional 2D potential. More physically, spinning can be expected to affect the 2D dynamics of small blobs when the rate of dissipation of the polarized charge from spinning becomes comparable to the rate of the polarized charge dissipation through pole rotation. Since both of these dissipation mechanisms are due to a corresponding E×B velocity, the relative importance of spinning on small blobs is found by comparing the Boltzmann potential with the conventional 2D potential. Moreover, since both of the conventional 2D potential sink terms are on the same order for medium blobs, then the same condition for the relative importance for small blobs can apply to medium blobs as well. The order of magnitude accurate 2D potential for small and medium blobs from 2D theory is $e\phi_{sh}/T_e \approx \sqrt{g\delta/c_s^2}\delta/\rho_s$ and the condition for the importance of blob spinning can be expressed as

$$\ln\left(\frac{n}{n_{sh}}\right) \gtrsim \frac{\delta}{\rho_s}\sqrt{\frac{g\delta}{c_s^2}}, \qquad \text{for} \qquad \delta \lesssim \delta_* \ . \tag{2.29}$$

How the Boltzmann potential compares with the order of magnitude estimate for the 2D potential as a function of $n(0)/n_{sh}$ for a small and medium blob using the current-like parameters from the previous sections is shown in Fig. 2.3. The order of magnitude estimate for the 2D potential for the medium blob given in Eq. 2.29 is scaled by the factor shown in Fig. 2.3 for a more accurate approximation.

3D seeded blob simulations of Eqs. 2.25-2.27 with initial normalized density

profiles of the form $\hat{n} = 1 + 2\exp\left(-\hat{x}^2 - \hat{y}^2\right)\exp\left(-\left(\hat{z}/\Delta z\right)^2\right)$ to demonstrate how the 2D blob dynamics are altered by an initially varying density profile along the field. The results of how the 2D potential profile looks at early times and how the early stage evolution of the blob is modified by the Boltzmann potential as $n(0)/n_{sh}$ increases for a small blob and medium blob are shown in Fig. 2.14 and Fig. 2.15 respectively.

The conclusion that the relative importance of spinning on small and medium blobs can be estimated by comparing the Boltzmann potential with the conventional 2D potential scale is supported by the results shown in Figs 2.14-2.15. The small blob has a smaller 2D potential magnitude than the medium blob and thus becomes susceptible to the effects of spinning with more modest parallel profiles than for the medium blob. Notice that the potential and density contour lines almost perfectly overlap for the $\Delta z = 0.5$ case in Fig. 2.29, demonstrating the the potential is almost purely Boltzmann. Furthermore, it appears that even a modest initially varying profile, where spinning is not quite important, still allows for the development of the drift wave instability at early stages in the blob advection. This can be seen by comparing the last time slice for $\Delta z = 2.0$ shown in Fig. 2.15 with the corresponding time slice shown in Fig. 2.10. The reduced radial convection with increasing $n(0)/n_{sh}$ is a result of the spinning mixing the polarized charge and the onset of poloidal convection is due to the rotation of the diminished polarized potential to a different angle with respect to the 2D plane. Both of these results are analogous to that found for nonthermalized spinning blobs discussed in [21].

One difference between the spinning of nonthermalized sheath connected plasma blobs and spinning due to a Boltzmann potential when the blob has some initially varying density profile is that, because the Boltzmann potential varies along the field line, the spinning rate also varies along the field line. So Boltzmann spinning is a full 3D effect - whereas the spinning rate for nonthermalized blobs is a purely 2D effect. The full 3D nature of the spinning is demonstrated in Fig. 2.16 by showing several different cross sections of the density contours in different planes for a small blob with $\Delta z = 0.5$. The implications of having a parallel varia-

tion of the spinning is not examined and detail here, but will be discussed further in the conclusion of this paper.

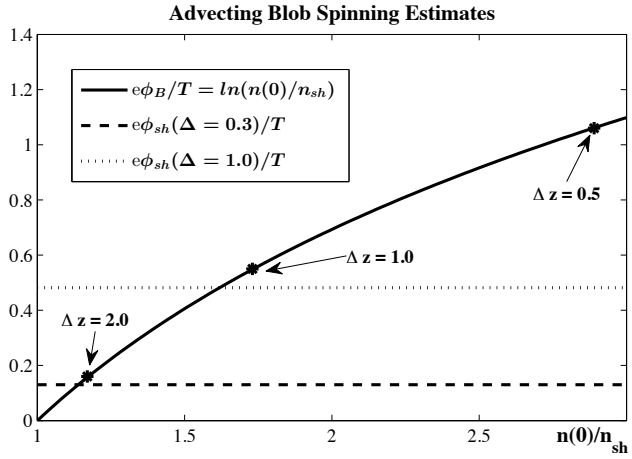

Figure 2.13: Relative importance of spinning on advecting ($\Delta \lesssim 1$) blobs. Spinning is important when $\phi_B \gtrsim \phi_{sh}$. Parameters used for ϕ_{sh} are same parameters used in previous section for current-like tokamaks.

Determining the relative importance of spinning for large blobs is a bit different than that of small and medium blobs. This is because the dynamical time scale for large blobs is set by the small wavelength flute instability rather than by the E×B advection rate. It has been shown in [37] that blob spin can stabilize the flute mode instability, but can also lead to a rotational instability. How spinning affects large blobs is demonstrated in Fig. 2.17 using the current-like parameters. Here it is seen that even a slight deviation in the 2D potential seems to stabilize small wavelength flute instabilities, but a larger wavelength mode still develops. It also appears that the developing finger gets spun up, similar to how the entire blob does for medium and small blobs, when the Boltzmann potential become comparable to and greater than the 2D potential. These are just a qualitative description of what is seen in the simulations. A more detailed and quantitative description of how spinning affects large blobs is deferred to a future paper.

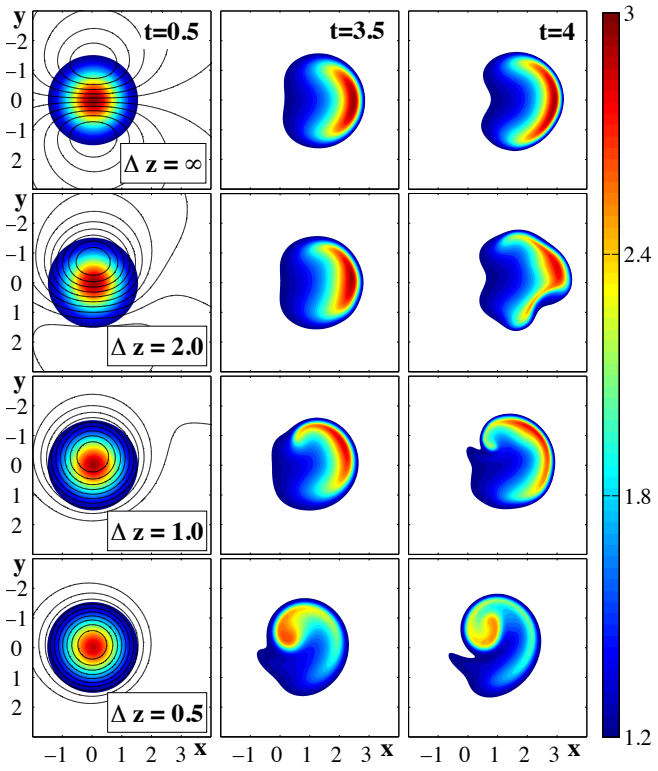

Figure 2.14: Comparison of small blob ($\Delta = 0.3$) evolution for varying initial parallel density profiles. The 2D contours are taken at $z = 0$. The solid contour lines shown in the first time slices represent the 2D potential structure.

2.4 Discussion and Conclusion

The standard 2D sheath connected model of plasma blobs driven by effective gravity forces is extended to 3D by including the electrostatic parallel electron and ion equations of motion under the assumptions of high collisionality, cold ions, and isothermal electrons. The conventional relation between the parallel current density and the potential from linear sheath theory used in the 2D model is implemented as boundary conditions in our 3D model. The new physics that enters from parallel ion dynamics are ion sound waves and parallel advection. The new physics that enters from parallel electron dynamics is the resistive bowing of the parallel profiles, the resistive drift wave instability, and Boltzmann spinning. For the modestly varying parallel profiles examined in this work, parallel ion dynamics occur on time scales much longer than that of parallel electron dynamics and only

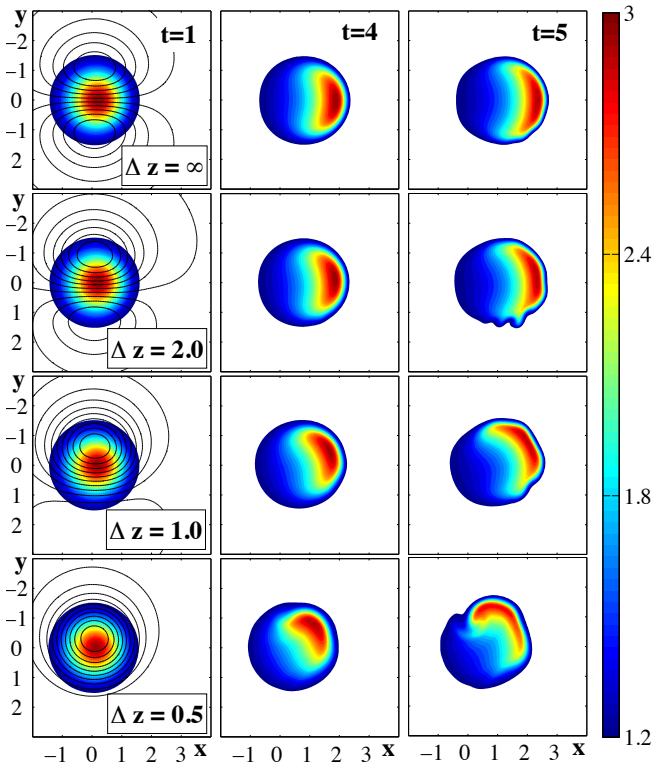

Figure 2.15: Comparison of medium blob ($\Delta = 1$) evolution for varying initial parallel density profiles. The 2D contours are taken at $z = 0$. The solid contour lines shown in the first time slices represent the 2D potential structure.

the effects of parallel electron dynamics are examined in detail. The deviation of blob dynamics from that predicted by 2D theory due to the parallel electron dynamics is examined in the conventional 2D limit, $\sigma_{\parallel} >> \sigma_{sh}$, where the resistive bowing of the parallel profiles is negligible.

The dynamics of plasma blobs predicted by 2D sheath limited theory is reviewed. Although E×B advection sets the time scale for small and medium blobs, whereas small wavelength flute modes set the time scale for large blobs, both of these phenomena occur on the same relative time scale ω_g^{-1}. The only relevant nondimensional parameter governing the dynamical evolution of sheath limited plasma blobs in 2D theory is the characteristic transverse size of the blob δ with respect to the fundamental size δ_*. The different physics predicted by 2D theory for the evolution of small, medium, and large blobs is demonstrated with 2D

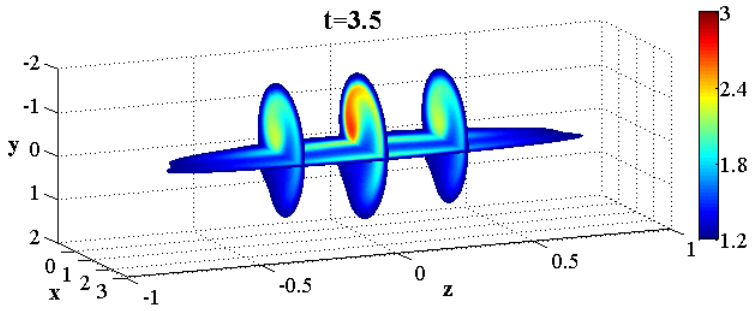

Figure 2.16: 2D density contours from 3D simulation taken at different slices along the magnetic field line corresponding to 2D density contour shown at $t = 3.5$ and $\Delta z = 0.5$ in Fig. 2.14.

simulations of the 2D governing equations using the code BOUT++.

3D simulations of seeded blobs with initially homogeneous profiles along the field line demonstrate that 2D blob theory holds well on time scales short compared to the drift wave instability, but, once the instability develops, the free energy source present in the blob density gradient is quickly depleted resulting in a much more diffuse blob with little radial convection. The effects of resistive drift waves on blob dynamics is estimated using the results from a standard local linear analysis of the 3D equations. It is argued that the linear modes from this model are a good representation of the modes that affect the more geometrically complicated, convecting plasma blobs because the convective rate is typically less than the drift wave frequency and typical blob sizes are larger than the size of the perpendicular wavelengths that correspond to the dominant unstable modes.

It is demonstrated that the sheath boundary condition does not enter into the dispersion relation for the finite parallel modes with $m \neq 0$ in the 2D limit where $\sigma_{\parallel} >> \sigma_{sh}$. The resulting dispersion relation is a linear combination of the standard flute mode and drift wave dispersion relations. The drift waves dominate the flute modes as long as the drift frequency is large compared to the flute mode frequency and the maximum growth rate in this limit is shown to scale with $1/\sqrt{g\delta}$. Thus, smaller blobs and blobs in systems with a smaller effective gravity force should be

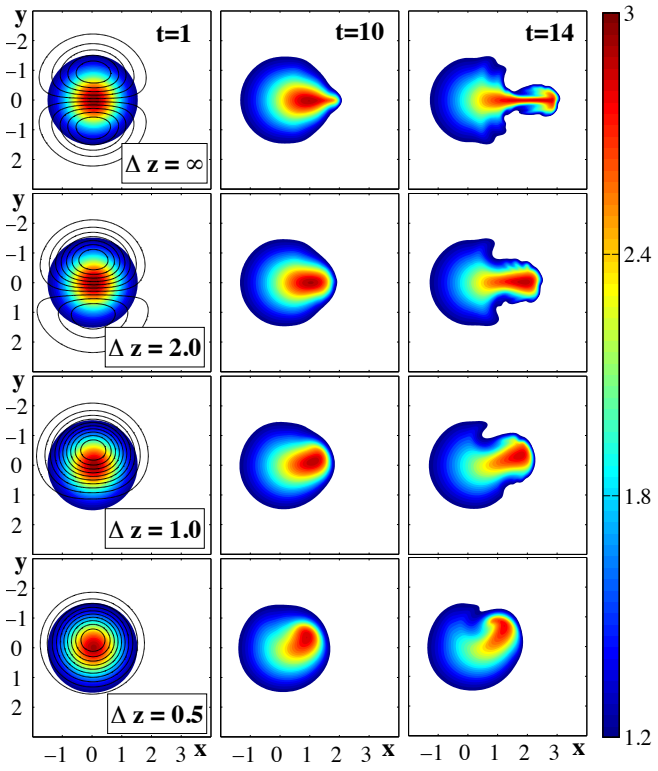

Figure 2.17: Comparison of large blob ($\Delta = 3$) evolution for varying initial parallel density profiles. The 2D contours are taken at $z = 0$. The solid contour lines shown in the first time slices represent the 2D potential structure.

more susceptible to the drift wave instability. This result is supported numerically by performing four different 3D simulations and varying the blob size and effective gravity force.

The parallel mode number corresponding to the maximum growth rate predicted by the local linear analysis is determined by $\omega_{\|} = \omega_*/(1+\chi^2)$ and seems to agree well with that found in the seeded blob simulations. It should be mentioned that in the conventional 2D limit as $\sigma \to \infty$, a system of finite length L cannot support the dominant unstable modes and 2D theory should be valid with respect to the drift wave instability. However, for most practical values of σ, the dominant modes can be supported.

The perpendicular and parallel wavelengths corresponding to the dominant unstable modes are identified for a $\Delta = 1$ blob using two different parameter sets - a

set that is characteristic of current tokamaks and a set that may be characteristic of future tokamaks. The wavelengths corresponding to the dominant unstable modes agree qualitatively well with that predicted by the local linear analysis. Exponential growth is found to occur during the time range where the dominant unstable modes become noticeable in the simulations. In agreement with the local linear analysis, the future-like blob dissipates at a relatively earlier time than the current-like blob does. However, even though the onset of the dominant unstable mode for the future-like blob occurs at a relatively earlier time than for the current-like blob, the actual growth rate is larger for the current-like blob. I argue that this is because the current-like blob propagates further before the dominant unstable mode sets in and, since the radial density gradient of the blob steepens more and more as the blob propagates radially outward [23], the actual density gradient is much larger than that used in the local linear analysis. A more modest linear mode does seem to set in for the current-like blob at around the same normalized time as the dominant mode sets in for the future-like blob, but this mode is not strong enough to dissipate the blob before a more dominant mode sets in at a later time. A more detailed analysis of the modes seen in these simulations with those predicted by a global solution employing the full background density profile when the blob goes unstable is in the works and will be discussed in a future paper.

The results presented in this paper on the effect of drift waves on blob dynamics are only expected to be qualitatively accurate due to the limitations of the simplified model used. Namely, the neglect of parallel electron kinetics, parallel electron heat flow, and finite ion temperature. The use of parallel Ohm's law is only valid in the collisional fluid limit where $\lambda_e k_\parallel < 1$ and this parameter is marginal for most tokamak edge parameters. Also, the isothermal electron assumption is never actually a quantitatively good assumption for linear drift waves [36] in a collisional plasma. Furthermore, although the ions are typically much colder than the electrons in the edge of most small scale experimental devices, it can be comparable to or even larger than T_e in the edge region of large scale tokamaks [17]. All of these limitations should be considered when interpreting the results from this work and suggest that parallel electron heat flow, parallel electron kinetics,

and finite ion-larmor radius effects could be important.

Blobs seeded with a varying parallel profile results in the plasma having a Boltzmann-like relation along the field line. This Boltzmann potential has a radial profile due to its dependence on the radially varying blob density and introduces a new sink of the 2D driving potential through spinning. Analogous to the effects of spinning that result from sheath connected plasma blobs with a radially varying temperature profile discussed in [21], Boltzmann spinning reduces the blobs radial velocity, keeps the blob more coherent, and induces some poloidal convection. However, these effects are only descriptive of the blob dynamics during the early stages of the blob evolution before the drift wave instability sets in, which eventually dissipates the blob. The contrasts are that spinning due to a varying parallel density profile has a parallel variation and can occur even if the blob is not sheath connected. The sheared rotation associated with this parallel variation of spinning can also be a source of instability for plasma blobs [38]. However, this instability is electromagnetic in nature and thus cannot be captured by the electrostatic equations considered in this paper. Electromagnetic effects should be a topic for future research.

It is argued from the conventional sink-source relation of the 2D potential that the relative importance of spinning on convecting blobs can be determined by comparing the conventional 2D potential with the Boltzmann potential that arises due to the parallel density profile. This claim is supported by performing a series of 3D seeded blob simulations and varying the initial density profiles. Quantifying the 3D effects of spinning on large blobs is different then that for small and medium blobs because the 2D dynamics of large blobs is that they break apart via small wavelength flute modes on time scales short compared to their advective time. The results of 3D seeded blob simulations with varying profiles for a large blob are presented. It is found that spinning stabilizes a small wavelength flute mode [37], but a larger wavelength finger still develops.

The work presented in this chapter is a reprint of the material as it appears in *Effects of parallel electron dynamics on plasma blob transport* in Physics of

Plasmas 19, 082312 by J. Angus, M. Umansky, and S. Krasheninnikov, 2012. The dissertation author was the primary investigator and author of this paper.

Chapter 3

Drift Wave Dispersion Relation for Arbitrarily Collisional Plasma

Drift waves are a class of electrostatic modes regularly seen in magnetically confined plasmas that play a vital role in cross field plasma transport [39]. The modes are often linearly unstable due to the "free energy" source contained in the plasma pressure gradient and there are many different processes that can act as the mechanism for the onset of the instability [35,39]; such as a finite resistivity via electron-ion collisions, resonant wave-particle interactions, a finite current density along the magnetic field line, etc. Drift waves that are driven unstable by the first two methods are considered in this Chapter. The physics of resistive drift waves driven by electron-ion collisions and collisionless drift waves driven by resonant wave-particle interactions is well documented and understood. The physics of both is explained thoroughly in [35, 39] and the references therein.

Resistive drift waves and collisionless drift waves occur in completely different system parameter regimes and are therefore governed by different equations. The plasma is governed by the collisional fluid equations when both $\nu >> \omega$ and $\lambda_e k_\parallel << 1$, where ν is the collision frequency, λ_e is the electron mean free path, and the characteristic time scale and spatial scale of interest are respectively ω^{-1} and $k_\parallel^{-1}$. The collisionless kinetic equation describes the system when $\nu << \omega$.

However, in the intermediate regime, where $\nu \sim \omega$ and $\lambda_e k_\parallel \sim 1$, neither the collisional fluid equations nor the collisionless kinetic equation are considered valid.

To address the issue of linear drift waves in these intermediate regimes, a generalized linear dispersion relation for drift waves that is valid for arbitrary values of $\lambda_e k_\parallel$ and ν/ω is obtained. This is accomplished by treating the electrons using the drift-kinetic equation to retain wave-particle interactions and using a BGK-like collision operator [40] to represents the collisional exchange of momentum with the ions. Moreover, the electrons are typically considered isothermal in the collisional treatment, which is only valid when ω is less than the parallel electron diffusion rate $\omega_\parallel$. The kinetic treatment of electrons insures that finite parallel electron heat flow is also retained in the analysis. The effect that finite ion temperature has on the dispersion relation is analyzed by treating the ions in the traditional way using the full collisionless Boltzmann equation.

3.1 Highly Collisional Electrons

Drift waves are a quasi-neutral phenomenon where the parallel physics along the field line dominates the electron dynamics and the cross field physics dominates the ion dynamics. The linear dispersion relation is found by separately solving for the electron and ion density perturbations, $\tilde{n}_e$ and $\tilde{n}_i$, in terms of the potential perturbation $\tilde{\phi}$ and then equating them. Solving for $\tilde{n}_e$ using a kinetic equation implicitly implies that temperature perturbations are retained in the analysis. However, the conventional method for obtaining $\tilde{n}_e$ from the collisional fluid equations [35] is done by assuming that the electrons are isothermal. In order to have an appropriate expression for $\tilde{n}_e$ from a fluid theory to compare with $\tilde{n}_e$ in the collisional limit from a kinetic theory that includes collisions, the electron temperature perturbations must be retained in the linear analysis of the fluid equations. This requires retaining the electron heat equation and thus the full set of electron Braginskii equations [41] needs to be considered. The full set of Braginskii equations for electrons in a singly charged ($Z = 1$) collisional plasma

are

$$\frac{\partial n_e}{\partial t} + \nabla \cdot (n_e \mathbf{V}_e) = 0, \tag{3.1}$$

$$n_e m_e \frac{d\mathbf{V}_e}{dt} = -\nabla \cdot \pi_e - \nabla P_e + e n_e \left(\nabla \phi - \frac{\mathbf{V}_e}{c} \times \mathbf{B} \right) + \mathbf{R}_e, \tag{3.2}$$

$$n_e \frac{3}{2} \frac{dT_e}{dt} + P_e \nabla \cdot \mathbf{V}_e = -\nabla \cdot \mathbf{q}_e - \pi_e : \nabla \mathbf{V}_e + Q_e, \tag{3.3}$$

where $d/dt = \partial/\partial t + \mathbf{V}_e \cdot \nabla$, $P_e = n_e T_e$, and all other terms such as the stress tensor π_e, the electron-ion momentum transfer $\mathbf{R}_e$, the electron heat flux $\mathbf{q}_e$, and the electron-ion heat transfer Q_e are defined conventionally as presented in [41].

Consider a strongly magnetized plasma in a Cartesian geometry with a uniform magnetic field $\mathbf{B} = B\hat{\mathbf{z}}$ in the z-direction. The ions for now are assumed to be cold. A local linear analysis of Eqs (3.1)-(3.3) relevant to the study of resistive drift waves is performed by assuming a background with no potential, no mean parallel velocity, homogeneous electron temperature, and density that is homogeneous along y and z but has a gradient in the x-direction $\partial \ln n_0/\partial x = -1/\delta$. Perturbations of the form $\exp\left[-i\omega t + ik_\perp y + ik_\parallel z\right]$ are assumed for the density, potential, velocity, and temperature. The ordering of time scales for a local analysis of collisional drift waves is $\omega << 1/\tau_e << \Omega_e$, and the order of space scales is $\lambda_e k_\parallel << 1$, $\rho_e << k_\perp^{-1} << \delta$, and $k_\parallel << k_\perp$. Here $\Omega_e = eB/(m_e c)$ is the electron gyro-frequency, $\rho_e = v_e/\Omega_e$ is the electron gyro-radius, $v_e = \sqrt{T_e/m_e}$ is the electron thermal velocity, $\tau_e = 3\sqrt{m}T_e^{3/2}/(4\sqrt{2\pi}e^4 n \ln\Lambda)$ is the electron collision time with $\ln\Lambda \approx 10$, and $\lambda_e = \tau_e v_e/0.51$ is the electron mean free path. The heat transfer between electrons and ions may also be neglected since it occurs on a time scale longer than the momentum transfer by the factor of M_i/m_e. The reduced set of equations relevant to the study of linear drift waves in the limits and assumptions

mentioned above are

$$\frac{\partial n_e}{\partial t} + \mathbf{V}_{\mathrm{E}} \cdot \nabla n_e = -\nabla_{\parallel} \left(n_e V_{\parallel} \right), \tag{3.4}$$

$$\frac{0.51 m_e n_e}{\tau_e} V_{\parallel} = e n_e \nabla_{\parallel} \phi - \nabla_{\parallel} P_e - 0.71 n_e \nabla_{\parallel} T_e, \tag{3.5}$$

$$\frac{3}{2} \frac{\partial T_e}{\partial t} + T_e \nabla_{\parallel} V_{\parallel} = \frac{-1}{n_e} \nabla_{\parallel} \left(0.71 n_e T_e V_{\parallel} - \kappa_{\parallel}^e \nabla_{\parallel} T_e \right), \tag{3.6}$$

where $\kappa_{\parallel}^e = 3.16 n_e T_e \tau_e / m_e$, $V_{\parallel} = \mathbf{V}_e \cdot \hat{\mathbf{b}}$, and $\mathbf{V}_{\mathrm{E}} = c\hat{\mathbf{b}} \times \nabla\phi / B$ is the E×B drift velocity.

Notice that the diamagnetic component of the electron velocity normal to the magnetic field does not enter into Eqs (3.4)-(3.6). This is because a homogeneous magnetic field is assumed in which case the diamagnetic velocity plays no role in the density evolution, has its contribution to the advection of momentum exactly cancelled by the corresponding component of the collisionless diamagnetic contribution to the stress tensor, and its contribution to the left hand side of the heat equation is exactly balanced by the diamagnetic heat flux.

After some algebra, the electron density perturbation $\tilde{n}_e$ is found in terms of the potential perturbation $\tilde{\phi}$ to be

$$\frac{\tilde{n}_e}{n_0} = \left[\frac{\left(\omega_* + i\omega_{\parallel} \right) \left(\frac{3}{2}\omega + i\kappa\omega_{\parallel} \right) + \beta i \omega_* \omega_{\parallel}}{\left(\omega + i\omega_{\parallel} \right) \left(\frac{3}{2}\omega + i\kappa\omega_{\parallel} \right) + \beta i \omega \omega_{\parallel}} \right] \frac{e\tilde{\phi}}{T_e}, \tag{3.7}$$

where $\omega_* = c_s \rho_s k_{\perp} / \delta$ is the drift frequency, $c_s = \sqrt{T_e / M_i}$ is the cold ion sound speed, $\rho_s = c_s / \Omega_i$, $\omega_{\parallel} = v_e^2 k_{\parallel}^2 / \nu$ is the characteristic rate for an electron to diffuse a parallel wavelength, $\nu = 0.51/\tau_e$ is the collision frequency, $\kappa = 1.61$, and $\beta = (1.71)^2$. κ physical comes from the diffusive heat flux and rest of the electron temperature fluctuations enter the dispersion relation through the terms proportional to β; if the contributions from the thermal force are neglected then $\beta = 1$ and if temperature perturbations are neglected all together then $\beta = 0$. In the latter case, Eq. (3.7) reduces to what would be found by *a priori* setting $\tilde{T} = 0$ [35].

The isothermal treatment of electrons in a collisional plasma is typically considered valid when the collisionally diffusive heat flux rate $\omega_{\parallel}$ is much faster than

the phenomenon under consideration ω. However, due to the fact that the velocity perturbations in a collisional plasma are set by collisions rather than by inertia, the "effective" adiabatic response to the heat equation occurs on the same time scale as the heat flux and thus the temperature fluctuations are always the same order as the density perturbations independent of the heat flux rate. A detailed comparison of the dispersion relations found when ignoring electron temperature perturbations and that found by retaining $\tilde{T}$ will be given later in the chapter.

3.2 Arbitrarily Collisional Electrons

To explore the effects of finite electron mean free path ($\lambda_e k_\parallel \sim 1$) on linear drift waves, consider the electrons to be governed by the following drift-kinetic equation with a BGK-like collision operator [40]:

$$\frac{\partial f}{\partial t} + \mathbf{V}_\mathrm{E} \cdot \nabla f + v_\parallel \nabla_\parallel f + \frac{e}{m_e} \nabla_\parallel \phi \frac{\partial f}{\partial v_\parallel} = -\nu \left(f - f_\mathrm{M} \right), \tag{3.8}$$

where f is the gyro-phase independent electron distribution function and f_M is the Maxwellian distribution function defined as

$$f_\mathrm{M} = n_e \exp\left[-v^2/(2v_e^2) \right] / \left(\sqrt{2\pi v_e^2} \right)^3. \tag{3.9}$$

All other parameters are defined the same as before. The mean parallel velocity $V_\parallel = \int v_\parallel f d\mathbf{v}/n_e$ is ignored in the Maxwellian used in the collision operator because this operator is meant to represent the loss of electron momentum due to a difference in the electron and ion mean velocities.

The electron-electron energy exchange rate is on the same order as the electron-ion momentum exchange rate and the collision operator used in Eq. (3.8) can therefore be considered to represent both the collisional loss of electron momentum to the ions as well as the collisional relaxation of the electrons with themselves. Also, since the thermal energy exchange of electrons with ions occurs on a time scale that is larger than ν by a factor of $M_i/m_e >> 1$, it is a valid assumption to ignore this in the collision operator and thus our collision operator

has the desired properties of conserving density $n_e = \int f d\mathbf{v}$ and thermal energy $\int \frac{m_e}{2}|\mathbf{v} - U_\parallel \hat{\mathbf{b}}|^2 f d\mathbf{v} = \frac{3}{2} n_e m_e v_e^2$.

Assume the same geometry, background, and perturbations used in the fluid analysis above to linearize Eq. (3.8). The resultant perturbed distribution function is

$$\tilde{f} = \frac{\left(k_\parallel v_\parallel - \omega_*\right) \frac{e\tilde{\phi}}{T_e} f_{M_0} - i\nu \tilde{f}_M}{k_\parallel v_\parallel - (\omega + i\nu)}, \tag{3.10}$$

where f_{M_0} is the background Maxwellian, and $\tilde{f}_M$ is the linearized Maxwellian defined as

$$\tilde{f}_M = \left(\frac{\tilde{n}_e}{n_0} + \frac{1}{2}\left(\frac{v^2}{v_e^2} - 3\right)\frac{\tilde{T}}{T_e} \right) f_{M_0}. \tag{3.11}$$

Similar linearized collision operators have been considered before in the study of rarefied gas dynamics [42,43]. One can verify that the linearized collision operator does indeed conserve density since $\int \tilde{f}_M d\mathbf{v} = \tilde{n}_e$ and, to first order in perturbation parameters, conserves thermal energy density since $\int \frac{m_e}{2}|\mathbf{v} - \tilde{U}_\parallel \hat{\mathbf{b}}|^2 \tilde{f}_M d\mathbf{v} \approx \int \frac{m_e}{2} v^2 \tilde{f}_M d\mathbf{v} = \frac{3}{2} n_0 m_e v_e^2 \left(\frac{\tilde{n}_e}{n_0} + \frac{\tilde{T}}{T_e}\right)$.

The electron density perturbation is found in terms of the potential perturbation by taking the zeroth and second velocity moments of Eq. (3.10) and performing some algebraic manipulations to remove the temperature perturbations. The result (see Appendix B) is

$$\frac{\tilde{n}_e}{n_0} = \eta \frac{e\tilde{\phi}}{T_e} \tag{3.12}$$

with

$$\eta \equiv \frac{\left(1 + \left(\alpha - \frac{\omega_*}{\sqrt{2}v_e k_\parallel}\right) Z\right)\left(\frac{3}{2} + \frac{i\nu Z}{\sqrt{2}v_e k_\parallel}\right) + \frac{i\nu}{\sqrt{2}v_e k_\parallel}\left(\frac{\omega_* \alpha}{\sqrt{2}v_e k_\parallel} - \frac{1}{2}\right)\left(\alpha + \left(\alpha^2 - \frac{1}{2}\right) Z\right)}{\left(1 + \left(\alpha - \frac{\omega}{\sqrt{2}v_e k_\parallel}\right) Z\right)\left(\frac{3}{2} + \frac{i\nu Z}{\sqrt{2}v_e k_\parallel}\right) + \frac{i\nu}{\sqrt{2}v_e k_\parallel}\left(\frac{\omega \alpha}{\sqrt{2}v_e k_\parallel} - \frac{1}{2}\right)\left(\alpha + \left(\alpha^2 - \frac{1}{2}\right) Z\right)},$$

where $Z = Z(\alpha) = \frac{1}{\sqrt{\pi}} \int_{-\infty}^{\infty} \exp(-x^2)/(x - \alpha) dx$ is the plasma dispersion function with $\alpha = (\omega + i\nu)/(\sqrt{2} v_e k_\parallel)$.

For $\nu = 0$, Eq. (3.13) directly reduces to

$$\frac{\tilde{n}_e}{n_0} = \left[1 + \left(\frac{\omega - \omega_*}{\sqrt{2}v_e k_\parallel}\right) Z(\alpha)\right] \frac{e\tilde{\phi}}{T_e}, \tag{3.13}$$

which is exactly the equation for $\tilde{n}_e/n_0$ for a collisionless plasma [35]. The leading order contribution to $Z(\alpha)$ in the collisionless isothermal limit ($\omega/k_\parallel << v_e$) comes from the Landau pole $Z(|\alpha| << 1) = i\sqrt{\pi}$ and Eq. 3.13 reduces to that used to analyze collisionless drift waves in [35].

The collisional fluid limit is valid when both $\nu/(\sqrt{2}v_e k_\parallel) >> 1$ and $\nu >> \omega$ are satisfied. The plasma dispersion function in this limit may be expressed as an infinite sum: $Z(|\alpha| > 1) = \frac{-1}{\alpha}\sum_{n=0}^{\infty} C_n \left(\frac{1}{\alpha}\right)^{2n}$, where $C_0 = 1$ and $C_n = C_{n-1}(n - 1/2)$. Without making any other assumptions on the ordering between ω and $\omega_\parallel$ and retaining all terms up to those that scale with $1/\alpha^2$, Eq. (3.13) reduces to

$$\frac{\tilde{n}_e}{n_0} = \left[\frac{\left(\omega_* + i\omega_\parallel\right)\left(\frac{3}{2}\omega + i\frac{5}{2}\omega_\parallel\right) + i\omega_*\omega_\parallel}{\left(\omega + i\omega_\parallel\right)\left(\frac{3}{2}\omega + i\frac{5}{2}\omega_\parallel\right) + i\omega\omega_\parallel}\right]\frac{e\tilde{\phi}}{T_e}. \tag{3.14}$$

Note that with the exception of having a coefficient of 5/2 in front of the term that arises due to the diffusive heat flux rather than the factor of 1.61 found from the Braginskii equations, that this expression is equivalent to Eq. (3.7) if the contributions from the thermal force in Eq. (3.7) are also neglected. These differences can be expected since a BGK collision operator is used which cannot capture the thermal force and will yield a different heat flux coefficient than that found from the Braginskii equations where the full linearized Fokker-Plank collision operator is considered.

3.3 Linear Dispersion Relation

The ion dynamics, in contrast to the electrons, are dominated by the cross field physics because of the large electron-ion mass ratio. The parallel ion dynamics occurs on the time scale of sound waves and may be neglected as long as $\sqrt{(T_e + 5T_i/3)/M_i} << \omega/k_\parallel$. Furthermore, wave particle resonances may be ignored if the ion thermal velocity $v_i = \sqrt{T_i/M_i}$ is small compared to $\omega/k_\parallel$. On the other hand, the large ion mass complicates the perpendicular dynamics when considering finite T_i because the characteristic ion gyro-radius $\rho_i = v_i/\Omega_i$ can become comparable to the perpendicular wavelength in which case the drift-kinetic equa-

tion cannot be used. For these reason, parallel dynamics can be neglected, but the ion density perturbation must be found from the full Vlasov equation rather than the simplified drift-kinetic equation. The ion density perturbation for $\omega << \Omega_i$ and $v_i << \omega/k_\parallel$ can be shown to be [35]

$$\frac{\tilde{n}_i}{n_0} = \left[\frac{\omega_*}{\omega}\mathrm{e}^{-\Lambda_i} I_0\left(\Lambda_i\right) - \frac{T_e}{T_i}\left(1 - \mathrm{e}^{-\Lambda_i} I_0\left(\Lambda_i\right)\right)\right]\frac{e\tilde{\phi}}{T_e}, \tag{3.15}$$

where $\Lambda_i = k_\perp^2 \rho_i^2$ and I_0 is the modified Bessel function of the first kind. For $k_\perp \rho_i << 1$, the ion density perturbation reduces

$$\frac{\tilde{n}_i}{n_0} = \left[\frac{\omega_*}{\omega}\left(1 - \Lambda_i\right) - k_\perp^2 \rho_s^2\left(1 - \frac{3}{4}\Lambda_i\right)\right]\frac{e\tilde{\phi}}{T_e}. \tag{3.16}$$

The expression for $\tilde{n}_i$ from cold ion theory [35], where the only contributions to $\tilde{n}_i$ are from the E×B drift velocity and the ion polarization current, is found when $\Lambda_i = 0$.

The dispersion relation for drift waves is found by equating $\tilde{n}_e$ and $\tilde{n}_i$ under the assumption of quasinuetrality. Similar to the collisionless kinetic theory, it can be shown from equating Eq. (3.13) and (3.15) that as $k_\parallel \to \infty$ the real part of the frequency ω_R approaches [35]

$$\omega_R\left(k_\parallel \to \infty\right) = \omega_*\left[\frac{\mathrm{e}^{-\Lambda_i} I_0(\Lambda_i)}{1 + \frac{T_e}{T_i}\left[1 - \mathrm{e}^{-\Lambda_i} I_0(\Lambda_i)\right]}\right]. \tag{3.17}$$

This gives $\omega_R = \omega_*/(1 + \rho_s^2 k_\perp^2)$ in the limit of small Λ_i. The maximum growth rates for $\Lambda_i << 1$ in both the collisional fluid and collisionless kinetic solutions can be shown to occur when $\rho_s k_\perp \sim 1$ [35, 44]. For the convenience of having the normalized real frequency asymptote to unity at large $k_\parallel$ when $\Lambda_i << 1$ and $\rho_s k_\perp = 1$, the following normalization is adopted: $\hat{k}_\perp = \rho_s k_\perp$, $\hat{k}_\parallel = 2\delta\sqrt{2} v_e k_\parallel / c_s$, $\hat{\omega} = 2\delta\omega/c_s$, and $\hat{\nu} = 2\delta\nu/c_s$.

In terms of these dimensionless parameters, the plasma is marginally collisional when $\hat{\nu} \approx \hat{\omega} \approx \hat{k}_\parallel$ and collisional when $\hat{\nu} >> \hat{\omega}$ and $\hat{\nu} >> \hat{k}_\parallel$. The solution of the dispersion relation for $\Lambda_i = 0$ and $\hat{k}_\perp = 1$ is compared with the collisionless (using Eq. (3.13) for $\tilde{n}_e$) and fluid solutions (using Eq. (3.7) for $\tilde{n}_e$ with $\beta = 1$) in

Figs 1-2 for varying values of $\hat{\nu}$ in order to demonstrate how the dominant unstable modes transition from being driven by wave-particle resonances to being driven by collisions.

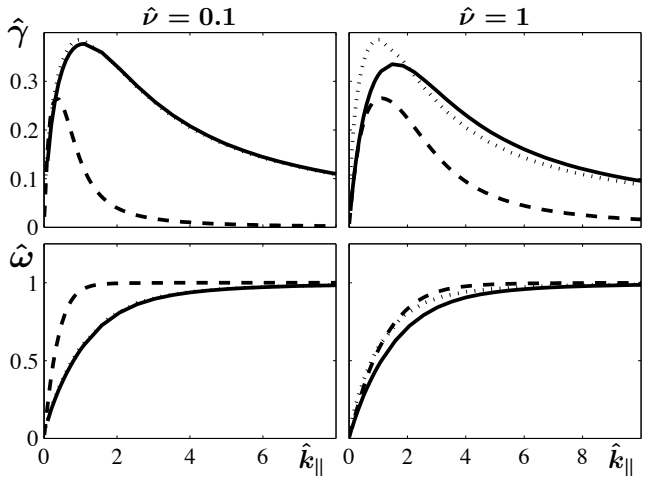

Figure 3.1: Normalized drift wave growth rate (top) and normalized frequency (bottom) versus normalized parallel wavenumber for $T_i/T_e = 0$, $\hat{k}_\perp = 1$, $\hat{\nu} = 0.1$ (left), and $\hat{\nu} = 1$ (right). The – line is the kinetic solution, the - - curve is the fluid solution without the thermal force contribution, and the ·· curve is the collisionless solution.

The solution for $\hat{\nu} = 0.1$ shown in Fig. 1 matches well with the known collisionless dispersion relation. Even for $\hat{\nu} = 1$ the Landau pole is seen to be the largest contribution to the solution for large $\hat{k}_{\|}$. The transition from the collisionless solution to the collisional solution found by neglecting the thermal force contributions to the collisional fluid dispersion relation is shown in Fig. 2. Very good agreement between the two solutions is seen for $\hat{\nu} = 100$. The small differences between the two solutions in the collisional limit are only due to the different coefficient for the heat fluxes that are found from the Braginskii equations and from using a simplified BGK collision operator.

The dispersion relation from our kinetic solution in the collisional limit (using Eq. (3.14) for $\tilde{n}_e$) is compared with the full collisional fluid solution (using Eq. (3.7) for $\tilde{n}_e$ with $\beta = 1.71^2$) in Fig. 3 to show how much the thermal force changes the dispersion relation. The conventional isothermal solution (using Eq. (3.7) for $\tilde{n}_e$ with $\beta = 0$) is also shown to demonstrate the full effect of temperature

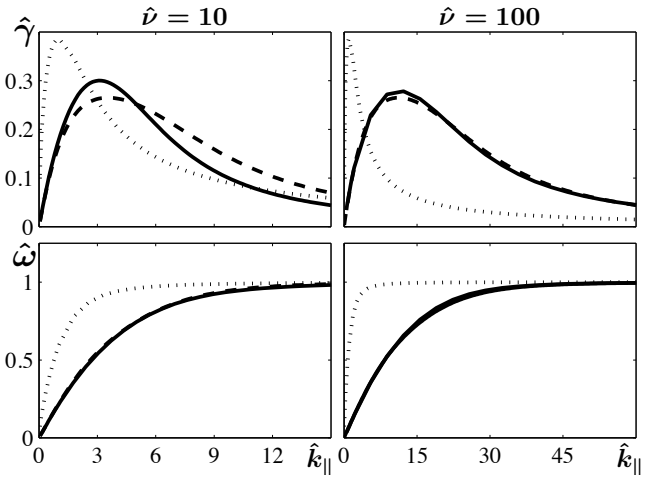

Figure 3.2: Normalized drift wave growth rate (top) and normalized frequency (bottom) versus normalized parallel wavenumber for $T_i/T_e = 0$, $\chi = 1$, $\hat{\nu} = 10$ (left), and $\hat{\nu} = 100$ (right). The – line is the kinetic solution, the - - curve is the fluid solution without the thermal force contribution, and the $\cdot\cdot$ curve is the collisionless solution.

fluctuations on the dispersion relation.

Although the dispersion relation found from considering $\tilde{T} = 0$ was shown in Section II to be quantitatively different than that found from retaining $\tilde{T}$ in the analysis, from Fig. 3 it appears that the dispersion relations qualitatively agree very well. The largest contribution to the difference between the isothermal solution and the full solution seems to be due to the thermal force.

3.4 Finite T_i Effects

The maximum growth rate as a function of T_i/T_e from the general solution is shown in Fig. 3a for varying values of $\hat{\nu}$ to demonstrate how the drift wave instability is modified by finite ion temperature. The maximum growth rates are about the same when $T_i \approx T_e$ as they are for $T_i << T_e$, but they decrease by about a factor of two for $T_i = 10T_e$. The corresponding perpendicular wavenumber, parallel wavenumber, and real frequency are also shown. Notice that the maximum growth rate as a function of $k_\perp$ shifts from peaking around $\rho_s k_\perp \sim 1$ for $T_i << T_e$

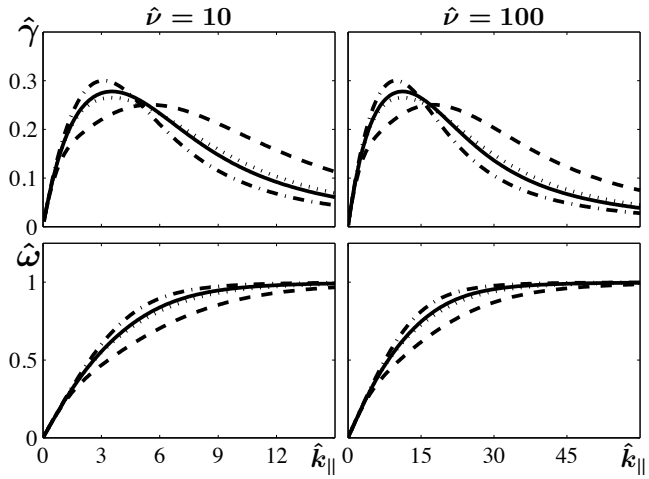

Figure 3.3: Normalized drift wave growth rate (top) and normalized frequency (bottom) versus normalized parallel wavenumber for $T_i/T_e = 0$, $\hat{k}_\perp = 1$, $\hat{\nu} = 10$ (left), and $\hat{\nu} = 100$ (right). The – line is the kinetic solution in the collisional limit, the $\cdot - \cdot$ curve is the conventional isothermal fluid solution, the - - curve is the full fluid solution, and the $\cdot\cdot$ curve is the fluid solution without the thermal force contributions.

to peaking around $\rho_i k_\perp \sim 1$ when $T_i \gtrsim T_e$. The real frequency corresponding to the maximum growth rate decreases with increasing T_i/T_e, as is expected from Eq. (3.17), but, similar to the maximum growth rate, is relatively independent of collisionality. The parallel wavenumber where the maximum growth rate occurs only slightly decreases with increased ion temperature.

3.5 Conclusion

In summary, a generalized linear dispersion relation for drift waves valid for arbitrary values of electron-ion collision frequency and electron mean free path is obtained by treating the electrons using the drift-kinetic equation with a BGK-like collision operator to represent both the collisional loss of momentum to ions and thermal relaxation with themselves. The solution matches the well-known collisionless solution exactly when the collision frequency is zero. The solution also matches the collisional fluid solution quite well in the highly collisional limit

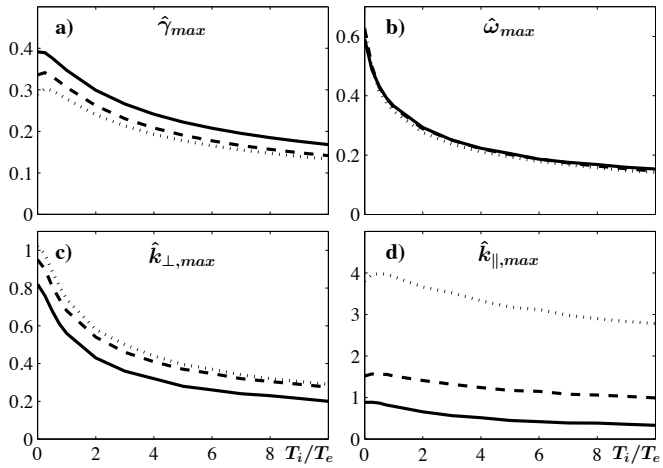

Figure 3.4: Maximum growth rate a) and corresponding frequency b), perpendicular wavenumber c), and parallel wavenumber d) versus temperature ratio T_i/T_e for varying values of collision frequency $\hat{\nu}$. The – line is for $\hat{\nu} = 0$, the - - line is for $\hat{\nu} = 1$, and the $\cdot\cdot$ line is for $\hat{\nu} = 10$.

if one neglects the thermal force contributions to the dispersion relation from fluid theory which cannot be captured with the simple BGK collision operator used in our kinetic analysis.

The conventional collisionally isothermal assumption used to neglect $\tilde{T}$ with respect to $\tilde{n}_e$ in the electron analysis is shown to not actually be a valid assumption in a collisional plasma where the "effective" adiabatic response is set by collisions rather than by inertia in which case the contributions to the heat equation from the compression of the plasma and the heat flux are always on the same order. However, the dispersion relation found from treating the electrons as isothermal in fluid theory is shown to be qualitatively similar to the full solution found by retaining the electron temperature fluctuations in the linearization of the Braginskii equations. The largest contribution to the difference is the effect of the thermal force in the Braginkii equations and results in a slightly decreased maximum growth rate that occurs at a slightly higher parallel wavenumber.

Using the same edge parameters that were used in Ch. 2 typical for current tokamaks ($T_e = 20$eV, and $n_B = 10^{13}\text{cm}^{-3}$) and future tokamaks ($T_e = 50$eV, and

$n_B = 3 \times 10^{13}\text{cm}^{-3}$) one obtains $0.1 \lesssim \hat{\nu} \lesssim 1.0$ for typical blob sizes $0.1 \lesssim \delta \lesssim 1.0$. It can be concluded from Fig. 1 that the maximum growth rates from fluid theory in this range of $\hat{\nu}$ occurs where the system is marginally collisional ($\hat{\omega} \approx \hat{\nu} \approx \hat{k}_{\|}$), but the the full solution demonstrates that the actual dominant unstable modes for this range of $\hat{\nu}$ are mostly driven by collisionless effects. However, since the fluid equations still yield a maximum growth rate comparable to that from collisionless theory, the fluid equations are sufficient enough to determine that the density gradients that drive the blob will be depleted on time scales short compared to blobs convective time scale. From a nonlinear point of view though, the fact that the maximum growth rate from the fluid equations occurs at a lower mode number and misses the numerous comparable modes at higher $\hat{k}_{\|}$ may mean that the fluid equations will not accurately depict the nonlinear behavior of drift waves in systems where $\hat{\nu} \lesssim 1$.

The ability of the fluid equations to capture the correct maximum linear growth rate is also dependent on the assumption that $T_i < T_e$ which is typically not a good assumption in the open field line scrape off layer of large scale tokamaks. It was shown that the maximum growth rate doesn't change appreciably when T_i and T_e are comparable, but does decrease by about a factor of two when the T_i is an order of magnitude larger than T_e. Moreover, the convective rate of blobs scales with the square root of the total temperature ($\sqrt{T_e + T_i}$) [17] and will therefore increase as T_i becomes comparable to and larger than T_e. Thus, when $T_i \gtrsim T_e$, the disparity between the blob convective rate and the maximum drift wave growth rate in systems will not be as large as Eq. 2.23 gives. However, baring the extreme case where $T_i \approx 10T_e$, the disparity in the time scales is still enough to suggest that drift waves could affect blobs in the outer midplane of large scale tokamaks.

However, since the growth rate is exponential, one could still expect drift waves to affect plasma blobs in the outer midplane of large scale tokamaks. However, since the maximum growth rates occur around $k_\perp \rho_i$ order unity when $T_i >> T_e$, finite ion gyro-radius effects could be import for accurate modeling of plasma blobs in the outer midplane of tokamaks which cannot be captured by fluid theo-

ries.

To conclude I wish to make some general comments about linear drift waves. Collisionless drift waves are driven unstable by wave-particle interactions and have maximum growth rates when the phase velocity $\omega/k_\parallel$ is on the order of the electron thermal velocity v_e. On the other hand, resistive drift waves are driven unstable by electron-ion collisions and the maximum growth rates occur when ω is on the order of the parallel diffusion rate $\omega_\parallel$. In either case, the wave frequency ω is on the order of the fundamental drift frequency, given in Eq. 3.17, which for cold ions is on the order of ω_*. The growth rate is linked with this fundamental frequency of drift waves and, even though the mechanism by which the waves are driven unstable is different in the collisional and collisionless cases, it is not surprising that the maximum growth rates are comparable. An example of this link between the maximum growth rate and frequency can be seen in Fig. 3.4 a) and b) where the maximum growth rate and real frequency where the maximum growth rate occurs both decay in similar ways with increasing ion temperature. This suggests that linear drift waves driven unstable by other mechanisms not discussed in this chapter could be expected to also have similar growth rates to those discussed in this chapter as long as the fundamental frequency remains more or less the same. The main role of the destabilizing mechanism seems to be in determining the parallel wavenumber $k_\parallel$ at which the maximum growth rate will occur.

The work presented in this chapter is a reprint of the material as it appears in *Drift wave dispersion relation for arbitrarily collisional plasmas* in Physics of Plasmas 19, 052504 by J. Angus and S. Krasheninnikov, 2012. The dissertation author was the primary investigator and author of this paper.

Chapter 4

Model Drag-Diffusion Collision Operator for Kinetic Codes

Each particle in a plasma is continuously experiencing electrostatic interactions (collisions) with all the other particles in the plasma. These collisions change each particles instantaneous speed and direction. In ideal plasmas, due to the relatively large mean particle energy, the dominant contribution to the change of a particles velocity vector comes from a collective effect of many weak (small angle scattering) interactions. The evolution of the distribution function of species α due to discrete small angle scattering collisions is governed by the standard Fokker-Planck Equation [45, 46]:

$$\frac{\partial f_\alpha}{\partial t}|_c = -\sum_\beta \frac{\partial}{\partial \mathbf{v}} \cdot \left[\mathbf{A}_\beta f_\alpha - \frac{1}{2} \frac{\partial}{\partial \mathbf{v}} \cdot (\mathbf{D}_\beta f_\alpha) \right], \tag{4.1}$$

where the vector $\mathbf{A}_\beta$ and the tensor $\mathbf{D}_\beta$ are respectively the dynamical friction and diffusion coefficients for species α due to collisions with species β. The sum is taken over all present species. Eq. 4.1 represents the slowing down and diffusion of particles in velocity space due to collisions. In general, these coefficients are functions of the velocity space coordinate $\mathbf{v}$ as well as the distribution function of the species β with which species α is interacting with.

The dynamical friction and diffusion coefficients for a plasma species are

$$\mathbf{A}_\beta = \Gamma_\beta \frac{\partial H_\beta}{\partial \mathbf{v}}, \quad \text{and} \quad \mathbf{D}_\beta = \Gamma_\beta \frac{\partial^2 G_\beta}{\partial \mathbf{v} \partial \mathbf{v}}, \tag{4.2}$$

where H_β and G_β are known as the Rosenbluth potentials [47] defined respectively as

$$H_\beta(\mathbf{v}) = \frac{m_\alpha}{\mu} \int_{\mathbf{v}'} \frac{f_\beta(\mathbf{v}')}{|\mathbf{v} - \mathbf{v}'|} d\mathbf{v}', \quad \text{and} \quad G_\beta(\mathbf{v}) = \int_{\mathbf{v}'} f_\beta(\mathbf{v}') |\mathbf{v} - \mathbf{v}'| \, d\mathbf{v}', \tag{4.3}$$

with $\mu = m_\alpha m_\beta / (m_\alpha + m_\beta)$ the reduced mass and the integrals are taken over all of velocity space. The velocity independent Γ_β is defined as $\Gamma_\beta \equiv 4\pi q_\alpha^2 q_\beta^2 \ln\Lambda / m_\alpha^2$ with $\ln\Lambda$ the Coulomb logarithm and all other notation is standard. The Fokker-Planck collision operator for a plasma species with the coefficients defined in Eq. 4.2 posses several physically meaningful properties [48]. First off, it conserves density, momentum, and energy. It also satisfies the H-theorem, which states that the entropy of the system must increase in time and that the steady state solution is a Maxwellian. The Maxwellian distribution is the maximum entropy state and is defined as

$$f_M = \frac{n}{\left(\sqrt{\pi} v_T\right)^3} \exp\left(-\frac{v'^2}{v_T^2}\right), \tag{4.4}$$

where n is the density, $v'^2 = |\mathbf{v} - \mathbf{U}|^2$ with mean velocity $\mathbf{U}$, and $v_T^2 = 2T/m$ is the thermal velocity with temperature T.

The full nonlinear Fokker-Planck equation for velocity space collisions in a plasma is analytically well formulated. However, due to the complex velocity space dependence of the dynamic friction and diffusion coefficients (Eq's 4.2-4.3), it is very computationally expensive to use in a numerical algorithm. Moreover, even though the analytical form of the operator exactly conserves the first three velocity space moments, retaining these conservations numerically is challenging [49–52]. The conservation of density can be captured numerically using a finite volume method, but numerical error in the calculation of the fluxes leads to unphysical numerical heating of the system and can lead to erroneous results. The error in these moments can be held to a tolerable limit using more refined grids or iterative processes, but this just amplifies the computational expense of an already numerically expensive algorithm.

The difficulties in computing the full nonlinear Fokker-Planck collision operator is often circumvented in numerical algorithms by using reduced forms of the collision operator that are easier to model numerically. These reduced models can be formulated from physically meaningful simplifications of the full operator, such as the linearized Fokker-Planck operator [52–55] and the Lorentz operator [55]. They can also be simplified "model" operators that may not correspond to any real physically justifiable simplification of the full Fokker-Planck equation, but satisfy at least some of the relevant physically properties. Some examples of "model" collision operators in a plasma are the Krook operator [40, 55, 56] and the Fokker-Planck operator for Brownian motion [57, 58]. These "model" operators are often used to study phenomena that occur on time scales much longer than the collisional time scale where the detailed relaxation of the distribution function to a Maxwellian is not important.

It is demonstrated in this Chapter how the Fokker-Planck operator for Brownian motion can be used as a "model" operator for like-like plasma species collisions in a numerical algorithm. This model relaxes the distribution function to a Maxwellian with drag and diffusion, while preserving the density, momentum, and energy. An appealing feature of this operator, that results from the simplified structure of the dynamical friction and diffusion coefficients, is that the conservation of density, momentum, and energy can be captured *exactly* numerically with relatively minimal computational effort with respect to the fully nonlinear collision operator.

4.1 Model Drag-Diffusion Collision Operator

The Fokker-Planck operator for a species described by the distribution function f undergoing Brownian motion in a moving medium with velocity $\mathbf{U} = \mathbf{U}(\mathbf{x})$ and temperature $T = T(\mathbf{x})$ is

$$\frac{\partial f}{\partial t}|_c = \nu \frac{\partial}{\partial \mathbf{v}} \cdot \left((\mathbf{v} - \mathbf{U})\, f + \frac{T}{m} \frac{\partial f}{\partial \mathbf{v}} \right), \tag{4.5}$$

where m is the species mass and $\nu = \nu(\mathbf{x})$ is the collision frequency. If f represents ions and the medium is electrons, then Eq. 4.5 describes the ion-electron collision integral in the highly collision limit where the species are close to Maxwellian [41]. An additional assumptions for this situation is that relative mean velocity between electrons and ions be small compared to the electron thermal velocity $|\mathbf{U}_e - \mathbf{U}_i| / v_T << 1$.

Eq. 4.5 can also be used as a "model" for like-like particle collision in a plasma if the density n, mean velocity $\mathbf{U}$, and temperature T are defined from the following velocity space moments of the distribution function:

$$(n,\ n\mathbf{U},\ nT) \equiv \int_{\mathbf{v}} f \left(1,\ \mathbf{v},\ \frac{mv'^2}{3}\right) d\mathbf{v}. \tag{4.6}$$

Using Eq. 4.5 with $\mathbf{U}$ and T defined in Eq. 4.6 relaxes the species to a Maxwellian while conserving density, momentum, and energy. This model operator thus satisfies all of the main macroscopic requirements of a velocity space collision operator in a plasma. It is shown below how the conservation of these quantities can be captured exactly in a numerical algorithm.

4.1.1 Finite-Volume Discretization

The finite-volume numerical method is used since the operator presented in Eq. 4.5 is in divergence form. In a finite-volume method, one solves for the cell-averaged distribution function. The idea being that the cell-averaged value reduces to the cell-centered values as the grid is refined. To make the discussion easier, a 3D3V Cartesian grid with uniform spacing h_i in the ith direction is considered. Generalization of the results to be presented to non-Cartesian systems is straight forward. The cell-average of an arbitrary function g at the location $(\mathbf{x}_i, \mathbf{v}_l) \equiv (x_i, y_j, z_k, u_l, v_m, w_n)$ is

$$\langle g \rangle_{\mathbf{x}_i, \mathbf{v}_l} \equiv \frac{1}{h_{\mathbf{v}} h_{\mathbf{x}}} \int_{\mathbf{v}_i - h_{\mathbf{v}}/2}^{\mathbf{v}_i + h_{\mathbf{v}}/2} \int_{\mathbf{x}_i - h_{\mathbf{x}}/2}^{\mathbf{x}_i + h_{\mathbf{x}}/2} g d\mathbf{x} d\mathbf{v}. \tag{4.7}$$

The finite-volume discretization of Eq. 4.5 is simplified by use of Gauss' theorem and is

$$\begin{aligned}\frac{\partial \langle f\rangle_{\mathbf{x}_i,\mathbf{v}_l}}{\partial t} &= \frac{1}{h_u}\left\langle \nu\left[(u-U^c)\,f+\frac{T^c}{m}\frac{\partial f}{\partial u}\right]_{l-1/2}^{l+1/2}\right\rangle_{\mathbf{x}_i,mn} \\ &+ \frac{1}{h_v}\left\langle \nu\left[(v-V^c)\,f+\frac{T^c}{m}\frac{\partial f}{\partial v}\right]_{m-1/2}^{m+1/2}\right\rangle_{\mathbf{x}_i,ln} \\ &+ \frac{1}{h_w}\left\langle \nu\left[(w-W^c)\,f+\frac{T^c}{m}\frac{\partial f}{\partial w}\right]_{n-1/2}^{n+1/2}\right\rangle_{\mathbf{x}_i,lm}, \end{aligned} \tag{4.8}$$

where the mean velocity $\mathbf{U}=U\hat{\mathbf{u}}+V\hat{\mathbf{v}}+W\hat{\mathbf{w}}$ and temperature T are superscripted with the letter c (for conservative) to distinguish between the mean velocity and temperature used on the RHS of Eq. 4.8 to conserve the numerical moments and the actual mean velocity and temperature interpreted from the numerical moments of $\langle f\rangle$ to be defined in the next section.

4.1.2 Numerical Conservation of Density, Momentum, and Energy

The proof of conservation the density, momentum, and energy moments of Eq. 4.5 follows from the fact that the distribution function f and its derivatives $\partial f/\partial\mathbf{v}$ are zero on the surfaces at $\mathbf{v}=\pm\infty$. In order to preserve these conservations on a finite numerical grid, numerical definitions of these moments need to first be presented. The numerical quantities to be conserved are the cell-averaged density, cell-averaged mean momentum, and cell-averaged mean energy. The cell-averaged density, mean velocity density, and pressure at real space location $\mathbf{x}_i$ on a grid with $N_\mathbf{v}\equiv(N_u,N_v,N_w)$ evenly spaced grid points in the velocity space dimension are defined as

$$\left(\langle n\rangle_{\mathbf{x}_i},\ \langle n\mathbf{U}\rangle_{\mathbf{x}_i},\ \langle nT\rangle_{\mathbf{x}_i}\right)\equiv\int_{\Omega_\mathbf{v}}\left(1,\ \mathbf{v},\ \frac{m}{3}v'^2\right)\langle f\rangle_{\mathbf{x}_i,\mathbf{v}_l}\,d\mathbf{v}, \tag{4.9}$$

where

$$\int_{\Omega_\mathbf{v}}\langle\rangle_{\mathbf{v}_l}d\mathbf{v}\equiv\sum_{n=0}^{N_w-1}\sum_{m=0}^{N_v-1}\sum_{l=0}^{N_u-1}\langle\rangle_{lmn}h_uh_vh_w$$

is the numerical integral over the finite velocity domain $\Omega_{\mathbf{v}}$. Note that these definitions of the velocity space moments reduce to the exact definitions given in Eq. 4.6 in the limit where the grid spacing goes to zero and the velocity domain extrema go to $\mathbf{v}\left(\mathbf{v}_l = -1/2\right) \to -\infty$ and $\mathbf{v}\left(\mathbf{v}_l = N_{\mathbf{v}} - 1/2\right) \to +\infty$.

The condition for the exact numerical conservation of density is obtained by taking the zeroth numerical moment of Eq. 4.8 using the same numerical integration as used in Eq. 4.9 and setting it to zero. The zeroth moment of Eq. 4.8, after some algebraic simplifications, is

$$\begin{aligned}
\frac{\partial \langle n \rangle_{\mathbf{x}_i}}{\partial t} &= \sum_{n=0}^{N_w-1} \sum_{m=0}^{N_v-1} h_v h_w \left\langle \nu \left[(u - U^c) f + \frac{T^c}{m} \frac{\partial f}{\partial u} \right]_{l=-1/2}^{l=N_u-1/2} \right\rangle_{\mathbf{x}_i, mn} \\
&+ \sum_{n=0}^{N_w-1} \sum_{l=0}^{N_u-1} h_u h_w \left\langle \nu \left[(v - V^c) f + \frac{T^c}{m} \frac{\partial f}{\partial v} \right]_{m=-1/2}^{m=N_v-1/2} \right\rangle_{\mathbf{x}_i, ln} \\
&+ \sum_{m=0}^{N_w-1} \sum_{l=0}^{N_u-1} h_u h_v \left\langle \nu \left[(w - W^c) f + \frac{T^c}{m} \frac{\partial f}{\partial w} \right]_{n=-1/2}^{n=N_w-1/2} \right\rangle_{\mathbf{x}_i, lm} . \quad (4.10)
\end{aligned}$$

Exact numerical conservation of cell-averaged density is accomplished by setting f and $\partial f / \partial \mathbf{v}$ to zero at both the upper ($\mathbf{v}_l = N_{\mathbf{v}} - 1/2$) and lower ($\mathbf{v}_l = -1/2$) domain boundaries in each velocity dimension [49–52]. These boundary conditions are actually just the finite velocity space domain analog of the conditions for f and $\partial f / \partial \mathbf{v}$ in an infinite analytical domain.

How the conservative mean velocity $\mathbf{U}^c$ and temperature T^c are defined in order to obtain exact numerical conservation of momentum and energy depends on the order of accuracy of Eq. 4.8 in real space. Assume that only 2nd order accuracy in real space is required, then, since the cell-average of a product equals the product of cell-averages to 2nd order ($\langle fg \rangle_{x_i} = \langle f \rangle_{x_i} \langle g \rangle_{x_i} + O(h_x^2)$), Eq. 4.8 can be written in the following simplified form:

$$\frac{\partial \langle f \rangle_{\mathbf{x}_i, \mathbf{v}_l}}{\partial t} = \left\langle \Psi^0_{\mathbf{v}_l} \right\rangle_{\mathbf{x}_i} - \langle \mathbf{U}^c \rangle_{\mathbf{x}_i} \cdot \left\langle \mathbf{\Psi}^U_{\mathbf{v}_l} \right\rangle_{\mathbf{x}_i} + \langle T^c \rangle_{\mathbf{x}_i} \left\langle \Psi^T_{\mathbf{v}_l} \right\rangle_{\mathbf{x}_i} , \quad (4.11)$$

where the $\Psi_{\mathbf{v}_l}$ functions are defined as

$$\Psi^0_{\mathbf{v}_l} = \frac{\nu}{h_u}\left\langle [uf]^{l+1/2}_{l-1/2}\right\rangle_{mn} + \frac{\nu}{h_v}\left\langle [vf]^{m+1/2}_{m-1/2}\right\rangle_{ln} + \frac{\nu}{h_w}\left\langle \nu\,[wf]^{n+1/2}_{n-1/2}\right\rangle_{lm}, \quad (4.12)$$

$$\mathbf{\Psi}^U_{\mathbf{v}_l} = \frac{\nu}{h_u}\left\langle [f]^{l+1/2}_{l-1/2}\right\rangle_{mn}\hat{\mathbf{x}} + \frac{\nu}{h_v}\left\langle [f]^{m+1/2}_{m-1/2}\right\rangle_{ln}\hat{\mathbf{y}} + \frac{\nu}{h_w}\left\langle [f]^{n+1/2}_{n-1/2}\right\rangle_{ln}\hat{\mathbf{z}}, \quad (4.13)$$

$$\Psi^T_{\mathbf{v}_l} = \frac{\nu}{h_u}\left\langle \left[\frac{\partial f}{\partial u}\right]^{l+1/2}_{l-1/2}\right\rangle_{mn} + \frac{\nu}{h_v}\left\langle \left[\frac{\partial f}{\partial v}\right]^{m+1/2}_{m-1/2}\right\rangle_{ln} + \frac{\nu}{h_w}\left\langle \left[\frac{\partial f}{\partial w}\right]^{n+1/2}_{n-1/2}\right\rangle_{lm} \quad (4.14)$$

The exact numerical conservation of momentum and energy is accomplished by defining $\langle \mathbf{U}^c\rangle_{\mathbf{x}_i}$ and $\langle T^c\rangle_{\mathbf{x}_i}$ as the solutions to the the system of equations created by setting the three first numerical moments and the second numerical moment of Eq. 4.11 to zero. The pressure moment of Eq. 4.11 gives

$$\frac{\partial \langle nT\rangle_{\mathbf{x}_i}}{\partial t} = \int_{\Omega_\mathbf{v}} \frac{m}{3} v'^2 \left\langle \Psi^0_{\mathbf{v}_l}\right\rangle_{\mathbf{x}_i} d\mathbf{v} - \langle \mathbf{U}^c\rangle_{\mathbf{x}_i} \cdot \int_{\Omega_\mathbf{v}} \frac{m}{3} v'^2 \left\langle \mathbf{\Psi}^U_{\mathbf{v}_l}\right\rangle_{\mathbf{x}_i} d\mathbf{v} + \langle T^c\rangle_{\mathbf{x}_i} \int_{\Omega_\mathbf{v}} \frac{m}{3} v'^2 \left\langle \Psi^T_{\mathbf{v}_l}\right\rangle_{\mathbf{x}_i} d\mathbf{v} = 0, \quad (4.15)$$

and the mean velocity moment gives the following three equations:

$$\frac{\partial \langle n\mathbf{U}\rangle_{\mathbf{x}_i}}{\partial t} = \int_{\Omega_\mathbf{v}} \mathbf{v} \left\langle \Psi^0_{\mathbf{v}_l}\right\rangle_{\mathbf{x}_i} d\mathbf{v} - \langle \mathbf{U}^c\rangle_{\mathbf{x}_i} \cdot \int_{\Omega_\mathbf{v}} \left\langle \mathbf{\Psi}^U_{\mathbf{v}_l}\right\rangle_{\mathbf{x}_i} \mathbf{v} d\mathbf{v} + \langle T^c\rangle_{\mathbf{x}_i} \int_{\Omega_\mathbf{v}} \mathbf{v} \left\langle \Psi^T_{\mathbf{v}_l}\right\rangle_{\mathbf{x}_i} d\mathbf{v} = 0. \quad (4.16)$$

For example, consider a problem where the mean velocity vector is zero. The conservative temperature would then be defined as

$$\langle T^c\rangle_{\mathbf{x}_i} \equiv \frac{-\int_{\Omega_\mathbf{v}} \frac{m}{3} v'^2 \langle \Psi^0_{\mathbf{v}_l}\rangle_{\mathbf{x}_i} d\mathbf{v}}{\int_{\Omega_\mathbf{v}} \frac{m}{3} v'^2 \left\langle \Psi^T_{\mathbf{v}_l}\right\rangle_{\mathbf{x}_i} d\mathbf{v}}. \quad (4.17)$$

The difference between $\langle \mathbf{U}^c\rangle_{\mathbf{x}_i}$ and $\langle T^c\rangle_{\mathbf{x}_i}$ defined by the solutions of Eq's 4.15-4.16 and $\langle \mathbf{U}\rangle_{\mathbf{x}_i}$ and $\langle T\rangle_{\mathbf{x}_i}$ interpreted from Eq's 4.9 depends on the velocity space domain size, grid resolution, and the interpolation and differencing methods used to formulate the fluxes. However, in the limit where the velocity domain goes to infinity and the grid spacing goes to zero, they are equivalent. Note that it is

the fact that the coefficients $\mathbf{U}$ and T in Eq. 4.5 are independent of velocity that allows for the exact numerical conservation of the velocity space moments. The full Fokker-Planck operator has velocity dependent coefficients and therefore this method cannot be used to conserve the numerical moments of it.

4.2 COGENT Implementation

The numerical scheme above for Eq. 4.5 has been implemented into the 2D2V gyrokinetic code COGENT as a model collision operator for like-like species collisions. COGENT is a kinetic code designed to study plasma phenomena in the edge region of magnetic confinement devices and uses the parallel velocity $v_\parallel = \mathbf{v}\cdot\hat{\mathbf{b}}$ and magnetic moment $\mu = \frac{m}{2}v_\perp^2/B$ velocity space coordinate system. The 2V grid is a simplified version of the full 3V grid and is used to study the evolution of the gyroangle independent distribution function. Eq. 4.11 written in this coordinate system for the gyrophase independent distribution function is

$$\frac{\partial f}{\partial t}|_c = \nu\left[\frac{\partial}{\partial v_\parallel}\left(\left(v_\parallel - U_\parallel\right) + \frac{T}{m}\frac{\partial f}{\partial v_\parallel}\right) + \frac{\partial}{\partial \mu}\left(2\mu f + \frac{2\mu T}{B}\frac{\partial f}{\partial \mu}\right)\right]. \tag{4.18}$$

The thermal relaxation of initially non-Maxwellian distribution functions to Maxwellian are considered for initial testing of this model collision operator. All variables are taken to be homogeneous in real space for initial testing purposes. The relaxation of a distribution function with $U_\parallel = 0$ to a Maxwellian along with the the evolution of the percent error from the exact Maxwellian are shown in Fig. 4.1 with contour plots in velocity space. The contours lines for a Maxwellian distribution function in the plane spanned by $\hat{v}_\parallel = v_\parallel/v_T$ and $\hat{v}_\perp = v_\perp/v_T$ correspond to the equation of semi-circles since $f_M = f_M\left(\hat{v}_\parallel^2 + \hat{v}_\perp^2\right)$. Notice that the distribution function relaxes to a Maxwellian on the collisional time scale and remains there at longer times. Also notice that the maximum error from an exact Maxwellian is about 10% and is concentrated in the corners of the velocity domain, which is where one would like the error to be concentrated. The grid resolution in the velocity domain is 40x40 and the domain boundaries in each dimension are about

$2.5v_T$. The time evolution of the error in the density and temperature from their initial values corresponding to the results shown in Fig. 4.1 are displayed in Fig. 4.2 a). The error in the density and temperature are both on the order of the machine accuracy and are completely negligible.

The results from a similar test with a finite $U_\parallel$ are displayed in Fig. 4.2 b) and Fig. 4.3. The results of this test are similar to those discussed above for the test results shown in Fig. 4.1 and Fig. 4.2 a). The error in the density, temperature, and mean velocity are all on the order of the machine accuracy.

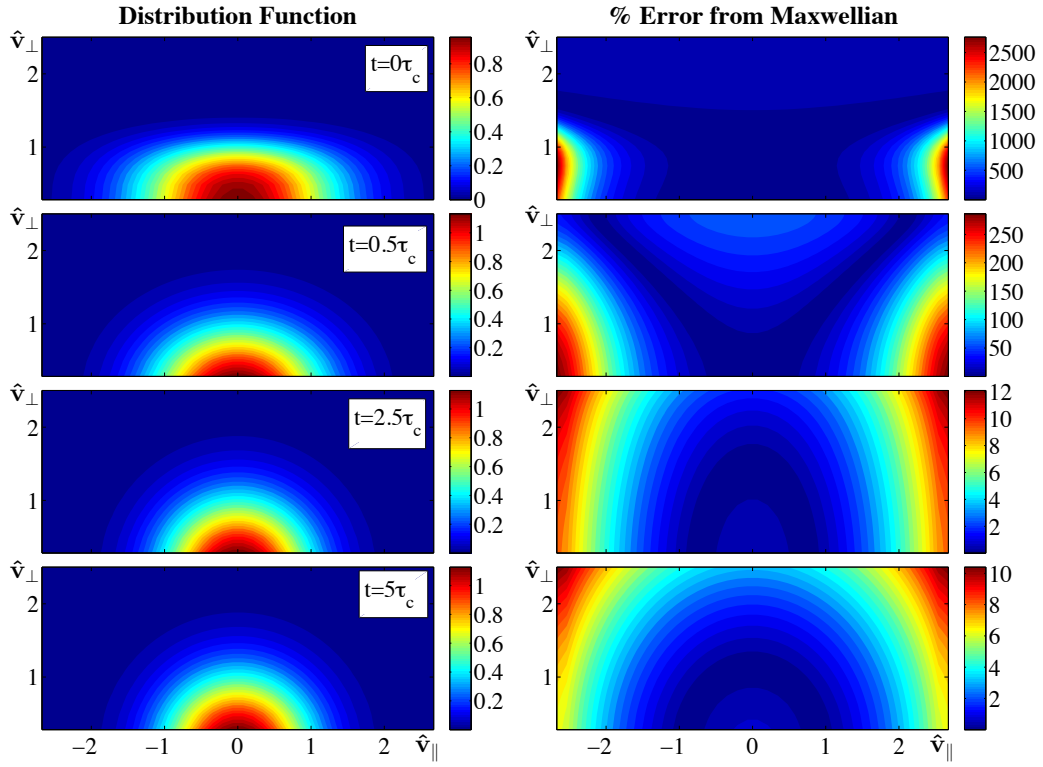

Figure 4.1: Relaxation of distribution function with no mean velocity to Maxwellian (left) and corresponding percent error from exact Maxwellian (right). The velocity coordinates are normlized by the thermal velocity $v_T = \sqrt{2T/m}$.

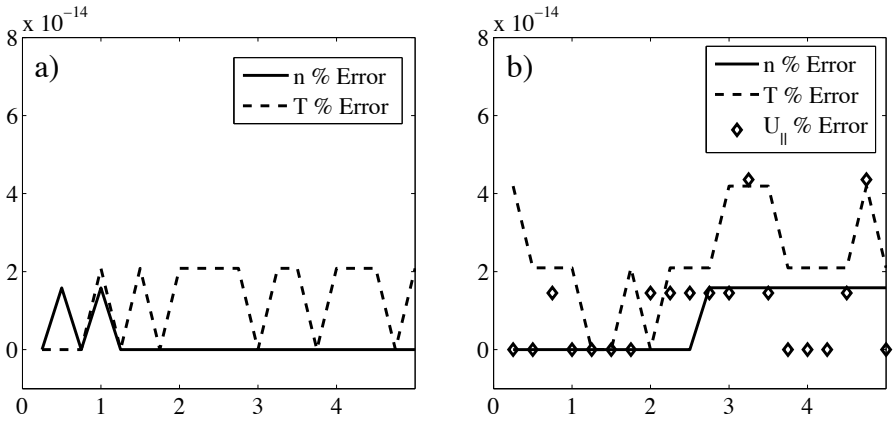

Figure 4.2: Velocity space moments percent error versus time normalized by the collision time $\tau_c = 1/\nu$. The curves in figure a) correspond to the results shown in Fig. 4.1 and the curves in figure b) correspond to the results shown in Fig. 4.3. The percent error is calulated from the numerical moments of the distribution function at $t = 0$ and are all on the order of the machine accuracy.

4.3 Conclusion

The Fokker-Planck equation for Brownian motion is considered as a model collision operator for like-like particles collisions in a plasma for numerical algorithms. This model operator drives the distribution function to a Maxwellian with drag and diffusion while conserving the density, momentum, and energy of the system. The operator is very appealing for numerical implementation because exact numerical conservation of the relevant velocity space moments can be captured to a high degree of accuracy with relatively little computation effort with respect to the full nonlinear operator. The conservation of density is captured numerical by use of the finite volume method and appropriately defining the boundary conditions at the velocity domain boundaries. The conservation of momentum and energy is captured by solving for the mean velocity vector $\mathbf{U}$ and temperature T used on the right-hand side of the operator from the system of equations created by setting the three first numerical moments and the second numerical moment of the operator to zero.

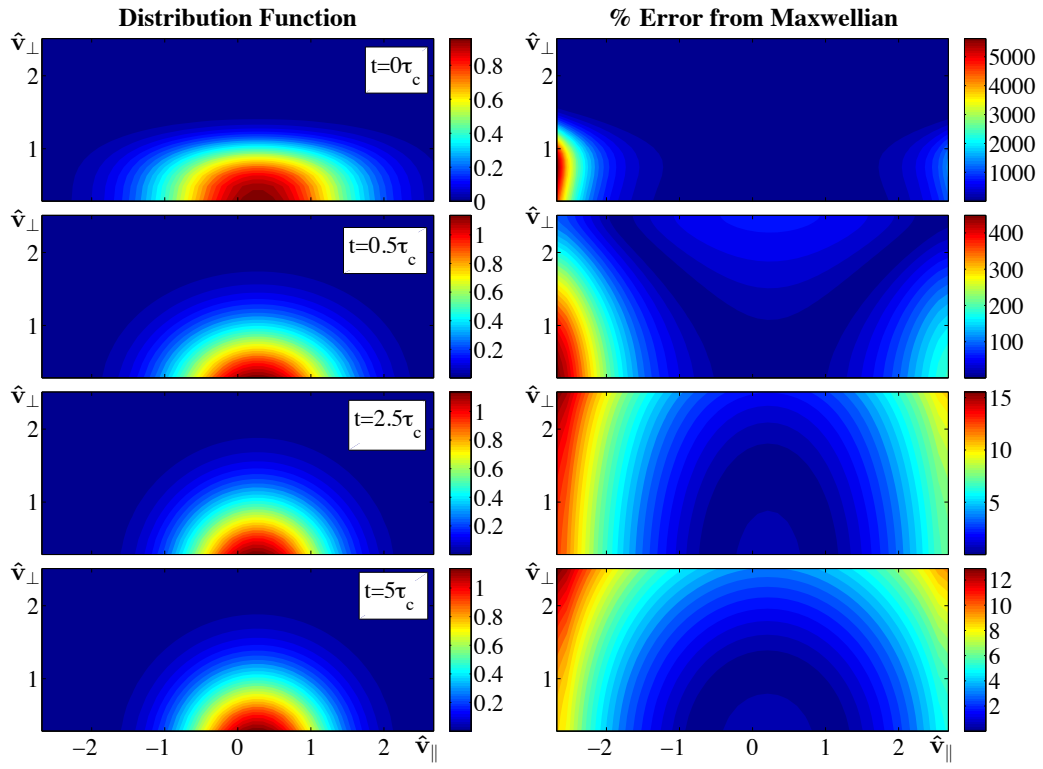

Figure 4.3: Relaxation of distribution function with finite mean parallel velocity to Maxwellian (left) and corresponding percent error from exact Maxwellian (right). The velocity coordinates are normlized by the thermal velocity $v_T = \sqrt{2T/m}$.

The model has been implemented into the 2D2V gyrokinetic code COGENT and two different thermalization tests are considered for testing purposes. In both tests, the distribution function is shown to relax to a Maxwellian on the collisional time scale and to remain there at long times. The maximum error at long times from an exact Maxwellian is concentrated at the velocity space domain corners. The error in the density, mean parallel velocity, and temperature from their initial values are all on the order of the machine accuracy and completely negligible.

Chapter 5

Anomalous Transport Model for Kinetic Simulations

The cross field transport in tokamaks is dominated by anomalous processes driven by turbulent fluctuations. The time scale of these turbulent fluctuations is typically much faster than time scale of the transport and mean profile evolution. Therefore, a numerically economic tokamak transport code should include a model to represent the effects of anomalous transport on the mean profiles rather than fully resolving the turbulent fluctuations. A cross flux surface transport model of anomalous transport due to electrostatic fluctuations in magnetically confined plasmas is the topic of this Chapter.

One of the difficulties in simulating tokamak plasmas is that there are many different time and spatial scales that exist. The drift-kinetic equation [59] is a reduction of the full kinetic equation used to study phenomena in highly magnetized systems where the time and spatial scales of interest are, respectively, much larger than the gyration time and gyro-radius of each species. The gyro-kinetic equations are an extension of the drift-kinetic equation that account for spatial scales comparable to the ion gyro-radius [60–62]. The time scale of electrostatic fluctuations in magnetic confinement devices is much larger than that of the gyration time of each species, but typically small compared to the mean parameter evolution time

scale. Thus, the equation for the evolution of the time-averaged distribution function (averaged over the turbulence correlation time) due to anomalous processes, and the corresponding equations for anomalous density and heat evolution, are formulated in this work from the gyro-kinetic equation. However, for initial implementation of the model into a numerical algorithm, the equations are analyzed in the drift-kinetic limit and finite ion larmor radius effects are deferred to future work.

The physics (or lack there of) really enters in how one chooses to model the anomalous flux. The structure and parameters of the anomalous flux can be determined from experimental data, from the results of numerical studies that fully resolve the turbulent fluctuations, or from a theoretical basis. The anomalous cross field flux in this paper is modeled in the conventional advective-diffusion manner [15, 56, 63, 64] and, for testing purposes, designed to be able to match typical transport models of density and heat in standard fluid transport models. The model has been implemented in the 2D2V gyrokinetic code COGENT [55, 65] and results from several successful tests are presented.

5.1 Anomalous Electrostatic Transport

Consider the gyro-kinetic equation for the gyro-phase independent distribution function $f(t, \mathbf{R}, v_\parallel, \mu)$ in highly magnetized plasmas:

$$\frac{\partial f}{\partial t} + \frac{1}{B_\parallel^*}\nabla_{\mathbf{R}} \cdot \left(B_\parallel^* \dot{\mathbf{R}} f\right) + \frac{1}{B_\parallel^*}\frac{\partial}{\partial v_\parallel}\left(B_\parallel^* \dot{v}_\parallel f\right) = C, \tag{5.1}$$

where $\dot{\mathbf{R}}\left(v_\parallel, \mathbf{R}\right) = v_\parallel \hat{\mathbf{b}} + \mathbf{U}_\perp$ with $\mathbf{U}_\perp = \mathbf{U}_\perp\left(v_\parallel, \mu, \mathbf{R}\right)$ the magnetic drift velocity, $v_\parallel$ is the parallel velocity coordinate, $\mu = \frac{1}{2}mv_\perp^2/B$ is the magnetic moment with magnetic field magnitude $B = |\mathbf{B}|$ and species mass m, C represents the velocity space collision operator, and $B_\parallel^*\left(\mathbf{R}, v_\parallel\right)/m$ is the velocity space Jacobian. In the electrostatic limit and with no background potential, $B_\parallel^*$ is defined as

$$B_\parallel^* = \mathbf{B}_\parallel^*\left(\mathbf{R}, v_\parallel\right) \cdot \hat{\mathbf{b}} = B + \frac{mv_\parallel}{Ze}\nabla_{\mathbf{R}} \times \hat{\mathbf{b}} \cdot \hat{\mathbf{b}}. \tag{5.2}$$

The absence of a phase space flux in the μ direction is a consequence of the conservation of a particle's magnetic moment in strong magnetic fields (i.e. $\dot{\mu} = 0$). A more detailed description of Eq's 5.1-5.2 can be found in [60–62].

An equation governing the mean time averaged distribution function is obtained by first splitting the time-dependent quantities into a mean and oscillatory part: $g = \langle g \rangle + \tilde{g}$ where $\langle g \rangle \equiv \frac{1}{\tau_c} \int_t^{t+\tau_c} g dt$ with τ_c the turbulence correlation time, and then time-averaging Eq. 5.1. By definition, $\langle \tilde{g} \rangle = 0$. Time averaging Eq. 5.1 yields

$$\begin{aligned} \frac{\partial \langle f \rangle}{\partial t} &+ \frac{1}{B_\parallel^*} \nabla_{\mathbf{R}} \cdot \left(B_\parallel^* \left\langle \dot{\mathbf{R}} \right\rangle \langle f \rangle \right) + \frac{1}{B_\parallel^*} \frac{\partial}{\partial v_\parallel} \left(B_\parallel^* \langle \dot{v}_\parallel \rangle \langle f \rangle \right) \\ &+ \frac{1}{B_\parallel^*} \nabla_{\mathbf{R}} \cdot \left(B_\parallel^* \left\langle \tilde{\dot{\mathbf{R}}}_\perp \tilde{f} \right\rangle \right) + \frac{1}{B_\parallel^*} \frac{\partial}{\partial v_\parallel} \left(B_\parallel^* \left\langle \tilde{\dot{v}}_\parallel \tilde{f} \right\rangle \right) = \langle C \rangle . \end{aligned} \tag{5.3}$$

The brackets on the mean values can now be dropped for convenience and the time averaged equation can be written in the following form:

$$\frac{\partial f}{\partial t} + \frac{1}{B_\parallel^*} \nabla_{\mathbf{R}} \cdot \left(B_\parallel^* \dot{\mathbf{R}} f \right) + \frac{1}{B_\parallel^*} \frac{\partial}{\partial v_\parallel} \left(B_\parallel^* \dot{v}_\parallel f \right) + \nabla \cdot \mathbf{\Gamma}_a = C, \tag{5.4}$$

where the last term on the left hand side represents the anomalous transport due to the coupling of fluctuating quantities and is defined as

$$\nabla \cdot \mathbf{\Gamma}_a \equiv \frac{1}{B_\parallel^*} \nabla_{\mathbf{R}} \cdot \left(B_\parallel^* \left\langle \tilde{\mathbf{U}}_\perp \tilde{f} \right\rangle \right) + \frac{1}{B_\parallel^*} \frac{\partial}{\partial v_\parallel} \left(B_\parallel^* \left\langle \tilde{\dot{v}}_\parallel \tilde{f} \right\rangle \right) . \tag{5.5}$$

For the purpose of analyzing and discussing the evolution of the time-averaged parameters due to anomalous transport, all terms but the anomalous transport are ignored and the following simplified governing equation is examined:

$$\frac{\partial f}{\partial t} + \nabla \cdot \mathbf{\Gamma}_a = 0. \tag{5.6}$$

The contribution of the anomalous flux to the density n, parallel momentum $M_\parallel = nU_\parallel$, and heat $Q = 3nT/2$ evolution are determined by taking the density, parallel velocity, and heat moments of Eq. 5.6. Due to finite gyroradius effects, the velocity space moments of Eq. 5.1 are quite complicated [60]. However, in the small gyroradius limit, $k_\perp \rho << 1$, where $k_\perp$ is the characteristic transverse gradient

scale and ρ is the species gyroradius, the relevant velocity space moments of the gyro-angle independent distribution function simplify to their conventional forms:

$$\left(n,\ nU_{\parallel},\ nT\right) = 2\pi \int_0^\infty \int_{-\infty}^\infty \left(1,\ v_{\parallel},\ \frac{m}{3}v'^2\right) f \frac{B_{\parallel}^*}{m} dv_{\parallel} d\mu, \tag{5.7}$$

where $v'^2 = \left(v_{\parallel} - U_{\parallel}\right)^2 + \frac{2B}{m}\mu$. Note that this definition of pressure is only valid when the drift velocity is small with respect to the thermal velocity, which is an assumption used in deriving Eq. 5.1.

The evolution of the moments defined in Eq. 5.7 due to anomalous process are determined by taking the corresponding velocity space moments of Eq. 5.6. Care should be taken when computing these moments since the magnetic moment μ is an independent variable in gyrokinetic coordinates. Therefore, the real space divergence is taken at constant μ rather than at constant $v_\perp$ and the resulting equations are

$$\frac{\partial n}{\partial t} + \nabla_{\mathbf{R}} \cdot \mathbf{\Gamma}_n = 0, \tag{5.8}$$

$$\frac{\partial M_{\parallel}}{\partial t} + \nabla_{\mathbf{R}} \cdot \mathbf{\Gamma}_{M_{\parallel}} = \left\langle \tilde{n}\tilde{\dot{v}}_{\parallel} \right\rangle, \tag{5.9}$$

$$\frac{\partial Q}{\partial t} + \nabla_{\mathbf{R}} \cdot \mathbf{\Gamma}_Q = \mathbf{\Gamma}_{Q_\perp} \cdot \nabla_{\mathbf{R}} \ln(B), \tag{5.10}$$

where the anomalous particle, parallel momentum, and heat flux are defined as

$$\left(\mathbf{\Gamma}_n,\ \mathbf{\Gamma}_{M_{\parallel}},\ \mathbf{\Gamma}_Q\right) \equiv 2\pi \int_0^\infty \int_{-\infty}^\infty \left(1,\ v_{\parallel},\ \frac{m}{2}v'^2\right) \left\langle \tilde{\mathbf{U}}_\perp \tilde{f} \right\rangle \frac{B_{\parallel}^*}{m} dv_{\parallel} d\mu. \tag{5.11}$$

The "effective" source/sink of parallel momentum on the RHS of Eq. 5.9 and the perpendicular heat flux $\mathbf{\Gamma}_{Q_\perp}$ in the "effective" source/sink of thermal energy in Eq. 5.10 are defined respectively as

$$\mathbf{\Gamma}_{Q_\perp} \equiv 2\pi \int_0^\infty \int_{-\infty}^\infty \frac{m}{2} v_\perp'^2 \left\langle \tilde{\mathbf{U}}_\perp \tilde{f} \right\rangle \frac{B_{\parallel}^*}{m} dv_{\parallel} d\mu \tag{5.12}$$

$$\left\langle \tilde{\dot{v}}_{\parallel} \tilde{n} \right\rangle \equiv 2\pi \int_0^\infty \int_{-\infty}^\infty \left\langle \tilde{\dot{v}}_{\parallel} \tilde{f} \right\rangle \frac{B_{\parallel}^*}{m} dv_{\parallel} d\mu. \tag{5.13}$$

The "effecive" sink/source on the RHS of Eq. 5.10 is a result of the conservation of magnetic moment. If the anomalous flux brings particles from a region of lower magnetic field into a region of higher magnetic field, or vice a versa, then the particles will gain, or lose, thermal perpendicular energy such that the adiabatic moment remains the same. This term may not be too significant in transport studies of the edge region of tokamaks, where the SOL width is typically small compared to the major radius, but could be important in the core.

5.2 Anomalous Cross-Field Transport Model

The anomalous flux of the gyro-center distribution function that arises due to the coupling of electrostatic fluctuations has a real space component ($\left\langle \tilde{\mathbf{U}}_{\perp} \tilde{f} \right\rangle$) and a velocity space component ($\left\langle \tilde{v}_{\parallel} \tilde{f} \right\rangle$). The anomalous real space flux itself has two components - a component that is normal to the magnetic field and lies in the plane of the magnetic flux surfaces, and one that is normal to both the magnetic field and the magnetic flux surfaces. Transport along field lines is typically much faster than transport across field lines and so, to lowest order, the plasma parameters are considered to be constant along magnetic flux surfaces. Moreover, it is this piece of the anomalous flux that directly affects plasma confinement and is therefore of the most interest. The simplified form of the anomalous transport considered here is

$$\mathbf{\Gamma}_a = \Gamma_{\Psi} \hat{\mathbf{e}}_{\Psi}, \tag{5.14}$$

where Ψ represents the direction normal to magnetic flux surfaces (see Fig. 5.1).

The goal is to model the anomalous cross field flux $\Gamma_{\Psi} = \left\langle \tilde{U}_{\Psi} \tilde{f} \right\rangle$ in the absence of fully resolving the turbulent fluctuations. The anomalous cross magnetic flux surface flux is typically considered to be proportional to gradients of plasma parameters across flux surfaces. Care should be taken when computing these derivatives operating in a Gyrokinetic coordinate system where the independent variable μ is implicitly a function of space. The gradients of parameters across flux surfaces in a gyrokinetic coordinate system may be obtained by using the chain

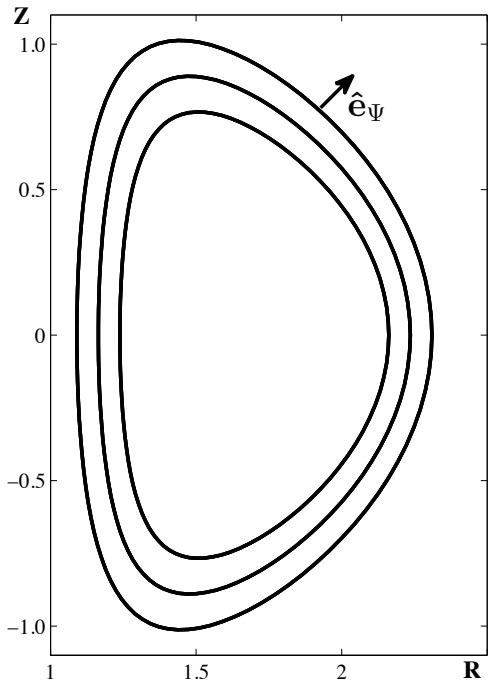

Figure 5.1: Example cross section of magnetic flux surfaces in tokamak. The unit vector $\hat{\mathbf{e}}_\Psi$ is always normal to the flux surfaces. R is the major radius, Z is the axial dimension, and the toroidal magnetic field is normal to the Z-R plane.

rule of differentiation to transform the spatial gradients across flux surfaces to the gyrokinetic coordinate system:

$$\nabla_\Psi \mid_{\mathbf{v}} = \nabla_\Psi \mid_\mu + \nabla_\Psi \mid_{\mathbf{v}} \mu \frac{\partial}{\partial \mu} = \nabla_\Psi \mid_\mu - \frac{\mu}{B} \nabla_\Psi B \frac{\partial}{\partial \mu}, \tag{5.15}$$

where $\nabla_\Psi \equiv \partial / \partial x_\Psi / h_\Psi$ is the component of the real space gradient in the direction normal to the magnetic flux surfaces.

Anomalous transport normal to magnetic flux surfaces is often not accurately captured by assuming a flux that is only proportional to the gradients of plasma parameters. The flux is considered to also have an advective component. Therefore, the general form of the anomalous flux normal to flux surfaces is considered to be a combination of convective and diffusive components:

$$\Gamma_\Psi = U_\Psi f - D_\Psi \nabla_\Psi \mid_{\mathbf{v}} f, \tag{5.16}$$

where $U_\Psi \left(\mathbf{R}, \mathbf{v} \right)$ and $D_\Psi \left(\mathbf{R}, \mathbf{v} \right)$ are respectively the advection and diffusion coef-

ficients. The coefficients U_Ψ and D_Ψ can be formulated from mathematical and physical derivations, experimental data, data from simulations that fully resolve the turbulence, or in such a way as to match some desired transport equations for the density and heat fluxes. The latter approach is the most practical choice for initial implementation and testing purposes and is the adopted approach in the following sections.

5.3 Fluid Model

The particle and heat transport fluxes in collisional fluid and neoclassical theories are driven by the cross flux surface gradients of density and temperature. The general form is written as

$$-\Gamma_n = D_{11}\nabla_\Psi n + D_{12} n \frac{1}{T}\nabla_\Psi T, \tag{5.17}$$

$$-\Gamma_Q = D_{21} T \nabla_\Psi n + D_{22} n \nabla_\Psi T. \tag{5.18}$$

The coefficients D_{ij} form the transport matrix. In General, the transport matrices are different for electrons, each ions species, and impurities. Also, the fluxes for one species can depend on gradients of parameters of other species. However, for simplicity in discussing the development of the model, only transport of one species that depends on gradients of its own parameters is considered here. The diagonal elements D_{11} and D_{22} are, respectively, known as the particle diffusivity D_n and heat diffusivity χ. It should be mentioned that the cross flux surface fluxes in neoclassical theory are averaged over the flux surfaces and actually depend on gradients of the flux surface averaged density and temperature. However, the fluxes in Eq.'s 5.17 and 5.18 are considered here to be in general varying along flux surfaces. This is because the kinetic transport model, which is going to use to match the fluid fluxes in Eq.'s 5.17 and 5.18, is to be used in a 2D2V kinetic code where all parameters in general vary along the field line.

In order to use the general form of the anomalous cross field flux given in Eq.

5.16 to reproduce the transport matrix given in Eqs 5.17-5.18, consider a diffusion and convection coefficient of the following form:

$$D_\Psi = D_0, \tag{5.19}$$

$$U_\Psi = \frac{D_{n0}}{n}\nabla_\Psi n + \frac{D_{T0}}{T}\nabla_\Psi T + \left(\frac{v'^2}{v_{th}^2} - \frac{3}{2}\right)\left(\frac{D_{n2}}{n}\nabla_\Psi n + \frac{D_{T2}}{T}\nabla_\Psi T\right). \tag{5.20}$$

The fluid transport matrix is found by taken the density and thermal energy moments of the kinetic flux (Eq. 5.16). With the coefficients defined above in Eq.'s 5.19 and 5.20, the corresponding fluid fluxes are

$$-\Gamma_n \equiv -\int_{\mathbf{v}} \Gamma_\Psi d\mathbf{v} = \left(D_0 - D_{n0}\right)\nabla_\Psi n - D_{T0}\frac{n}{T}\nabla_\Psi T \tag{5.21}$$

$$\begin{aligned} -\Gamma_Q \equiv -\int_{\mathbf{v}} \frac{mv'}{2}\Gamma_\Psi d\mathbf{v} &= \frac{3}{2}\left(D_0 - D_{n0} - D_{n2}C_4\right)T\nabla_\Psi n \\ &+ \frac{3}{2}\left(D_0 - D_{T0} - D_{T2}C_4\right)n\nabla_\Psi T, \end{aligned} \tag{5.22}$$

where the constant C_4 is defined as

$$C_4 \equiv \frac{2}{3nT^2}\int_{\mathbf{v}} \left(\frac{1}{2}mv'^2\right)^2 f d\mathbf{v} - \frac{3}{2}. \tag{5.23}$$

Note that $C_4 = 1$ for a Maxwellian distribution function. The relation between the transport matrix coefficients and the kinetic coefficients in matrix format is

$$\begin{bmatrix} D_{11} \\ D_{12} \\ D_{21} \\ D_{22} \end{bmatrix} + D_{n0}\begin{bmatrix} 1 \\ 0 \\ 3/2 \\ 0 \end{bmatrix} = \begin{pmatrix} 1 & 0 & 0 & 0 \\ 0 & -1 & 0 & 0 \\ 3/2 & 0 & -3/2 & 0 \\ 3/2 & -3/2 & 0 & -3/2 \end{pmatrix}\begin{bmatrix} D_0 \\ D_{T0} \\ D_{n2}C_4 \\ D_{T2}C_4 \end{bmatrix} \tag{5.24}$$

The parameter D_{n0} is considered to be the free parameter used to insure that the kinetic diffusion coefficient D_0 is always greater than zero. Since the fluid transport matrix coefficients are always greater than or equal to zero, this free parameter is only needed for the special case when D_{11} is zero. This is purely a numerical requirement since purely advective schemes are inherently numerically unstable

with standard central finite difference schemes. This can also be remedied by using upwinding schemes to model to advective portion of the kinetic flux. However, the problem is treated numerically using the standard central finite differences and interpolating schemes and defer more advanced schemes to future work. A Von-Nuemman stability analysis of the transport model is given in Appendix C.

Neglecting the free parameter, the inverse relation is

$$\begin{bmatrix} D_0 \\ D_{T0} \\ D_{n2}C_4 \\ D_{T2}C_4 \end{bmatrix} = \begin{pmatrix} 1 & 0 & 0 & 0 \\ 0 & -1 & 0 & 0 \\ 1 & 0 & -2/3 & 0 \\ 1 & 1 & 0 & -2/3 \end{pmatrix} \begin{bmatrix} D_{11} \\ D_{12} \\ D_{21} \\ D_{22} \end{bmatrix} \tag{5.25}$$

Note that C_4 cannot be zero.

5.4 Verification Tests

The numerical model has been implemented into the 2D2V gyrokinetic code COGENT. Results from several numerical simulation tests are presented in this section to demonstrate that the kinetic transport model can correctly reproduce results from fluid transport matrices. The equation for the steady state solution of density from Eq. 5.8 with density flux defined in Eq. 5.17 with spatially invariant coefficients and $D_{11} \neq 0$ is

$$\frac{\partial}{\partial x_\Psi}\left(\frac{J}{h_\Psi^2 T^\alpha}\frac{\partial}{\partial x_\Psi}\left(nT^\alpha\right)\right) = 0, \tag{5.26}$$

where J is the real space Jacobian, h_Ψ is the Ψ metric (i.e., if the magnetic flux surfaces are perfectly toroidal, then $x_\Psi = r$, $J = 2\pi r R$, and $h_\Psi = 1$), and $\alpha = D_{12}/D_{11}$.

The steady state solution of the temperature requires some knowledge of the distribution function so that $\Gamma_{Q_\perp}$ can be expressed in terms of Γ_Q. If the distribution function is isotropic about the mean velocity in velocity space, then $\Gamma_{Q_\perp} = \frac{2}{3}\Gamma_Q$ and the equation for the steady state solution of the temperature can

be written as

$$\frac{\partial}{\partial x_\Psi}\left(\frac{J}{h_\Psi^2 B^{2/3}}\Gamma_Q\right) = 0. \tag{5.27}$$

Note that the factor of $B^{2/3}$ in the denominator comes from the conservation of magnetic moment, which acts to drive the plasma away from an isothermal state when particles flux across regions of varying magnetic field strength. So, to ensure that the plasma remains isothermal in the simulations and that Eq. 5.27 holds, the collision operator presented in the previous Chapter is applied to relax the distribution to thermodynamic equilibrium. The distribution function for a plasma in thermodynamic equilibrium takes the form of a Maxwellian:

$$f_M = \frac{n}{\left(\sqrt{\pi} v_{th}\right)^3} \exp\left(-\frac{v'^2}{v_{th}^2}\right), \tag{5.28}$$

where $n = n(\mathbf{x})$ is the density, $v_{th} = \sqrt{2T(\mathbf{x})/m}$ is the thermal velocity. The steady state solution of a heat flux of the form given in Eq. 5.18 for an isothermal distribution function and $D_{22} \neq 0$ reduces to

$$\frac{\partial}{\partial x_\Psi}\left(\frac{J n^{1-\beta}}{h_\Psi^2 B^{2/3}} \frac{\partial}{\partial x_\Psi}\left(n^\beta T\right)\right) = 0, \tag{5.29}$$

where $\beta = D_{21}/D_{22}$.

A circular annulus of a torus is the geometry used in the verification testing. The plane of the annulus is normal to the toroidal direction. The magnetic field is assumed to scale with $1/R$, where $R = R_0 + r\cos(\theta)$ is the major radius, such as the main component of the magnetic field in a tokamak. The geometry of the annulus is specified by the following parameters:

$$R_0 = 1.7, \qquad r_{min} = 0.4, \qquad r_{max} = 0.8.$$

The initial density and temperature profiles are both taken to be in the form of hyperbolic tangent functions and symmetric with respect to the poloidal angle. Toroidal symmetry is implied since the test case is only an annulus of a torus. Dirichlet boundary conditions on both the density and temperature are applied at both the inner and outer radial boundaries. The fixed values at the boundaries are taken to be the the values at $t = 0$.

5.4.1 Test1: Purely Diffusive Kinetic Flux

For the first test, consider a purely diffusive kinetic flux with a constant diffusion coefficient. The kinetic and corresponding fluid transport matrices are

$$-\Gamma_\Psi = D_0 \frac{\partial f}{\partial r} |_{\mathbf{v}}, \tag{5.30}$$

$$-\Gamma_n = D_0 \frac{\partial n}{\partial r}, \tag{5.31}$$

$$-\Gamma_Q = \frac{3}{2} D_0 T \frac{\partial n}{\partial r} + \frac{3}{2} D_0 n \frac{\partial T}{\partial r}. \tag{5.32}$$

The steady state solution of density for this case is

$$\frac{\partial}{\partial r}\left(rR \frac{\partial n}{\partial r} \right) = 0 \quad \Rightarrow \quad n(r,\theta) = n_1 + (n_2 - n_1) \frac{\ln\left(\frac{rR_1}{r_1 R}\right)}{\ln\left(\frac{r_2 R_1}{r_1 R_2}\right)}, \tag{5.33}$$

where the subscripts 1 and 2 refer to the values at the inner and outer radial boundaries, which are technically at $r_1 = r_{min} - \Delta r/2$ and $r_2 = r_{max} + \Delta r/2$ where Δr is the numerical grid spacing in the r-direction. Note that the solution reduce to the steady state solution in a cylinder in the limit as $R_0 \to \infty$. The steady state solution of the temperature is governed by Eq. 5.29 with $\beta = 1$. The results of a numerical simulation of Eq. 5.6 with the flux specified in Eq. 5.30 are shown in Fig. 5.2. The affect of the toroidal geometry is most evident in the left right asymmetry of the steady state temperature profile ($t \to \infty$) shown in the lower right corner of Fig. 5.2. Both the flux surfaced averaged density and temperature are seen to relax to the steady state solutions on the diffusive time scale.

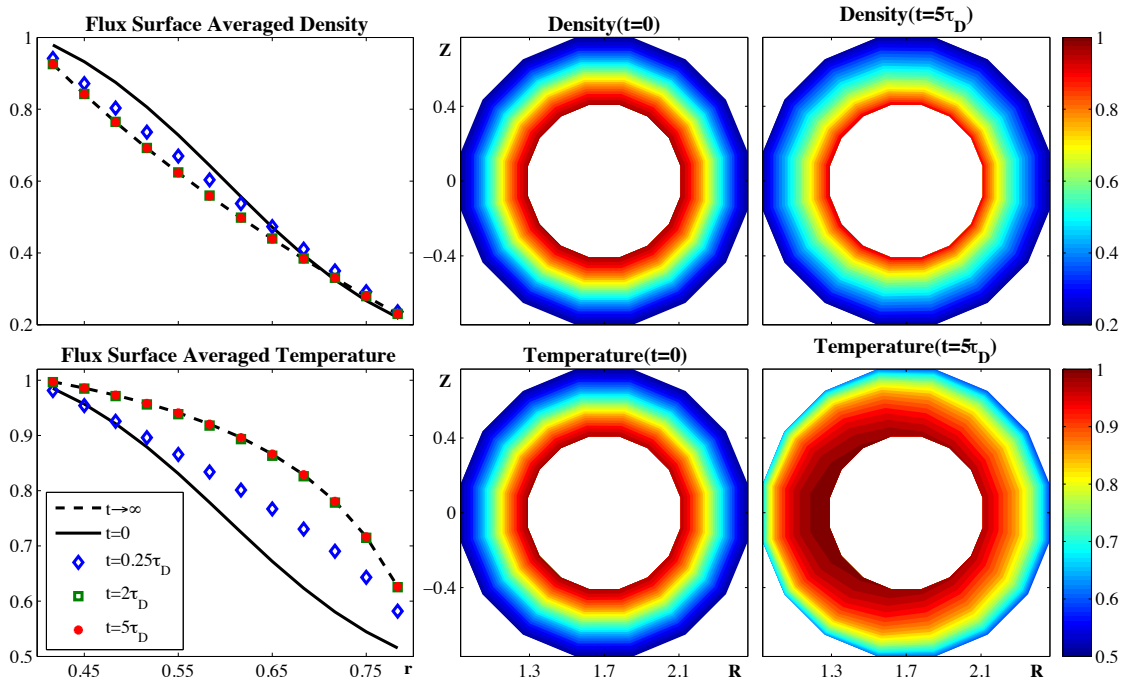

Figure 5.2: Relaxation of flux surface averaged density and temperature profiles for a purely diffusive kinetic flux as specified in Eq. 5.30. The values for $t \to \infty$ are the steady state solutions. The diffusive time is defined as $\tau_D = (0.5(r_{max} - r_{min}))^2/D_0$.

5.4.2 Test2: Purely Diffusive Transport Matrix

Consider a purely diffusive transport matrix ($D_{12} = D_{21} = 0$). The kinetic and corresponding fluid transport matrices are

$$-\Gamma_\Psi = D_{11}\frac{\partial f}{\partial r}\Big|_{\mathbf{v}} - \left(\frac{v'^2}{v_{th}^2} - \frac{3}{2}\right)\left(\frac{D_{11}}{n}\frac{\partial n}{\partial r} + \left(D_{11} - \frac{2}{3}D_{22}\right)\frac{1}{T}\frac{\partial T}{\partial r}\right) f, \quad (5.34)$$

$$-\Gamma_n = D_{11}\frac{\partial n}{\partial r}, \quad (5.35)$$

$$-\Gamma_Q = D_{22}n\frac{\partial T}{\partial r}. \quad (5.36)$$

The steady state solution of the density is the same as in Test 1 and the steady state solution of the temperature is governed by Eq. 5.29 with $\beta = 0$. The heat diffusivity $\chi = D_{22}$ is taken to be three times the particle diffusivity $D_n = D_{11}$ for the numerical simulation of Eq. 5.6 with the flux specified in Eq. 5.34. The

results are shown in Fig. 5.3. Notice that the flux surface average temperature profile doesn't fully relax to the steady state until the density has relaxed.

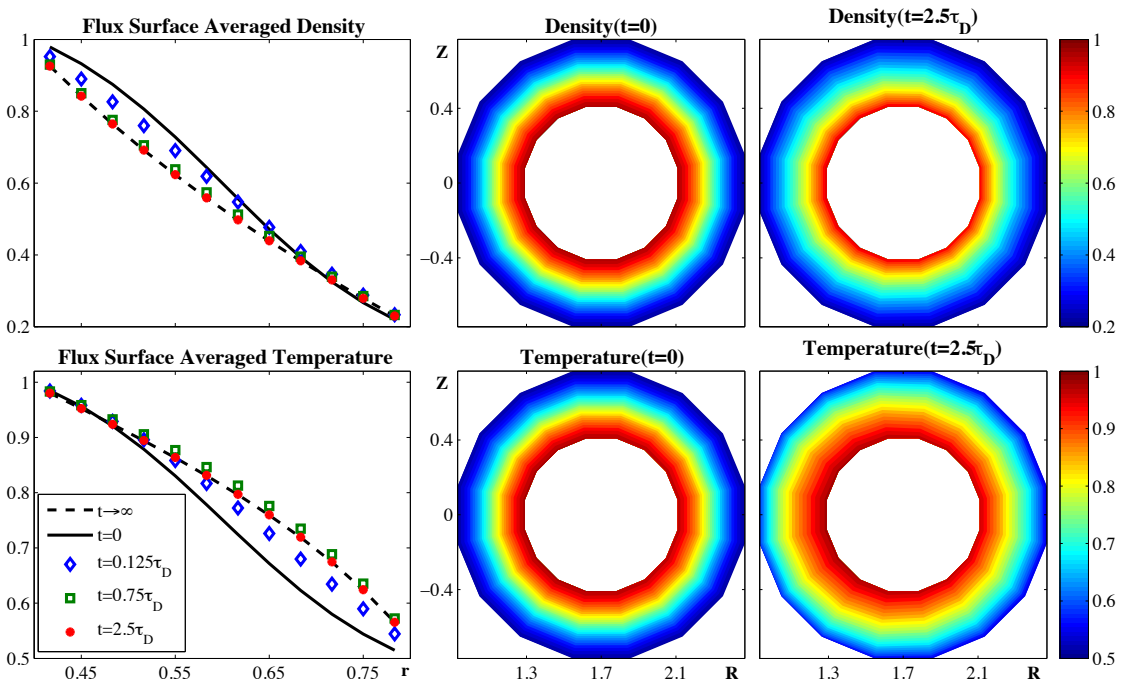

Figure 5.3: Relaxation of flux surface averaged density and temperature profiles for a purely diffusive fluid tranpsport matrix with kinetic flux specified in Eq. 5.34. The values for $t \to \infty$ are the steady state solutions. The diffusive time is defined as $\tau_D = (0.5(r_{max} - r_{min}))^2/D_{11}$.

5.4.3 Test3: Purely Conductive Plasma

Consider a plasma with no density evolution, but a diffusive heat coefficient. The free parameter D_{n0} needs to be used in this situation so that the central finite difference scheme will be numerically stable. The simplest choice for the free parameter D_{n0} for this problem seems to be $D_{n0} = \frac{2}{3}D_{22}$. The kinetic and

corresponding fluid transport matrices are

$$-\Gamma_\Psi = \frac{2}{3} D_{22} \frac{\partial f}{\partial r} \mid_{\mathbf{v}} - \frac{2}{3} \left(D_{22} \frac{1}{n} \frac{\partial n}{\partial r} \right) f, \tag{5.37}$$

$$-\Gamma_n = 0, \tag{5.38}$$

$$-\Gamma_Q = D_{22} n \frac{\partial T}{\partial r}. \tag{5.39}$$

The steady state solution of the temperature is again governed by Eq. 5.29 with $\beta = 0$, but the steady state density profile is whatever the density is at $t = 0$. Results from a numerical simulation of Eq. 5.6 with the flux specified in Eq. 5.37 that match the steady state profiles are shown in Fig. 5.4.

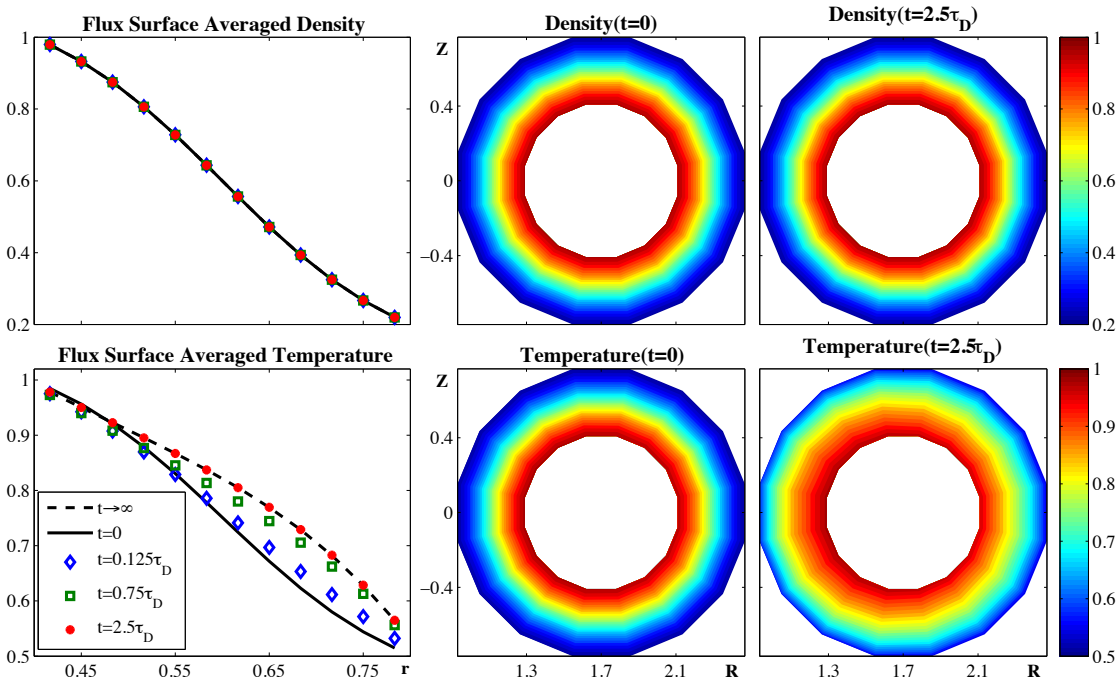

Figure 5.4: Relaxation of flux surface averaged density and temperature profiles for purely conducting plasma with kinetic flux specified in Eq. 5.37. The values for $t \to \infty$ are the steady state solutions. The diffusive time is defined as $\tau_D = (0.5(r_{max} - r_{min}))^2 / D_{22}$.

5.5 Conclusion

A model to represent the effects on mean parameter evolution in magnetic confinement devices due to anomalous radial transport is proposed. The general form of the model term is formulated from the gyro-kinetic equations and preserves adiabatic moment. The anomalous flux is constructed in the conventional advective-diffusive manner where the gradients are taken across flux surfaces. For initial implementation and testing, the model has been formulated in such a way that the moments of the anomalous flux can match typical fluid transport matrices. To make the model more flexible, it is demonstrated how this can be accomplished even if the distribution function is not Maxwellian. The model has been implemented into the gyrokinetic code COGENT and several successful tests have been performed using a circular annulus of a torus for the test geometry.

One of the main difficulty in anomalous transport studies is how to accurately represent the anomalous flux. Ideally it should be based on theoretical understandings, but, due to the complexity of turbulent transport, it is usually formulated by matching the fluid moment profiles from experimental results. Fully turbulent gyrokinetic studies, like those eventually to be done with COGENT, should give more insight into the parameters that govern the anomalous advection and diffusion coefficients. Furthermore, extension of the model to account for finite ion larmor radius effects should also be considered for edge transport studies where the ion gyroradius can be come comparable to the background gradient scales. Also, from a numerical perspective, the mixed derivative term that arises due to physically justifiable needs for the divergence and gradients to be calculated with different parameters held fixed makes the problem inherently unstable using explicit time integration. This was overcome in the work presented here by simultaneously solving the transport model with a 2V collision model that stabilized the system. However, implicit integration and more advanced advection schemes should eventually be considered [66, 67].

Chapter 6

Summary

The main goals of this Thesis work are to characterize and better understand some of the features of plasma transport in the edge region of magnetic confinement devices due to anomalous processes. This is accomplished through a combination of analytical and numerical work. More specifically, the 3D effects of parallel electron dynamics on plasma blobs are investigated, the drift wave instability in an arbitrarily collisional plasma is analyzed, and a fully conservative Fokker-Planck collision model for like-like species collisions along with an anomalous transport model are formulated for kinetic codes.

The strong convective nature of plasma blobs bring dense clumps of plasma across the SOL on time scales short with respect to the parallel loss time. This can cause significant damage to the first wall of fusion devices and pollute the core plasma. The standard 2D sheath limited theory of plasma blobs suggest that plasma blobs in future larger devices will be just as much of an issue as they are in current devices. However, a 3D analysis reveals that plasma blobs can be dissipated on time scales short compared to their advective time scale by the drift wave instability. The novel realization in coming to this result was recognizing that the plasma blob itself can be considered a background with a density gradient to feed the instability. The maximum drift wave growth rate compared to the blob advection rate scales with the square root of the radius of the device and

thus suggests that plasma blobs may not be as much as an issue in future larger devices such as ITER. Furthermore, blobs with initially varying profiles along the field line lead to a Boltzmann potential that acts as an additional sink of the 2D driving potential by spinning the blob. This spinning can greatly decrease the blobs initial advection velocity when the Boltzmann potential becomes comparable to the conventional 2D potential that drives the blob radially outward.

The results from the 3D analysis of plasma blobs were obtained using a reduced set of the collisional Braginskii equations under the assumptions of high collisionality, isothermal electrons, and cold ions. However, the mode structure and frequency of the dominant unstable drift wave modes that occurred on the plasma blobs were found to be in parameter regimes that only marginally satisfied the requirements for these assumptions. A linear dispersion relation obtained from a kinetic treatment of the system was analyzed to see how the linear drift wave dynamics would be altered due to finite electron mean free path, finite parallel electron heat flow, and finite temperature ions. It was found that the maximum growth rate was practically unchanged due to finite parallel electron heat flow and weather or not the destabilizing mechanism was collisionless Landau damping or collisional momentum exchange. The growth rate in both cases is on the order of the fundamental drift wave frequency, which is independent of the destabilizing mechanism. The only thing that changed was the parallel mode number corresponding to the maximum growth rate. On the other hand, finite ion temperature was found to decrease the maximum growth rate, as it decreased the fundamental drift wave frequency, but, even in the extreme case where the ions are an order of magnitude larger than the electron, the decrease was only by about a factor of two. The main effect of finite ion temperature was to shift the perpendicular wave number corresponding to the maximum growth rate from $k_\perp \rho_s \approx 1$ in the cold ion case to $k_\perp \rho_i \approx 1$ for warm ions.

The Fokker-Planck collision operator with coefficients in the form of that for Brownian motion is implemented as a model operator for like-like species collisions in a plasma. It is demonstrated how the exact conservation of density, momentum,

and energy can be obtained numerically with minimal computational effort. The model is implemented into the gyrokinetic code COGENT and thermalization tests demonstrate the ability of the operator to relax the distribution function to a Maxwellian while conserving all moments. The maximum error in the distribution function from a Maxwellian saturates to the corners of the velocity grid. The error in the moments as the distribution function relaxes to thermodynamic equilibrium are on the order of the machine accuracy and completely negligible.

A model to represent the effects of anomalous electrostatic fluctuations on the mean profile evolution for gyrokinetic codes is formulated. The radial flux divergence is taken at constant μ, reflecting the conservation of adiabatic invariance, and the radial gradients of mean parameters are taken at constant velocity, reflecting the flux surface gradient driven transport. The model is formulated so that the fluid moments match typical models used in fluid codes. Several successful tests in toroidal geometry are presented.

In closing, a 3D characterization of plasma blobs and a kinetic description of anomalous cross field transport has been presented. I believe that the most relevant issues going forward with a more complete 3D model of plasma blobs is to address the role of parallel electron kinetics, finite ion larmor radius, and electromagnetic effects. The important issues for future anomalous transport studies are the need for implicit integration schemes, effects of finite ion larmor radius, and a more accurate description of the anomalous flux based on results from fully turbulent simulations.

Appendix A

Basic Physics of Linear Flute Modes and Drift Waves

The basic mechanics of the 2D linear flute mode instability and the 3D linear drift wave are demonstrated in Fig. A.1. Both modes are quasi neutral, electrostatic, incompressible, and contain a background density gradient normal to a magnetic field. The density oscillations in both cases are driven by an E×B drift velocity associated with an electrostatic potential. The different nature between these two linear modes is due to the different physics that sets the potential.

Linear flute modes are a 2D phenomenon that are analogous to the standard Rayleigh-Taylor instability in fluid dynamics. "Effective" gravity forces in the opposite direction of the background density gradient cause the electrons and ions to drift normal to both the magnetic field and the background gradient, but opposite to each other. If a density perturbation exist normal to the background gradient and magnetic field, then the gravity forces polarize the perturbation and the resulting electric field drives the higher density perturbations into the lower density regions and vice versa. This mode is a purely growing mode and the growth rate is wavelength independent.

For drift waves, it is assumed that there are no gravity forces, but there is

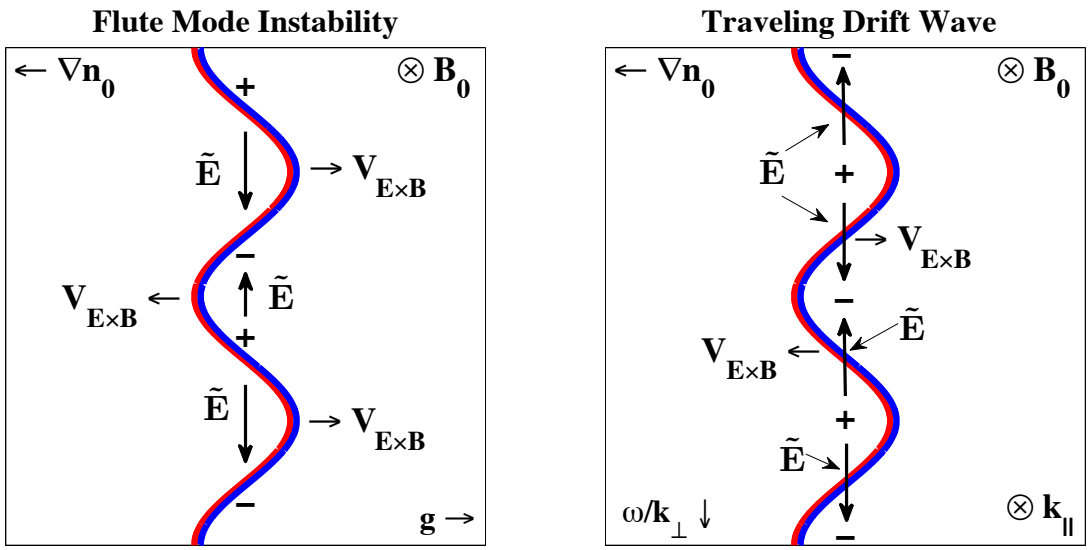

Figure A.1: Fundamental picture of unstable stationary flute mode(left) and stable traveling drift wave (right). The red isolines represent the higher density regions and the blue isolines represent the lower density regions.

a small finite parallel wavenumber $k_{\parallel} << k_{\perp}$. In the ideal situation where the parallel conductivity of the plasma is infinite, the electrons will move freely along the magnetic field lines due to the parallel pressure gradient and set up a Boltzmann potential. The Boltzmann potential is positive at the higher density regions and negative at the lower density regions. This potential leads to a stable wave that travels in the electron diamagnetic direction with the electron diamagnetic drift velocity. The drift wave is only stable in this most ideal case where the potential is perfectly Boltzmann. Any finite resistance to the electrons as they move along the field line will cause a deviation of the potential from a perfect Boltzmann and make the modes unstable.

Appendix B

Derivation of Eq. 3.13

The derivation of the expression for $\tilde{n}_e/n_0$ in terms of $e\tilde{\phi}/T_e$ (Eq. (3.13)) from Eq. (3.10) is given here. It should be mentioned that the normalization used here is for notational convenience only and is not the same as the normalization used in the rest of the paper. Eq. (3.10) can be written as

$$\tilde{f} = \left[\left(1 + \frac{\alpha - \hat{\omega}_*}{\hat{v}_\parallel - \alpha}\right)\frac{e\tilde{\phi}}{T_e} - \frac{i\hat{\nu}}{\hat{v}_\parallel - \alpha}\frac{\tilde{n}_e}{n_0} - \frac{i\hat{\nu}\left(\hat{v}^2 - \frac{3}{2}\right)}{\hat{v}_\parallel - \alpha}\frac{\tilde{T}}{T_e}\right]\frac{n_0 \exp\left[-\hat{v}^2\right]}{\left(2\pi v_e^2\right)^{3/2}}, \qquad \text{(B.1)}$$

where $\alpha = \hat{\omega} + i\hat{\nu}$, $(\hat{\omega}, \hat{\nu}, \hat{\omega}_*) = (\omega, \nu, \omega_*) \,/\, \left(\sqrt{2}v_e k_\parallel\right)$, and $\hat{v}^2 = \left(v_r^2 + v_\parallel^2\right) / \left(2v_e^2\right)$. The velocity space is taken in cylindrical coordinates. The zeroth moment of Eq. (B.1) divided by n_0 is

$$\begin{aligned}\frac{\tilde{n}_e}{n_0} &= 2\pi \int_{-\infty}^{\infty}\int_0^{\infty} \frac{\tilde{f}}{n_0} v_r dv_r dv_\parallel \\ &= \left(1 + (\alpha - \hat{\omega}_*)\, Z\right)\frac{e\tilde{\phi}}{T_e} - i\hat{\nu} Z \frac{\tilde{n}_e}{n_0} - i\hat{\nu}\left(\alpha + \left(\alpha^2 - \frac{1}{2}\right) Z\right)\frac{\tilde{T}}{T_e}, \qquad \text{(B.2)}\end{aligned}$$

where $Z = Z(\alpha)$ is the plasma dispersion function. The second moment of Eq. (B.1) divided by $2v_e^2 n_0$ is

$$\begin{aligned}
&\frac{3}{2}\left(\frac{\tilde{n}_e}{n_0}+\frac{\tilde{T}}{T_e}\right) = 2\pi\int_{-\infty}^{\infty}\int_{0}^{\infty}\frac{v^2\tilde{f}}{2v_e^2 n_0}v_r dv_r dv_\parallel \\
= \;& \left(1+\alpha^2\right)\frac{\tilde{n}_e}{n_0} - i\hat{\nu}Z\frac{\tilde{T}}{T_e} + \int_{-\infty}^{\infty}\left[\left(\hat{v}_\parallel-\alpha\right)^2+2\alpha\left(\hat{v}_\parallel-\alpha\right)\right]\left[\left(1+\frac{\alpha-\hat{\omega}_*}{\hat{v}_\parallel-\alpha}\right)\frac{e\tilde{\phi}}{T_e}\right. \\
- \;& \left.\frac{i\hat{\nu}}{\hat{v}_\parallel-\alpha}\frac{\tilde{n}_e}{n_0} - \frac{i\hat{\nu}\left(\hat{v}_\parallel^2-\frac{1}{2}\right)}{\hat{v}_\parallel-\alpha}\frac{\tilde{T}}{T_e}\right]\frac{\exp\left[-\hat{v}_\parallel^2\right]}{\sqrt{\pi}}d\hat{v}_\parallel \\
= \;& \left(1-i\hat{\nu}\alpha+\alpha^2\right)\frac{\tilde{n}_e}{n_0} - i\hat{\nu}Z\frac{\tilde{T}}{T_e} + \left(\frac{1}{2}-\alpha\hat{\omega}_*\right)\frac{e\tilde{\phi}}{T_e}. \qquad \text{(B.3)}
\end{aligned}$$

The temperature fluctuations can be removed by combining Eq. (B.2) and Eq. (B.3) and the result may be written as

$$\frac{\tilde{n}_e}{n_0} = \left[\frac{\left(1+\left(\alpha-\hat{\omega}_*\right)Z\right)\left(\frac{3}{2}+i\hat{\nu}Z\right)+i\hat{\nu}\left(\hat{\omega}_*\alpha-\frac{1}{2}\right)\left(\alpha+\left(\alpha^2-\frac{1}{2}\right)Z\right)}{\left(1+\left(\alpha-\hat{\omega}\right)Z\right)\left(\frac{3}{2}+i\hat{\nu}Z(\alpha)\right)+i\hat{\nu}\left(\hat{\omega}\alpha-\frac{1}{2}\right)\left(\alpha+\left(\alpha^2-\frac{1}{2}\right)Z\right)}\right]\frac{e\tilde{\phi}}{T_e}. \qquad \text{(B.4)}$$

This result is equivalent to Eq.(3.13).

Appendix C

Numerical Stability of 3D Advection-Diffusion with Mixed Derivative

The anomalous cross field flux combined with the drag-diffusion collision operator is essentially a 3D advective and diffusive problem with the addition of a mixed derivative term. To see how this mixed derivative alters the conventional stability restraints for the multidimensional advection-diffusion problem with central differencing and interpolation, a Von Neumman stability analysis is performed. Consider a simple 3D planer geometry where the governing equation takes the following form:

$$\frac{\partial f}{\partial t} = \frac{\partial}{\partial x_i}\left[D_i \frac{\partial f}{\partial x_i} - U_i f\right] - \frac{\partial}{\partial x}\left[\frac{y D_x}{B}\frac{\partial B}{\partial x}\frac{\partial f}{\partial y}\right], \tag{C.1}$$

where summation notation is implied, D_i is the diffusion coefficient in the ith dimension, and U_i is the convection coefficient in the ith dimension. The standard Von Neumman stability analysis of Eq. C.1 yields the following Fourier mode amplification factor:

$$G(\theta_x, \theta_y, \theta_z) = \left[1 - 4\left(\alpha_i \sin^2\frac{\theta_i}{2}\right) + \beta \sin\theta_x \sin\theta_y\right] - j\left[c_i \sin\theta_i\right], \tag{C.2}$$

where $j = \sqrt{-1}$ and $\theta_i = k_i h_i$ with h_i, k_i respectively the numerical grid spacing and wavenumber in the ith dimension. The coefficients α_i, β, and c_i are defined as

$$\alpha_i = \frac{D_i \Delta t}{h_i^2}, \qquad \beta = \frac{D \Delta t}{h_x h_y} \frac{y}{B} \frac{\partial B}{\partial x}, \qquad c_i = \frac{U_i \Delta t}{h_i}. \tag{C.3}$$

α_i and c_i are respectively the diffusion number and the Courant number in the ith dimension.

The numerically stability of Eq. C.1 using central finite difference and interpolation schemes requires that $|G(\theta_x, \theta_y, \theta_y)|$ be less than unity for all finite values of θ_x, θ_y, and θ_z:

$$|G| = \left[1 - 4\left(\alpha_i \sin^2 \frac{\theta_i}{2}\right) + \beta \sin\theta_x \sin\theta_y\right]^2 + \left[c_i \sin\theta_i\right]^2 < 1. \tag{C.4}$$

The condition for stability when all values of $\theta = \pm\pi$ gives the standard multidimensional diffusion condition:

$$\alpha_x + \alpha_y + \alpha_z < \frac{1}{2}. \tag{C.5}$$

Stability conditions for all other wavelengths is determined by recognizing that $|G(0,0,0)| = 1$ and corresponds to the maximum value when the following 2nd derivative test restraints for a function of three variables are satisfied:

$$\frac{c_x^2}{\alpha_x} < 2, \qquad \frac{c_y^2}{\alpha_y} < 2, \qquad \frac{c_z^2}{\alpha_z} < 2, \tag{C.6}$$

$$\frac{2\beta c_x c_y}{\alpha_x \alpha_y} + \frac{c_x^2}{\alpha_x} + \frac{c_y^2}{\alpha_y} + \frac{c_z^2}{\alpha_z} < 2 - \frac{\beta}{2\alpha_x \alpha_y}\left(\beta - \frac{c_z^2}{\alpha_z}\right). \tag{C.7}$$

Note that the RHS of Eq. C.7 is independent of Δt and reduces to the conventional restraint when $\beta = 0$. Also note that if $c_y = \alpha_y = 0$, then the stability condition in Eq. C.7 reduces to $\beta^2 < 0$ and the system is never stable.

Bibliography

[1] J. Lamarsh and A. Baratta, "Introduction to nuclear engineering," 2001.

[2] J. Wesson, *Tokamaks*, vol. 149. OUP Oxford, 2011.

[3] P. Stangeby *et al.*, *The plasma boundary of magnetic fusion devices*. Institute of Physics Pub., 2000.

[4] F. Hinton and R. Hazeltine, "Theory of plasma transport in toroidal confinement systems," *Reviews of Modern Physics*, vol. 48, no. 2, p. 239, 1976.

[5] J. Connor, "Tokamak turbulence-electrostatic or magnetic?," *Plasma physics and controlled fusion*, vol. 35, no. SB, p. B293, 1999.

[6] C. Ritz, R. Bravenec, R. Bengtson, K. Gentle, C. Klepper, P. Phillips, E. Powers, T. Rhodes, B. Richards, W. Rowan, *et al.*, "Edge diagnostics and transport in the text tokamak," *Journal of Nuclear Materials*, vol. 145, pp. 241–244, 1987.

[7] A. Wootton, B. Carreras, H. Matsumoto, K. McGuire, W. Peebles, C. Ritz, P. Terry, and S. Zweben, "Fluctuations and anomalous transport in tokamaks," *Physics of Fluids B: Plasma Physics*, vol. 2, p. 2879, 1990.

[8] C. Hidalgo, "Edge turbulence and anomalous transport in fusion plasmas," *Plasma Physics and Controlled Fusion*, vol. 37, no. 11A, p. A53, 1995.

[9] B. Carreras, "Plasma edge cross-field transport: experiment and theory," *Journal of nuclear materials*, vol. 337, pp. 315–321, 2005.

[10] S. Zweben, J. Boedo, O. Grulke, C. Hidalgo, B. LaBombard, R. Maqueda, P. Scarin, and J. Terry, "Edge turbulence measurements in toroidal fusion devices," *Plasma Physics and Controlled Fusion*, vol. 49, no. 7, p. S1, 2007.

[11] G. Conway, "Turbulence measurements in fusion plasmas," *Plasma Physics and Controlled Fusion*, vol. 50, no. 12, p. 124026, 2008.

[12] J. Boedo, D. Rudakov, R. Moyer, S. Krasheninnikov, D. Whyte, G. McKee, G. Tynan, M. Schaffer, P. Stangeby, P. West, *et al.*, "Transport by intermittent convection in the boundary of the diii-d tokamak," *Physics of Plasmas*, vol. 8, p. 4826, 2001.

[13] D. Rudakov, J. Boedo, R. Moyer, N. Brooks, R. Doerner, T. Evans, M. Fenstermacher, M. Groth, E. Hollmann, S. Krasheninnikov, *et al.*, "Far scrape-off layer and near wall plasma studies in diii-d," *Journal of nuclear materials*, vol. 337, pp. 717–721, 2005.

[14] R. Maqueda, D. Stotler, Z. S.J., and T. N. team, "Intermittency in the scrape-off layer of the national sphereical torus experiment during h-mode confinement," *Journal of nuclear materials*, vol. 415, pp. 459–462, 2011.

[15] A. Pigarov, S. Krasheninnikov, T. Rognlien, M. Schaffer, and W. West, "Tokamak edge plasma simulation including anomalous cross-field convective transport," *Physics of Plasmas*, vol. 9, p. 1287, 2002.

[16] T. Rognlien, M. Umansky, X. Xu, and R. Cohen, "Self-consistent simulation of turbulence and transport in tokamak edge plasmas," *Contributions to Plasma Physics*, vol. 44, no. 1-3, pp. 188–193, 2004.

[17] D. D'Ippolito, J. Myra, and S. Zweben, "Convective transport by intermittent blob-filaments: Comparison of theory and experiment," *Physics of Plasmas*, vol. 18, p. 060501, 2011.

[18] S. Krasheninnikov, "On scrape off layer plasma transport," *Physics Letters A*, vol. 283, no. 5-6, pp. 368–370, 2001.

[19] G. Yu and S. Krasheninnikov, "Dynamics of blobs in scrape-off-layer/shadow regions of tokamaks and linear devices," *Physics of Plasmas*, vol. 10, p. 4413, 2003.

[20] D. Russell, D. D'Ippolito, J. Myra, W. Nevins, and X. Xu, "Blob dynamics in 3d bout simulations of tokamak edge turbulence," *Physical review letters*, vol. 93, no. 26, p. 265001, 2004.

[21] J. Myra, D. DIppolito, S. Krasheninnikov, and G. Yu, "Convective transport in the scrape-off-layer by nonthermalized spinning blobs," *Physics of plasmas*, vol. 11, p. 4267, 2004.

[22] O. Garcia, V. Naulin, A. Nielsen, and J. Rasmussen, "Computations of intermittent transport in scrape-off layer plasmas," *Physical review letters*, vol. 92, no. 16, p. 165003, 2004.

[23] A. Aydemir, "Convective transport in the scrape-off layer of tokamaks," *Physics of plasmas*, vol. 12, p. 062503, 2005.

[24] O. Garcia, N. Bian, and W. Fundamenski, "Radial interchange motions of plasma filaments," *Physics of plasmas*, vol. 13, p. 082309, 2006.

[25] S. Krasheninnikov, D. DIppolito, and J. Myra, "Recent theoretical progress in understanding coherent structures in edge and sol turbulence," *J. Plasma Phys*, vol. 74, 2008.

[26] I. Furno, B. Labit, M. Podestà, A. Fasoli, S. Müller, F. Poli, P. Ricci, C. Theiler, S. Brunner, A. Diallo, *et al.*, "Experimental observation of the blob-generation mechanism from interchange waves in a plasma," *Physical review letters*, vol. 100, no. 5, p. 55004, 2008.

[27] O. Garcia, "Blob transport in the plasma edge: a review," *Plasma and Fusion Research*, vol. 4, no. 0, pp. 19–19, 2009.

[28] P. Manz, M. Xu, S. Müller, N. Fedorczak, S. Thakur, J. Yu, and G. Tynan, "Plasma blob generation due to cooperative elliptic instability," *Physical Review Letters*, vol. 107, no. 19, p. 195004, 2011.

[29] C. Theiler, I. Furno, J. Loizu, and A. Fasoli, "Convective cells and blob control in a simple magnetized plasma," *Physical Review Letters*, vol. 108, no. 6, p. 065005, 2012.

[30] J. Angus, M. Umansky, and S. Krasheninnikov, "Effect of drift waves on blob dynamics," *Physical Review Letters*, vol. 108, no. 21, p. 215002, 2012.

[31] B. Dudson, M. Umansky, X. Xu, P. Snyder, and H. Wilson, "Bout++: A framework for parallel plasma fluid simulations," *Computer Physics Communications*, vol. 180, no. 9, pp. 1467–1480, 2009.

[32] P. Popovich, M. Umansky, T. Carter, and B. Friedman, "Analysis of plasma instabilities and verification of the bout code for the large plasma device," *Physics of Plasmas*, vol. 17, no. 10, p. 2107, 2010.

[33] S. Krasheninnikov and A. Smolyakov, "On neutral wind and blob motion in linear devices," *Physics of Plasmas*, vol. 10, p. 3020, 2003.

[34] X. Xu, R. Cohen, T. Rognlien, and J. Myra, "Low-to-high confinement transition simulations in divertor geometry," *Physics of Plasmas*, vol. 7, p. 1951, 2000.

[35] P. M. Bellan, *Fundamentals of plasma physics*. Cambridge Univ Pr, 2006.

[36] J. Angus and S. Krasheninnikov, "Drift wave dispersion relation for arbitrarily collisional plasmas," *Physics of Plasmas*, vol. 19, p. 052504, 2012.

[37] D. DIppolito, J. Myra, D. Russell, and G. Yu, "Rotational stability of plasma blobs," *Physics of plasmas*, vol. 11, p. 4603, 2004.

[38] X. Lee, P. Catto, and R. Aamodt, "Instabilities driven by the parallel variation of the electrostatic potential in tandem mirrors," *Physics of Fluids*, vol. 25, p. 1491, 1982.

[39] W. Horton, "Drift waves and transport," *Rev. Mod. Phys.*, vol. 71, pp. 735–778, Apr 1999.

[40] P. L. Bhatnagar, E. P. Gross, and M. Krook, "A model for collision processes in gases. i. small amplitude processes in charged and neutral one-component systems," *Phys. Rev.*, vol. 94, pp. 511–525, May 1954.

[41] S. Braginskii, "Transport processes in a plasma," *Reviews of plasma physics*, vol. 1, p. 205, 1965.

[42] C. Cercignani, *Mathematical methods in kinetic theory*. Plenum Press New York, 1990.

[43] C. Cercignani, *Rarefied gas dynamics: from basic concepts to actual calculations*, vol. 21. Cambridge Univ Pr, 2000.

[44] J. R. Angus, M. V. Umansky, and S. I. Krasheninnikov *Submitted to Phys. Rev. Lett.*

[45] K. Pearson, "The problem of the random walk," *Nature*, vol. 72, no. 1865, p. 294, 1905.

[46] S. Chandrasekhar, "Stochastic problems in physics and astronomy," *Reviews of modern physics*, vol. 15, no. 1, pp. 1–89, 1943.

[47] M. Rosenbluth, W. MacDonald, and D. Judd, "Fokker-planck equation for an inverse-square force," *Physical Review*, vol. 107, no. 1, p. 1, 1957.

[48] F. Hinton, "Collisional transport in plasma," *Handbook of Plasma Physics*, vol. 1, p. 147, 1983.

[49] J. Chang and G. Cooper, "A practical difference scheme for fokker-planck equations," *Journal of Computational Physics*, vol. 6, no. 1, pp. 1–16, 1970.

[50] E. Epperlein, "Fokker-planck modeling of electron transport in laser-produced plasmas," *Laser and Particle Beams-Pulse Power and High Energy Densities*, vol. 12, no. 2, pp. 257–272, 1994.

[51] L. Chacón, D. Barnes, D. Knoll, and G. Miley, "An implicit energy-conservative 2d fokker–planck algorithm: I. difference scheme," *Journal of Computational Physics*, vol. 157, no. 2, pp. 618–653, 2000.

[52] Z. Xiong, R. Cohen, T. Rognlien, and X. Xu, "A high-order finite-volume algorithm for fokker–planck collisions in magnetized plasmas," *Journal of Computational Physics*, vol. 227, no. 15, pp. 7192–7205, 2008.

[53] I. Abel, M. Barnes, S. Cowley, W. Dorland, and A. Schekochihin, "Linearized model fokker-planck collision operators for gyrokinetic simulations. i. theory," *arXiv preprint arXiv:0808.1300*, 2008.

[54] M. Barnes, I. Abel, W. Dorland, D. Ernst, G. Hammett, P. Ricci, B. Rogers, A. Schekochihin, and T. Tatsuno, "Linearized model fokker-planck collision operators for gyrokinetic simulations. ii. numerical implementation and tests," *arXiv preprint arXiv:0809.3945*, 2008.

[55] M. Dorf, R. Cohen, J. Compton, M. Dorr, T. Rognlien, J. Angus, S. Krasheninnikov, P. Colella, D. Martin, and P. McCorquodale, "Progress with the cogent edge kinetic code: Collision operator options," *Contributions to Plasma Physics*, vol. 52, no. 5-6, pp. 518–522, 2012.

[56] K. Bodi, *Anomalous radial transport in tokamak edge plasma*. PhD thesis, University of California, San Diego, 2010.

[57] D. Montgomery and D. Tidman, "Plasma kinetic theory," *McGraw-Hill Advanced Physics Monograph Series, New York: McGraw-Hill, 1964*, vol. 1, 1964.

[58] D. Nicholson and D. Nicholson, *Introduction to plasma theory*.

[59] R. Hazeltine, "Recursive derivation of drift-kinetic equation," 1973.

[60] D. Dubin, J. Krommes, C. Oberman, and W. Lee, "Nonlinear gyrokinetic equations," *Physics of Fluids*, vol. 26, no. 12, pp. 3524–3535, 1983.

[61] T. Hahm, "Nonlinear gyrokinetic equations for tokamak microturbulence," *Physics of Fluids*, vol. 31, no. 9, pp. 2670–2673, 1988.

[62] T. Hahm, "Nonlinear gyrokinetic equations for turbulence in core transport barriers," *Physics of Plasmas*, vol. 3, p. 4658, 1996.

[63] P. Stangeby, "Modeling plasma contact with the main vessel walls of a divertor tokamak," *Physics of Plasmas*, vol. 9, p. 3489, 2002.

[64] E. Doyle *et al.*, "Progress in iter physics basis 2. plasma confinement and transport 2.2. fundamental transport processes," *Nuclear Fusion*, vol. 47, pp. S18–S127, 2007.

[65] M. Dorr, R. Cohen, P. Colella, M. Dorf, J. Hittinger, and D. Martin, "Numerical simulation of phase space advection in gyrokinetic models of fusion plasmas," in *Proc. 2010 Scientific Discovery through Advanced Computing (SciDAC) Conf.(Oak Ridge, TN,)*, pp. 42–52, 2010.

[66] I. Craig and A. Sneyd, "An alternating-direction implicit scheme for parabolic equations with mixed derivatives," *Computers & Mathematics with Applications*, vol. 16, no. 4, pp. 341–350, 1988.

[67] B. Welfert *et al.*, "Stability of adi schemes applied to convection–diffusion equations with mixed derivative terms," *Applied numerical mathematics*, vol. 57, no. 1, pp. 19–35, 2007.